

N71-35343

NASA CR-72868



**CASE FILE
COPY**

DESIGN AND DEVELOPMENT OF A SELF-HEALING FUSE

by

N. D. Jones and Dr. L. P. Harris

GENERAL ELECTRIC COMPANY

prepared for

NATIONAL AERONAUTICS AND SPACE ADMINISTRATION

NASA Lewis Research Center

Contract NAS12-675

Dr. Francisc C. Schwarz, Project Manager

NOTICE

This report was prepared as an account of Government-sponsored work. Neither the United States, nor the National Aeronautics and Space Administration (NASA), nor any person acting on behalf of NASA:

- A.) Makes any warranty or representation, expressed or implied, with respect to the accuracy, completeness, or usefulness of the information contained in this report, or that the use of any information, apparatus, method, or process disclosed in this report may not infringe privately-owned rights; or
- B.) Assumes any liabilities with respect to the use of, or for damages resulting from the use of, any information, apparatus, method or process disclosed in this report.

As used above, "person acting on behalf of NASA" includes any employee or contractor of NASA, or employee of such contractor, to the extent that such employee or contractor of NASA or employee of such contractor prepares, disseminates, or provides access to any information pursuant to his employment or contract with NASA, or his employment with such contractor.

Requests for copies of this report should be referred to

National Aeronautics and Space Administration
Scientific and Technical Information Facility
P.O. Box 33
College Park, Md. 20740

FINAL REPORT

DESIGN AND DEVELOPMENT OF A SELF-HEALING FUSE

by

N. D. Jones and Dr. L. P. Harris

GENERAL ELECTRIC COMPANY
Tube Department
Microwave Tube Operation
Schenectady, New York

prepared for

NATIONAL AERONAUTICS AND SPACE ADMINISTRATION

September 23, 1970

CONTRACT NAS12-675

NASA Lewis Research Center
Cleveland, Ohio
Dr. Francisc C. Schwarz, Project Manager
Spacecraft Technology Division

FOREWORD

The work described herein was done by the General Electric Microwave Tube Operation under NASA Contract NAS12-675 with N. D. Jones as principal investigator. Dr. Francisc C. Schwarz, Spacecraft Technology Division, NASA-Lewis Research Center, was Project Manager.

TABLE OF CONTENTS

	Page
SUMMARY	
INTRODUCTION	3
FUSE DESIGNS, MATERIALS AND FABRICATION TECHNIQUES	5
Single-Channel Alumina or Sapphire Devices	5
Narrow Channel Devices	10
Sandwich Structure Devices	21
External Fuse Structure	21
TEST AND PROCESSING APPARATUS	26
Processing Equipment	29
TEST PROCEDURES AND RESULTS	33
Circuit Protective Capability of Self-Healing Fuses	33
Effects of the Transition Explosion	35
Impedance of Current-Limiting Arc	40
Thermally-Induced Bore Erosion	42
Multiple-Channel Devices	53
DISCUSSION OF RESULTS	55
Factors in Circuit Protection	55
Arc Behavior and Thermal Erosion	56
Fabrication and Materials for the Fuse Channel	57
Design Parameters for Fuse Channel	59
CONCLUSIONS	63

	Page
Appendix A - AN ANALYSIS OF HIGH-PRESSURE METAL VAPOR ARCS IN NARROW CHANNELS	64
Appendix B - SURFACE EFFECTS OF HIGH-ENERGY PULSES	96
Appendix C - CURRENT LIMITERS DRIVEN BY CONSTANT CURRENTS	99
Appendix D - GLOSSARY OF SYMBOLS	104
REFERENCES	105

ABSTRACT

The mercury-filled self-healing fuses developed for this program afford very good protection from faults for solid-state circuits. Fuse performance and design parameters have been characterized. Trends in fuse behavior indicate good durability for devices with very small channels. A series of sample fuses using alumina and sapphire insulation have been furnished to NASA for circuit evaluation. Fuse ratings are 100 volts, up to 15 amperes.

SUMMARY

The purpose of this program was to develop construction techniques for mercury-filled self-healing fuses and to resolve related technological problems. The objective ratings were 15 amperes at 100 volts, with the capability of 1000 operations. Earlier work indicates that the explosive forces and the large flux of heat energy generated in the small fuse channel when the fuse is in operation are the major factors governing the utility of these devices. Sapphire, alumina and molybdenum were utilized as channel materials for this investigation.

The following three types of fuses were fabricated and tested: 1) alumina or sapphire devices with a single cylindrical channel, 2) alumina or sapphire devices with various forms of very narrow channels, and 3) structures of a sandwich geometry having conducting layers of molybdenum or cermet with alternate insulating layers of glass, alumina or rubber. All three types require pre-stressing of the insulation to prevent damage caused by the explosive forces. The sandwich devices are also vulnerable to the shorting out of the insulating layers, caused by injected mercury, which makes correct fabrication of these structures more difficult.

Restrained bellows structures were designed to buffer the impact forces and furnish restoring action to return mercury to the fuse channel after fuse operation. A somewhat novel sealing technique was also developed.

A solid-state circuit was used for the fuse testing program. Current and voltage waveforms were carefully monitored in order to evaluate fuse circuit protective capabilities and the amount of energy which could be accommodated by the fuse. The circuit protective capability was found to be very good and consistent and is thus amenable to straightforward calculation for fuses of various sizes. Also, the fuse is capable of switching functions such as clearing momentary circuit faults.

To check fuse durability, close observations were made of the changes in the electrical resistance of the mercury in the fuse channel as the channel became eroded by fuse action. Fuse durability proved to be very good when the channel material was strongly pre-stressed to prevent mechanical damage caused by the explosive forces and when the metal-vapor arc state extinguished within 10^{-3} second. Fuse channels of less than 0.008-inch diameter were found to provide better arc characteristics while multiple channel devices divided the arc energy very well. Thus, multiple small channels promise to provide the best fuse performance.

The arc impedance increases rapidly with decreasing channel size for non-cylindrical sapphire channels less than 0.002 inch across and such devices could withstand long-term arc operation, thus providing remarkable current-limiting capability.

INTRODUCTION

The objective of this contract was to develop construction techniques for a 15-ampere self-healing fuse in a form conducive to manufacture. Related scientific and technological problems were to be identified and solutions formulated. In general, this fuse was to take the form of a mercury-filled, closed container consisting of two end reservoirs connected by a small insulated channel. In operation, contact is broken when excessive current flowing through the channel vaporizes the mercury; after the fault has been cleared, contact is re-established when the mercury is forced back into the channel by gravity-independent restoring forces supplied by the container.

The nominal fuse rating sought was 15 amperes at 100 volts, with the fuse to be storable between -65°C and $+150^{\circ}\text{C}$ and operable at ambient temperatures from -30°C to $+80^{\circ}\text{C}$, with the capability of 1000 or more operations without failure. This report describes the work performed toward achieving these objectives, with the investigation limited to the use of mercury as the metallic medium.

The self-healing fuse in its earliest conception* takes advantage of the very large difference in electrical resistivity between the liquid state and gaseous vapor state of liquid metals, typically mercury. The work of several other investigators has also been documented.** This earlier fuse work was primarily addressed to power distribution applications involving fault currents of thousands of amperes, compared to the current range of 15 to a few hundred amperes covered by this program and by the concurrent work at NASA performed by Dr. C. A. Renton.

Self-healing fuse operation involves three stages: (1) The energy-limiting stage is defined by the energy required to heat the liquid mercury in the channel to its boiling temperature. The channel cross-section is then filled very rapidly by a bubble of neutral mercury vapor, which simultaneously breaks down to a mercury arc discharge. (2) In the transition stage, the fuse voltage initially rises very rapidly to a value determined

* R. L. Hurtle, patent Nos. 3,117,203 and 3,158,786

**L. J. Goldberg, patent No. 3,273,018; L. P. Harris, patent No. 3,389,359; J. J. Keenan, patent No. 3,389,360

by the circuit parameters, while current simultaneously decays at a rate determined by these parameters. During the transition stage, explosive forces expel all of the liquid mercury from the channel. (3) After the transition, the mercury arc either extinguishes or operates for times of the order of milliseconds with an arc impedance 100 or more times greater than the resistance of the liquid mercury column. Because the current is limited by the comparatively large arc impedance, these devices have also been termed "change of state current limiters" (CSCL's) in earlier work.

The explosive transition forces per unit area are high -- generating pressures of the order of 10,000 psi -- although the net force resulting is quite small due to the very small channel sizes. Similarly, the current limiting arc results in a large flux of heat energy per unit area for the fuse channel walls, although the circuit energy is limited to very modest levels by the high arc impedance. Since the transition occurs in a very short time and most of the transition energy becomes heat at the walls of the fuse channel, transition stage heat energy also becomes an important factor.

FUSE DESIGNS, MATERIALS AND FABRICATION TECHNIQUES

In terms of technology, the background available from earlier investigations of the CSCL devices cited in the Introduction had established the existence of two major factors as governing the usefulness of these devices: (1) the device must mechanically withstand the explosive transition forces, and (2) the fuse materials must withstand the large flux of heat energy generated within the fuse channel during the transition explosion and any subsequent current-limiting arc action. Thus these two factors become primary considerations in selection of materials and designs for these devices. Because some practicable limits had to be established relative to the variations of materials and designs which could be evaluated, and since the availability and fabrication techniques favored the use of alumina or sapphire as an insulator, and molybdenum as a refractory metal, these three materials were established as the major candidates.

SINGLE-CHANNEL ALUMINA OR SAPPHIRE DEVICES

Where the channel geometry was a single cylindrical hole, more experimental devices utilizing alumina or sapphire as the channel material were made and tested than any other category of device. Such devices obviously avoid the problem of injected mercury shorting out the device, as can occur in the case of the sandwich-type device. However, since these devices utilize a single piece of heavy-walled tubing with a small hole (0.008- to 0.020-inch diameter), they must be pre-stressed by compressing the tubing from the outside to overcome the tensile stresses induced by the explosive transition forces.

Three designs used in these experimental devices are shown in Figures 1, 2 and 3. The double-conical geometry device shown in Figure 1 provided the best performance in terms of resisting the transition forces, and more fuses of this design were fabricated than any other. A completed fuse and its component parts are shown pictorially in Figure 4, and various double-conical cores can be seen in Figure 5.

The design of Figure 2 also performed well when the filler material (shown shaded in this cross-section) was of glass. Here the metal restraining rings apply a compressive restraint force to the glass due to differential thermal contraction as the assembly cools after the glass has been molded in place at approximately 1000°C. The epoxy filler used was a high temperature

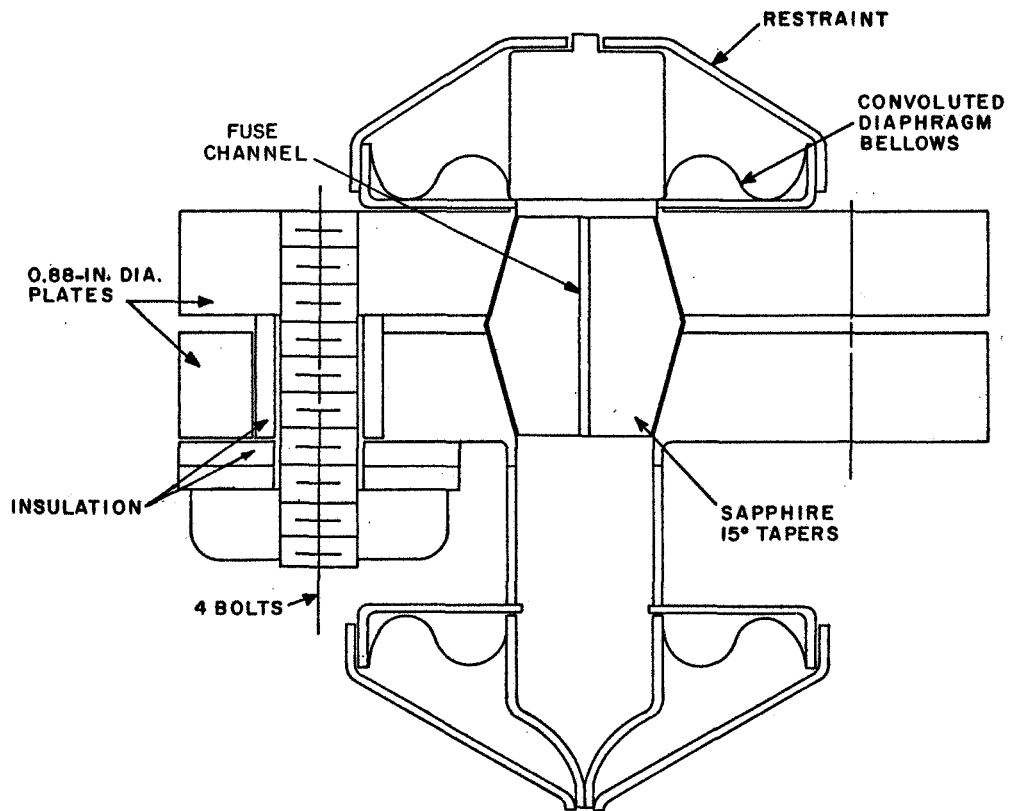


Figure 1 - Double-Conical Geometry Fuse Design

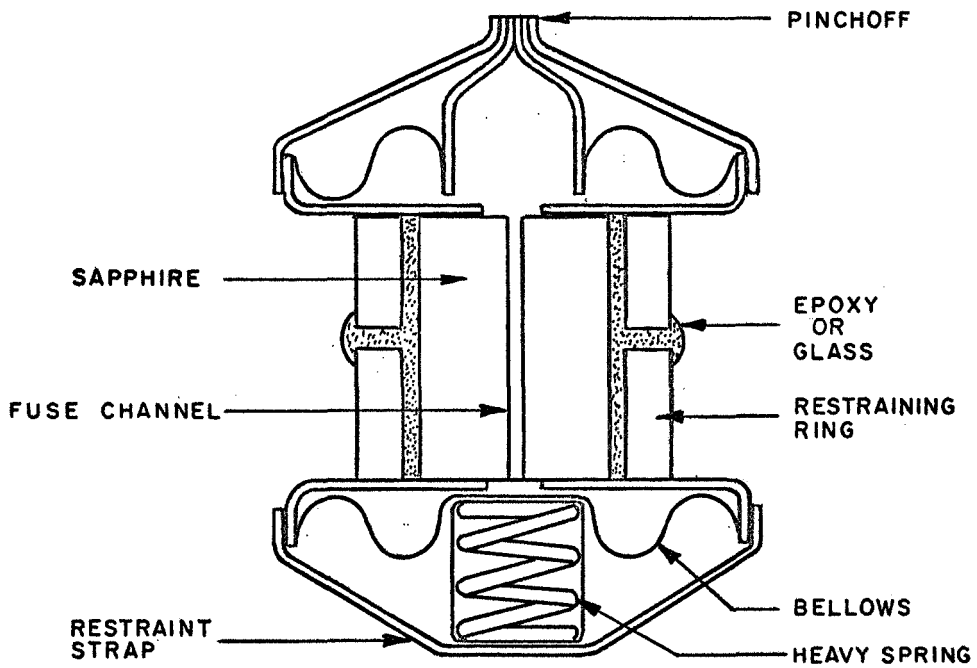


Figure 2 - Molded Fuse Design

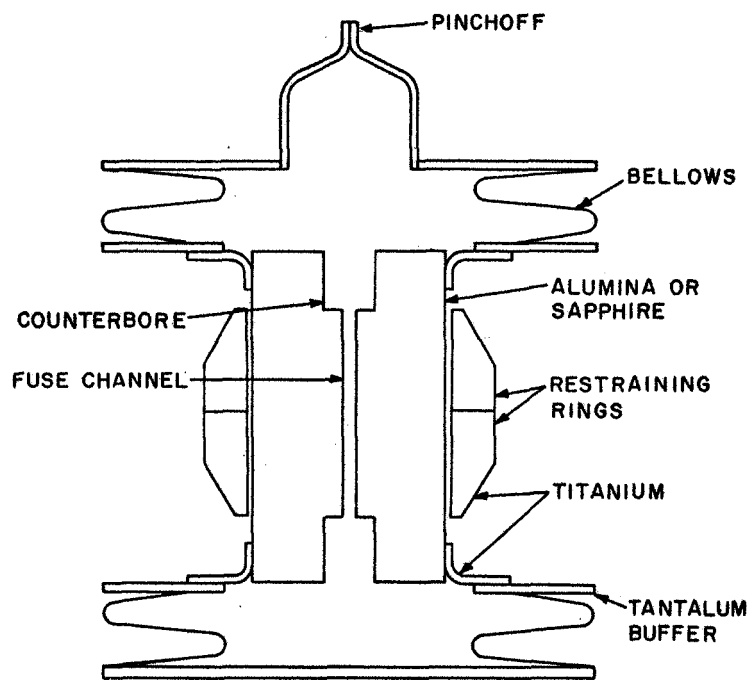


Figure 3 - Titanium Ring Fuse Design

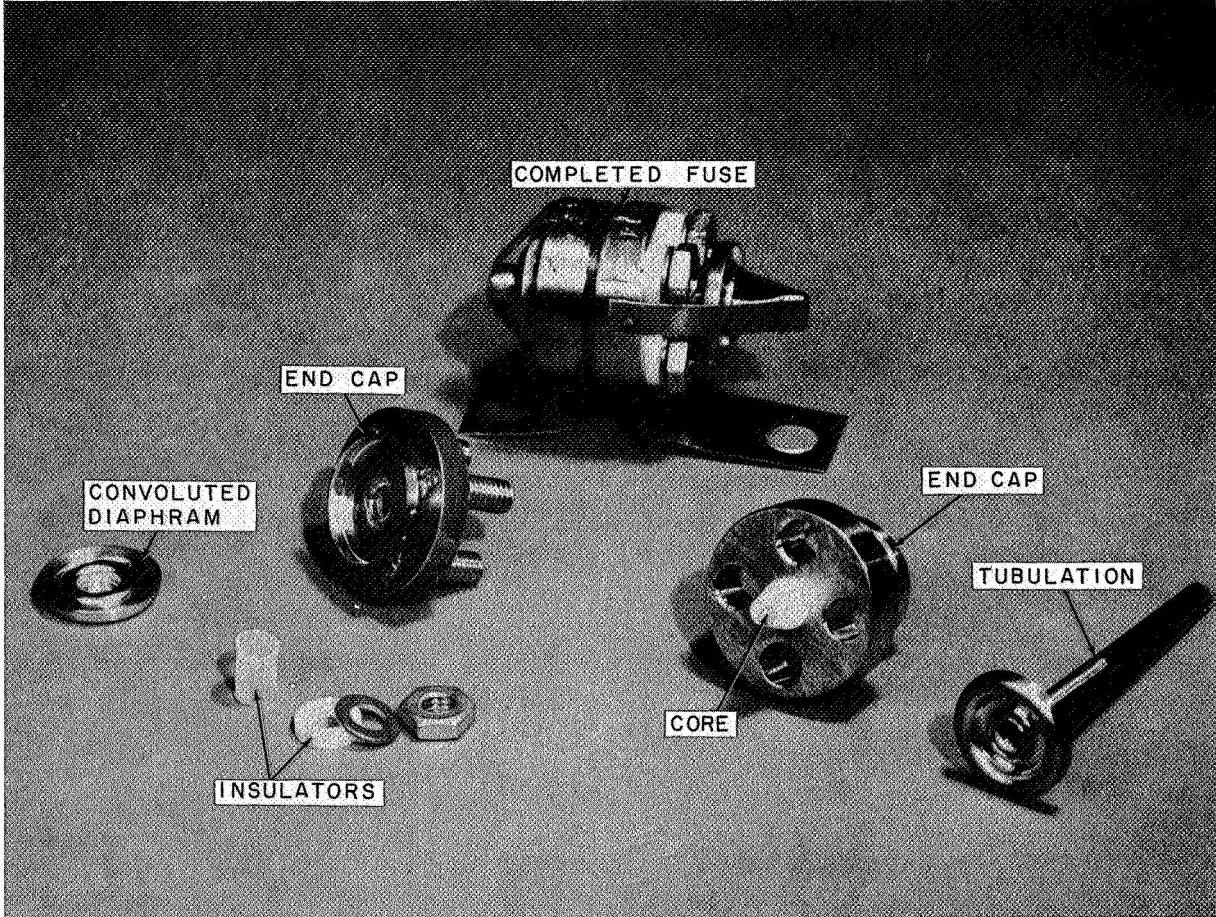


Figure 4 - Double-Conical Fuse and Parts

aluminum-filled composition* and fuses using this material were reliable only up to fault currents of approximately 150 amperes. The Figure 3 design which was least successful, was used for devices evaluated early in the program. In this configuration, titanium restraining rings were brazed in place using standard active-alloy (titanium bearing) metal-ceramic sealing techniques. It was difficult to balance the stresses where the tension rings ended, with or without the counterbores shown. The open spaces near the ends of the fuse channel provided the required electrical insulation.

The sapphire tubing used in the devices was single-crystal material, grown in the form of tubing.** Some tubing was large enough in outside diameter to permit fabrication into the required shape, and some was of outside diameter as small as 0.030 inch, which was first imbedded in glass (by the usual hand glass-working techniques) and then fabricated into the desired configuration.

The alumina materials used were "high purity" commercial alumina (99+ percent alumina) and a proprietary*** "ultra-pure" (99.8+ percent) alumina body prepared in General Electric's Microwave Tube Operation ceramic laboratory.

The single-channel fuses which were fabricated and were given significant evaluation tests are listed in Table I.

NARROW CHANNEL DEVICES

In order to gain additional insight into the parameters affecting arc operation in these devices, an extensive analysis of the arc mechanism was undertaken. This analytical study of high pressure metal arcs in narrow channels is included as Appendix A in this report. The more pertinent results of this analysis are shown in Figure 36 where arc voltage gradient and current density are plotted with channel thickness as a parameter. Much higher arc impedance and somewhat lower arc plasma temperature are predicted for very narrow channels by this analysis. Both rectangular and cylindrical channels can be accommodated in this analysis by proper choice of a geometry factor.

* 3M type 2214, 3M Company, St. Paul, Minn. 55119

** Obtained from Tyco, Inc., Waltham, Mass. 02154

*** G.E. designation AT-100 (Microwave Tube Operation, Tube Department)



Figure 5 - Cores and End Caps for Double-Conical Geometry Fuses (Conventional Bellows Configuration Shown at the Left)

TABLE I - SUMMARY OF SINGLE-CHANNEL DEVICES

<u>Fuse No.</u>	<u>Type of Design</u>	<u>Channel Material</u>	<u>Channel dia. x length</u>	<u>No. Tests</u>	<u>Disposition</u>
A1	Fig. 3	99% Alumina	.015 x .140	50	Channel eroded
A2	Fig. 3	99% Alumina	.015 x .140	55	Channel eroded
A3	Fig. 3	94% Alumina	.013 x .140	12	Channel fractured
A4	Fig. 2	94% Alumina	.015 x .110	21	Channel eroded
A5	Fig. 2	99% Alumina	.012 x .210	10	Dismantled
A6	Fig. 2	99% Alumina	.012 x .200	12	Dismantled
A7	Fig. 4	99% Alumina	.020 x .450	65	**
A8	Fig. 4	99% Alumina	.020 x .300	5	**
A9	Fig. 4	99% Alumina	.020 x .450	45	**
L1, L2	Fig. 4	99.8% Alumina	.018 x .300	~20	**
L3	Fig. 4	99.8% Alumina	.018 x .450	20	**
S1	Fig. 2	Sapphire	.020 x .300	30	*
S2	Fig. 3	Sapphire	.020 x .300	20	Channel fractured
S3	Fig. 2	Sapphire	.020 x .250	110	Dismantled
S4, S5, S6, S7	Fig. 4	Sapphire	.020 x .300	~10	**
S8, S9	Fig. 4	Sapphire	.020 x .450	~10	**
S10	Fig. 4	Sapphire	.009 x .240	50	*
S11	Fig. 4	Sapphire	.009 x .220	25	**
S12	Fig. 4	Sapphire	.020 x .450	20	**
S13	Fig. 4	Sapphire	.012 x .320	18	**

* Denotes fuses available for further tests

** Denotes fuses sent to NASA for evaluation

Based on this analysis and promising experiments conducted in devices with very small channels by Dr. C. A. Renton at NASA-ERC, a series of fuses with very narrow channels were fabricated and tested.

Three narrow-channel configurations utilizing sapphire for the channel material are shown in Figure 6. These devices, from left to right, respectively, have fuse channels formed from seven sapphire rods (see cross-section in Figure 7), two half-cylinders (see Figure 8), and 0.008-inch bore sapphire tubing. The latter device was made in the double-conical geometry configuration of sapphire tubing imbedded in glass, as described in the previous section. The former two configurations were fabricated into fuses by cementing a bellows section on each end using epoxy. A completed fuse is shown in Figure 9, its cross-section being similar to that shown in Figure 2.

Another experimental narrow-channel device was fabricated of quartz in the configuration shown in Figure 10, where the 19 channels vary from 0.001 inch to 0.003 inch across. The fuse was assembled as shown in Figure 2. Quartz was chosen because it can readily be fabricated into complex shapes, although quartz is a less refractory material than alumina or sapphire. Since the analytical picture of the arc mechanism derived in Appendix B predicts a lower temperature arc for the very narrow channels, a less refractory material should be usable for such devices.

Three earlier experiments with narrow-channel devices used one or more rods held on one end and positioned in a closely-fitted hole to form narrow channels. Two of these configurations are shown in cross-section in Figure 11. One of the fuse structures is shown in Figure 12 after test, when five of the seven rods were found to be broken after only eleven test firings. A third device was similar in structure to the one shown in Figure 12, with the exception that it incorporated one sapphire center rod 0.060-inch diameter, positioned in a 0.062-inch diameter hole in a sapphire piece, leaving a maximum channel width of 0.002 inch. In the two aforementioned fuses incorporating the 0.060-inch sapphire rods, the rods were broken after a few test firings, indicating that such structures would have to be supported over the full length of the fuse channel in order to withstand the transition forces. The fuse channel configurations shown in Figure 6, which fulfill this requirement, have performed well in resisting the mechanical forces caused by fuse operation.

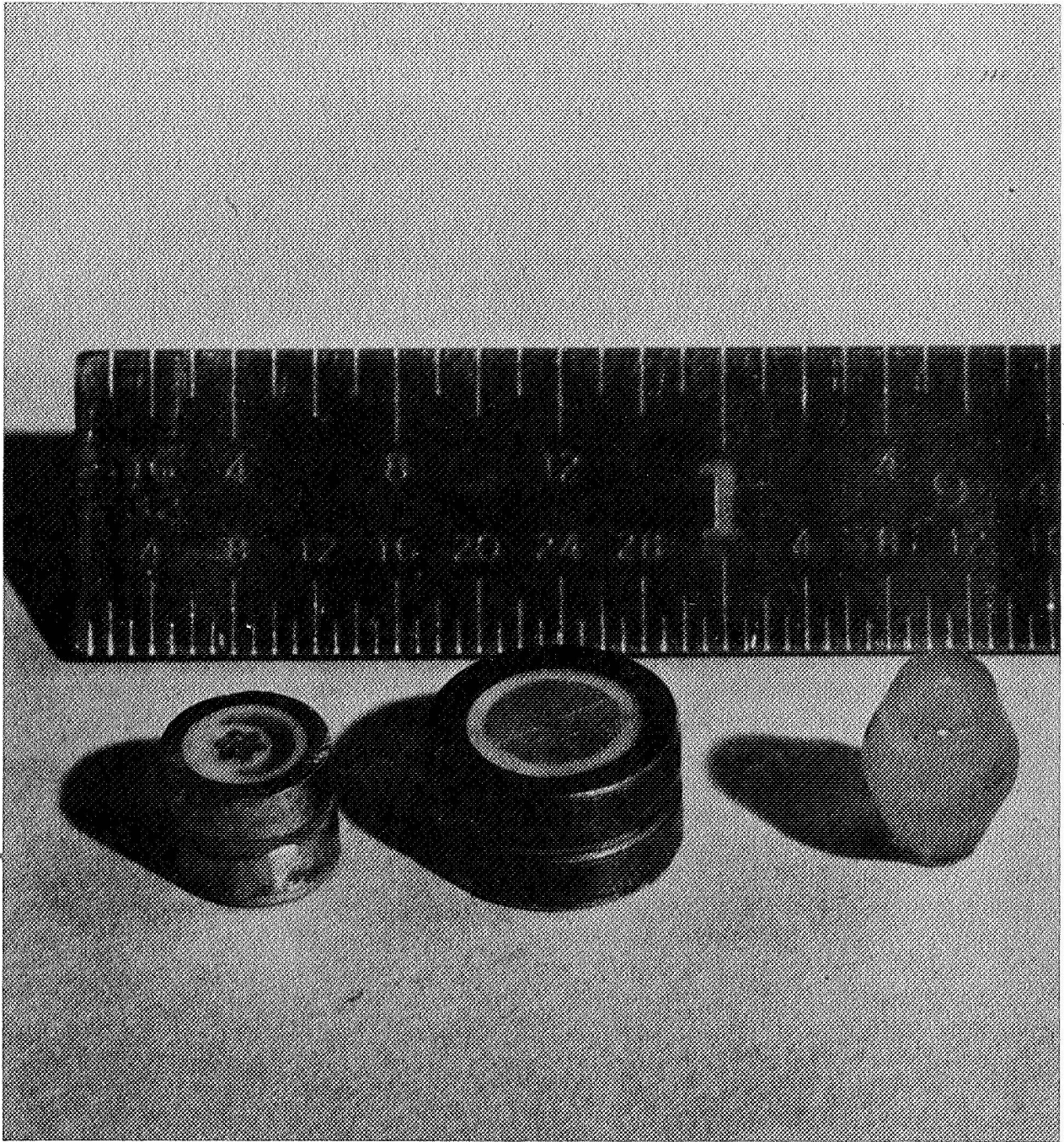


Figure 6 - Narrow-Channel Fuse Configurations Utilizing Sapphire Molded in Glass

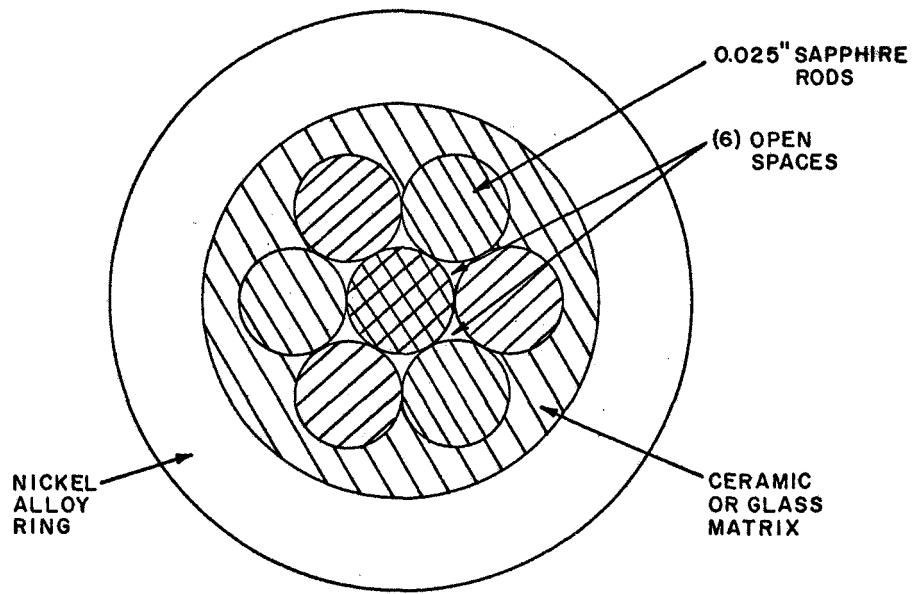


Figure 7 - Rod Matrix Fuse Configuration

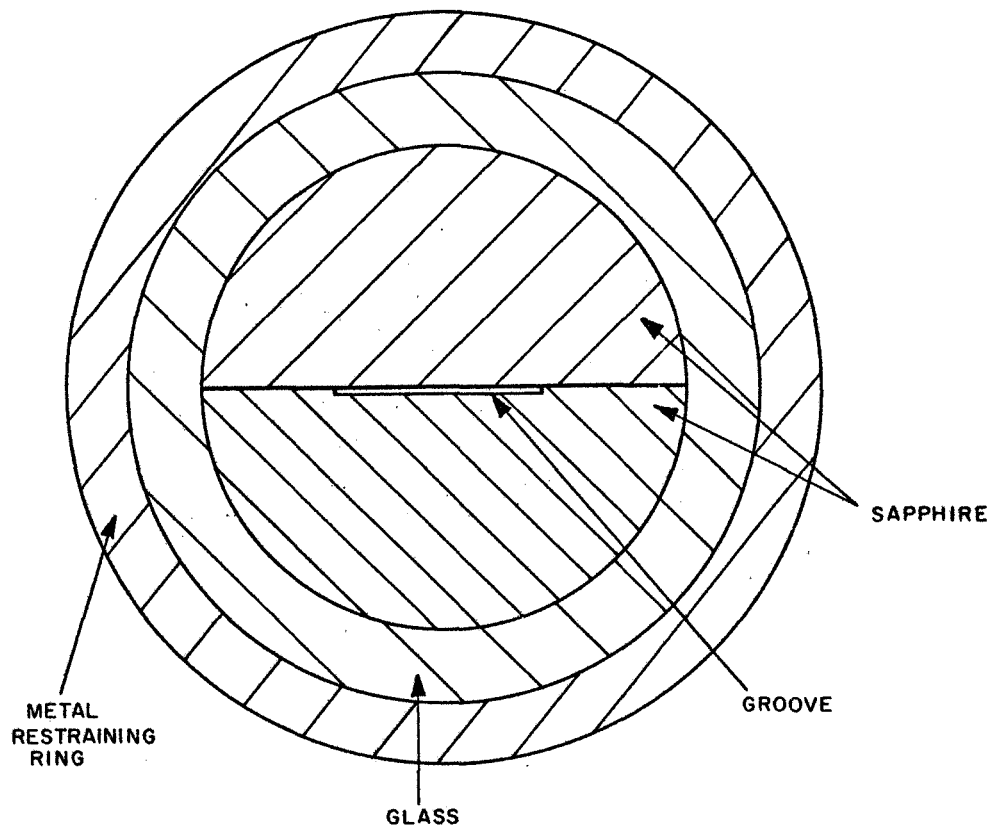


Figure 8 - Cross-Section of Split-Sapphire Narrow Channel Fuse

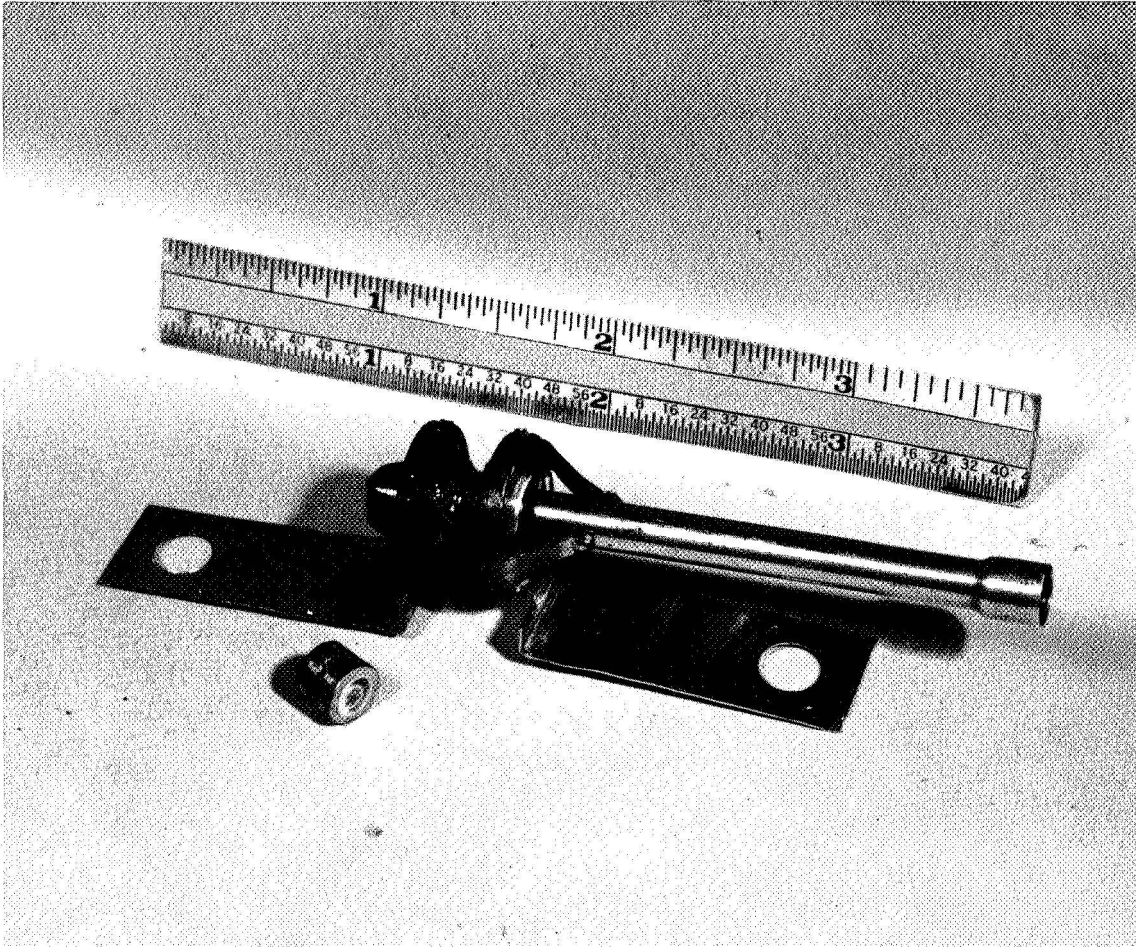


Figure 9 - Completed Narrow-Channel Fuse (Rod Matrix Structure Shown in Foreground)

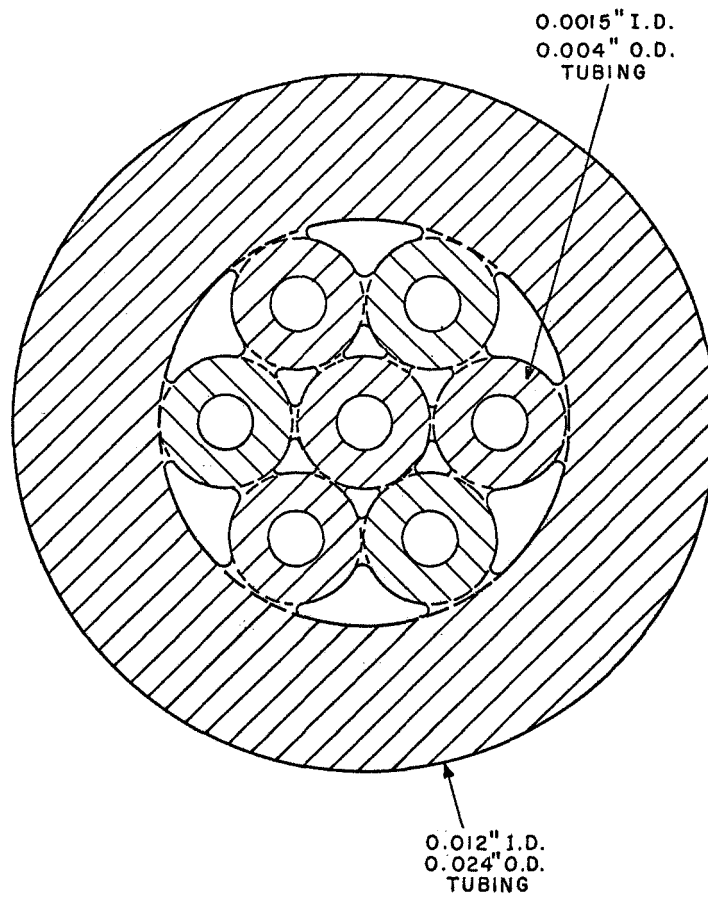


Figure 10 - 19-Hole Quartz Matrix Configuration

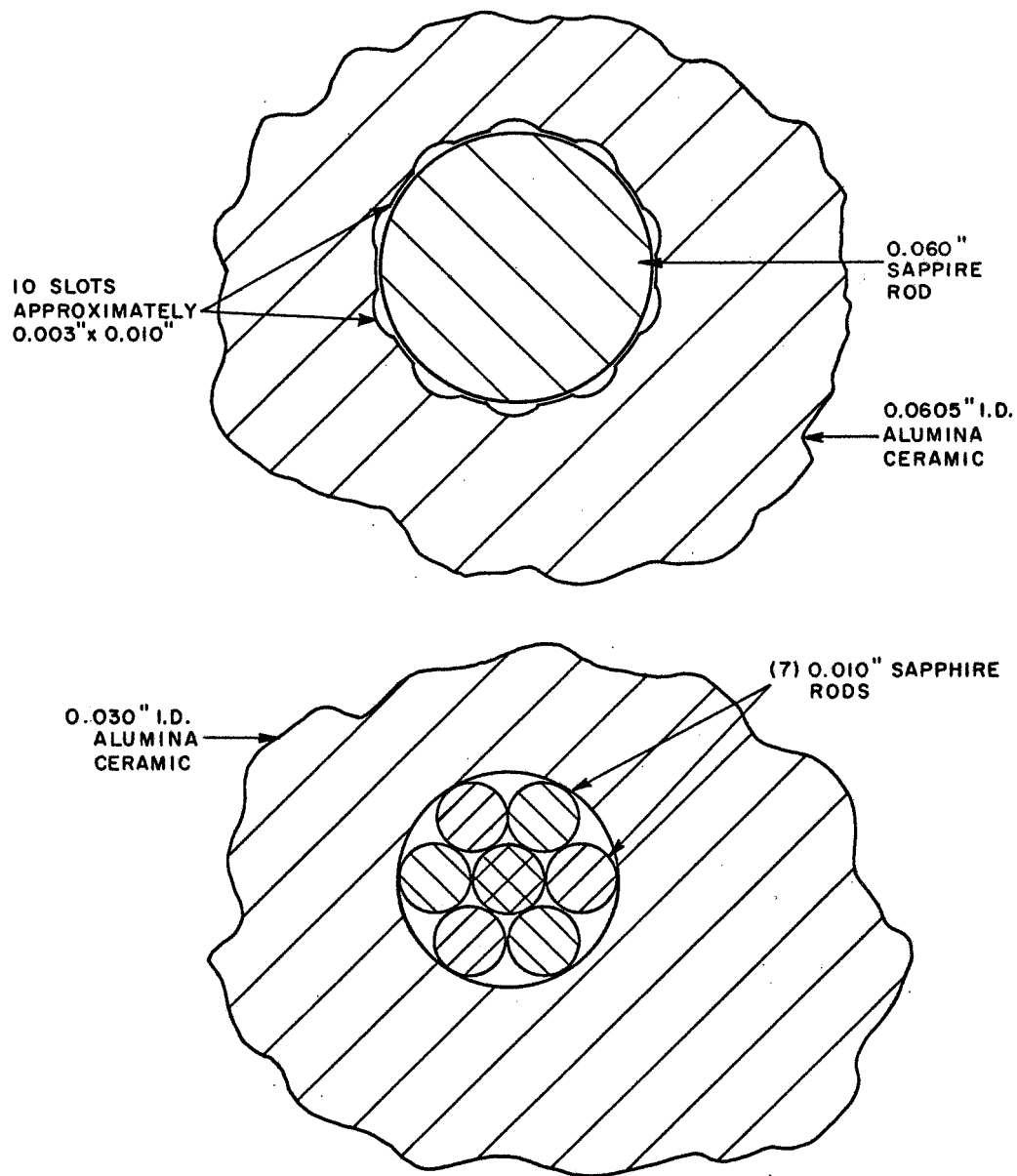


Figure 11 - Cross-Sections of Multiple-Channel Fuses
F1 (Top) and R1 (Bottom)

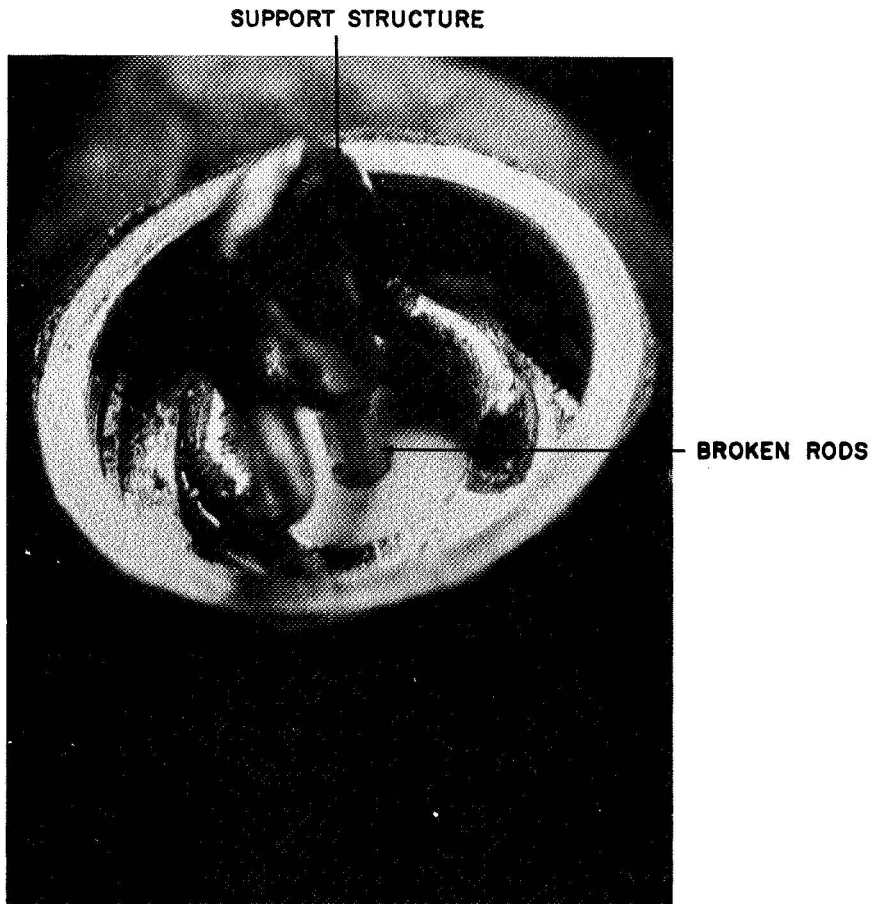


Figure 12 - Fuse R1 Structure After Test
(10X Magnification)

SANDWICH STRUCTURE DEVICES

Since refractory metals have definite advantages, both mechanically and thermally, compared to the brittle refractory oxides (refer to Appendix B), several techniques of utilizing molybdenum were evaluated. The designs evaluated were variations of a "sandwich" structure, shown in basic form in Figure 13. Two materials were used for the discs of the sandwich structure: molybdenum metal and a 50 percent alumina-50 percent molybdenum cermet. Since the cermet is an electrical conductor (approximately 1/10 the conductivity of molybdenum metal), either material requires intervening layers of electrical insulation. Of the materials tried as insulating layers, thin layers of fused glass or plasma-sprayed alumina were the most successful, while silicone rubber would withstand up to ten test firings with moderate compression applied along the axis of the fuse channel. Silicone rubber was not tried with heavy compression, but a several-fold improvement is considered feasible, based on tests of two devices insulated by silicone rubber.

The critical factor for the sandwich devices tested was the need for a good, continuous bond between the molybdenum or cermet disc and the insulating layer. This bond must be able to resist the strong forces tending to inject liquid mercury between these layers when the explosive transition forces occur, thus making it possible for the fuse layers to short. The glass-bonded molybdenum cermet sandwich will resist such forces. In this configuration, the cermet is heated with a torch to oxidize the molybdenum on the surface of the cermet and then the glass is fused between the cermet layers, under pressure. (A piece of stainless-steel tubing was used to keep the fuse channel open during the glass-bonding process.) The plasma-sprayed alumina structure also was bonded strongly enough to resist mercury injection by the transition forces. These devices were fabricated by plasma-spraying alternate layers of molybdenum and alumina. The alumina layers are approximately 0.003-inch thick, the molybdenum layers approximately 0.010-inch thick, and the fuse channel is a 0.020-inch diameter hole ground through the sandwich structure using a diamond dust slurry.

The sandwich structure fuses fabricated and subsequently given significant evaluation tests are described in Table II.

EXTERNAL FUSE STRUCTURE

The mechanical requirements for the external fuse structure are not stringent and consequently caused little difficulty. (The large per unit forces generated in the fuse channel cause only small net forces due to the very

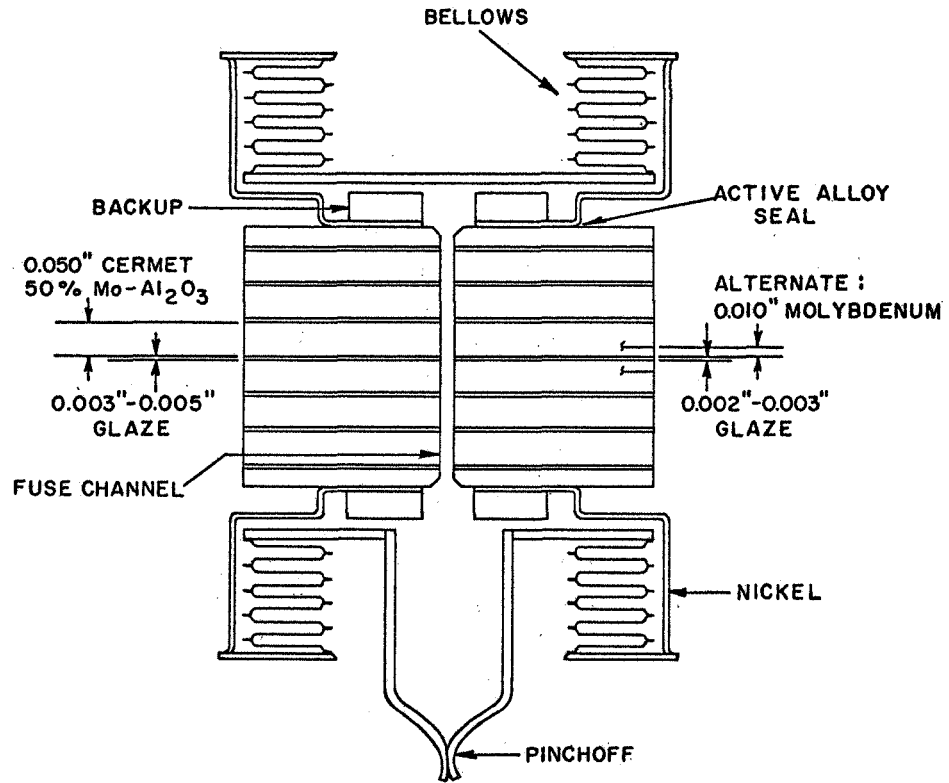


Figure 13 - Sandwich Structure Fuse Design

TABLE II - SUMMARY OF SANDWICH-TYPE FUSES

<u>Fuse No.</u>	<u>Insul. Mat'l.</u>	<u>Conducting Layers</u>	<u>Channel Dia. x Length (inches)</u>	<u>No. of Firing</u>	<u>Test Results</u>
M1	Glass	4	0.020 x 0.068*	35	Mo erosion nil
M2	S.R.	20	0.020 x 0.320	4	Several layers shorted
M3	S.R.	11	0.020 x 0.180	20	Several layers shorted
M4	P.S.A.	10	0.020 x 0.130	15	Insulator erosion
M5	G.A.	11	0.015 x 0.160	15	Several layers shorted
C1	V.G.	7	0.020 x 0.220	35	Two layers shorted

Where:

"M" fuses have molybdenum conducting layers

C1 conducting layers are cermet (50 percent molybdenum-50 percent alumina).

S.R. indicates Silicone Rubber

P.S.A. indicates "Plasma-Sprayed Alumina"

G.A. denotes No. 7052 glass over flame-sprayed alumina

V.G. denotes "Vitta" tape glass No. 1004 which is furnished as a powdered glass dispersed through a thin adhesive layer on plastic tape (Vitto Corp., Wilton, Conn. 06897)

* 0.030 inch diameter by 0.100-inch long alumina tubing at each end

small area of the channel.) The fuse structure, however, must supply gravity-independent restoring forces to force mercury back into the fuse channel after the fuse fires, and must also allow for thermal expansion and contraction of the mercury.

To accommodate these requirements, end buffer sections were provided on each end of the fuse, consisting of a rigid cup and a flexible bellows in a convoluted configuration, as shown in Figures 1 and 4. Some fuses were also fabricated using a more conventional bellows design, shown in Figure 5. The latter design, which is somewhat more flexible, may be the preferable design, although both performed properly for the devices tested.

Because the transition forces are of very short duration, the impact effects of the force are quite high, and the bellows structure will be distorted unless some added restoring force is provided. This can be accomplished by adding the restraint structure shown in Figures 1 and 4, which limits the impact-induced flexing of the bellows but allows the bellows to move the required 4 percent (in volume) to provide for thermal expansion of the mercury. Using a heavy spring instead of a rigid post is considered more reliable for this structure, and some fuses were fabricated using such a structure. This version is shown in Figure 2.

An improved seal-off technique was also developed. In earlier fuses, the seal-off technique used to seal the tubing required to evacuate the device and fill it with mercury had utilized a "weld-pinch" procedure. This technique, widely used to seal off mercury-loaded electron devices, consists of mechanically pinching the tubing closed and then resistance-welding the pinched section. The weld-pinch performed well as a seal-off technique, but a few devices failed to seal properly. This apparently resulted when mercury became trapped by the pinch action, subsequently "exploding" when the weld was made. This problem was corrected by changing to a new technique which provides a good seal-off without welding. This technique involves coating the interior of the tubulation with a thin layer of silicone rubber (shown at the left in Figure 14) during fuse fabrication. When the fuse is ready for sealing-off, the tubing is flattened and folded, as shown at the right in the figure to effect a seal. This seal-off technique was applied to most fuses shipped to NASA.

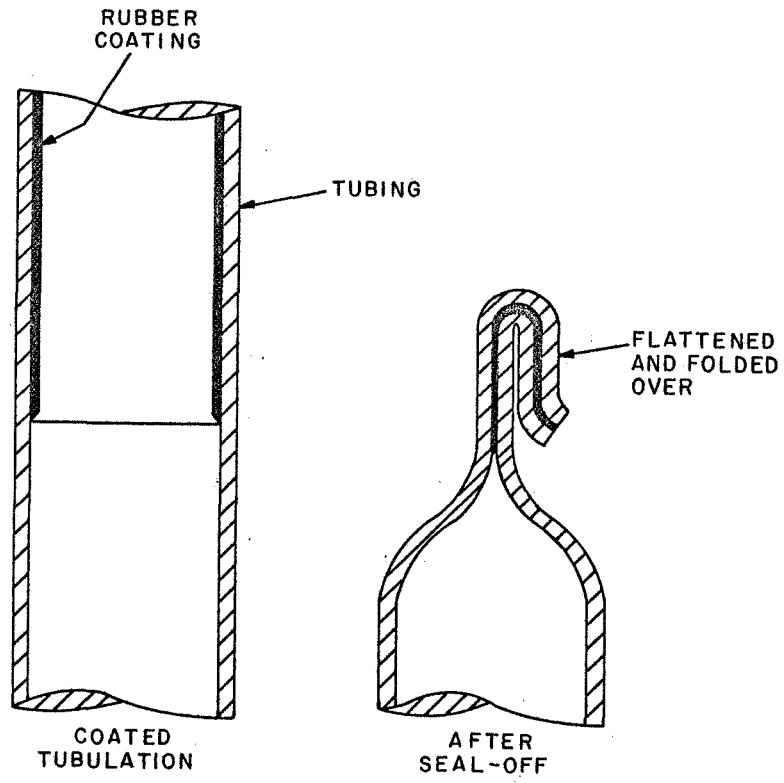


Figure 14 - Silicone Rubber Seal-Off Technique

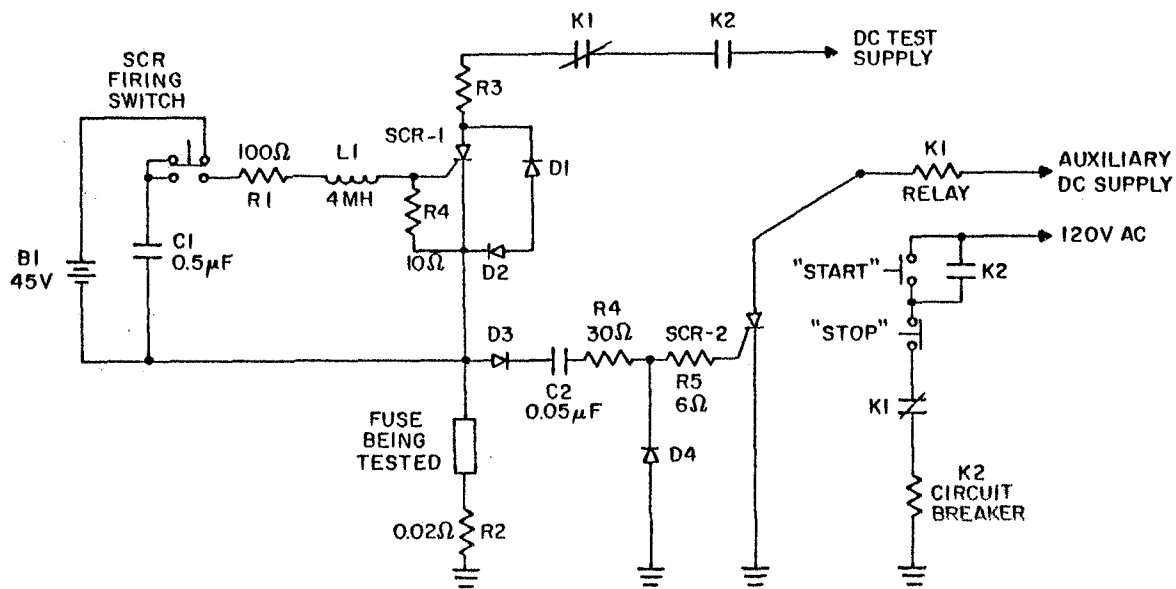
TEST AND PROCESSING APPARATUS

The principal objectives of testing the experimental fuses investigated in this program were (1) realistic evaluation of their circuit protective capabilities, and (2) comparison of the performance of various fuse designs and materials. A "standard" circuit was thus used for most fuse tests, because the circuits in which fuses are applied influence fuse operation in important ways, ie., circuit parameters determine fault current rise time, the maximum fault current, and the transient overvoltage and energy the fuse must accommodate during the transition stage.

Since one principal application of such fuses would be the protection of solid-state devices, the simulated fault current was passed through a silicon-controlled rectifier (SCR); which was also utilized to switch the fault current during the testing. The circuit devised for evaluating fuse performance is shown in Figure 15. The fault current first passes through R3, a variable resistor bank, SCR-1, then to the fuse being tested and subsequently current-viewing resistor R2. The test is initiated by a simple switch-actuated single-pulse circuit, consisting of B1, C1, L1 and R1, which actuates SCR-1. The protective circuit is triggered by coupling to the very fast-rising voltage that appears across the fuse when it interrupts the simulated fault current. This voltage, suitably attenuated, actuates SCR-2 and thereby relay K1. The light (10-ampere rated) K1 contacts open to properly interrupt the current for tests in which the fuse arc state persists beyond approximately 0.008 second. For most fuse tests the fuse current goes to zero (or a very low current) allowing SCR-1 to switch off before the K1 contacts open.

Circuit breaker K2 protects the circuit from being damaged during the occasional fuse or circuit failures. The K2 contacts open after the normal "dropout" time of approximately 0.04 second, following the actuation of the protective circuit described above. For fuse test where the fuse arc state current was allowed to persist for 0.04 second, the K1 contacts were bypassed.

Figure 16 depicts the test apparatus. The cage-enclosed (for safety purposes) apparatus is an existing test facility which includes metering, switching, circuit breakers, variable resistor bank R3, and associated circuitry. The SCR panel includes the other test circuitry except for the fuse under test, which is enclosed in the fuse test box. The fuse test box eliminates the possibility of injury that might result from flying pieces of an exploding fuse and contains most of the toxic mercury vapor which would otherwise escape if a fuse failed. The clear plastic top permits visual observation of the fuse and the light from the fuse arc during testing.



Where:

- SCR -1 = Type C-35 Silicon Controlled Rectifier
- SCR -2 = Type C22AR66
- D1, D2, D3, D4 = Diodes Protecting SCR's from Overvoltages
- D1 = 1N1362 Zener Diode (20 V)
- D2, D3 = 4 JA27P Diodes
- D4 = 1N1523 Zener Diode (10 V)
- K1 = GE Cat. No. 2790-E100A2 Relay
- K2 = Custom-made Circuit Breaker
- R3 = Variable Resistor Bank
- R2 = Viewing Resistor

Figure 15 - Test Circuit for CSCL Devices

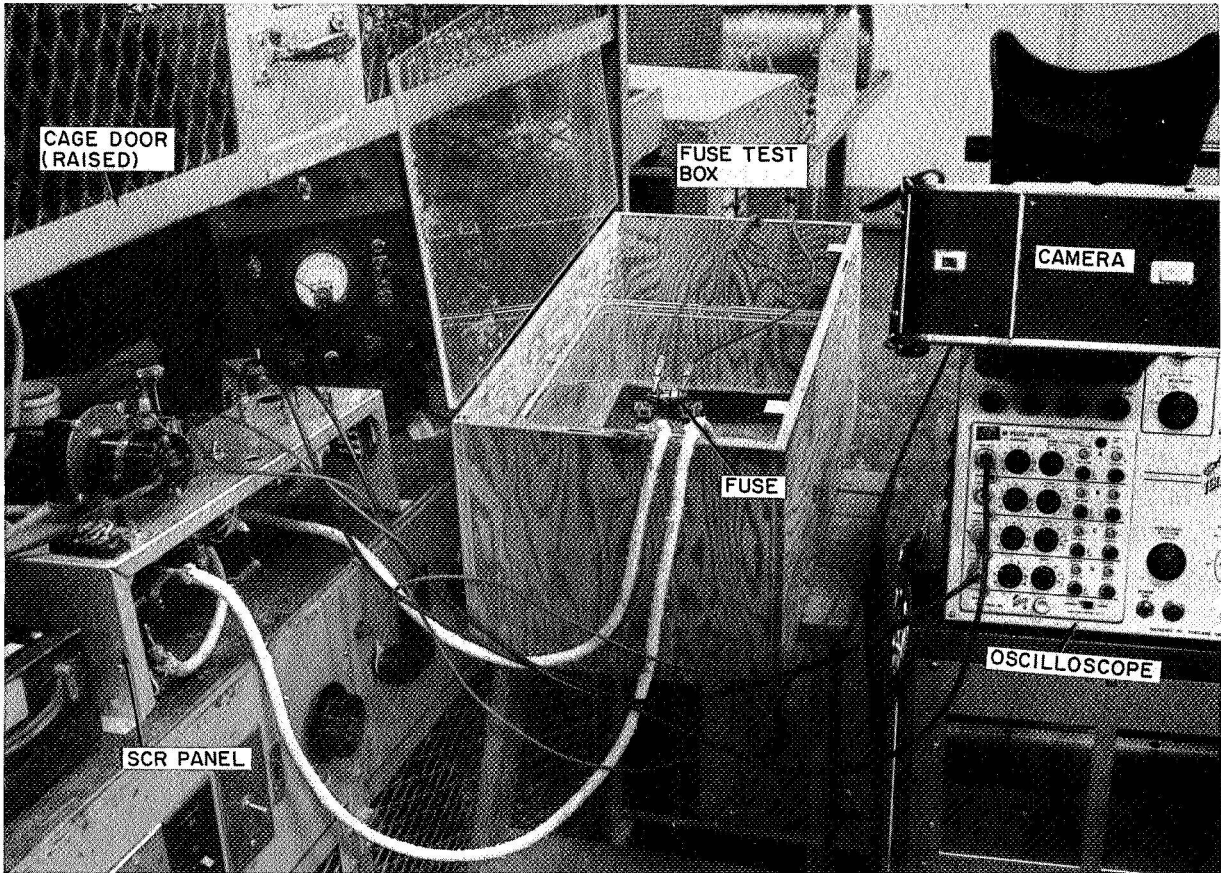


Figure 16 - Fuse Test Apparatus

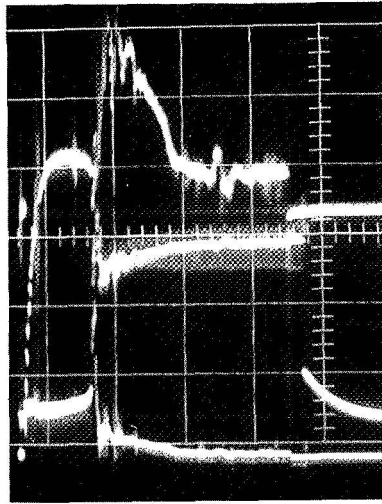
The oscilloscope and camera were used to monitor the fuse current and voltage. Three oscilloscope traces were used -- one to measure the "fault" current for each test, one the arc current, and one the fuse voltage. A typical oscilloscope picture is shown at the top of Figure 17, with the current and voltage traces redrawn as separate curves at the bottom. The traces are overlapping in the photo to enable greater resolution of the traces. The upper trace in the photo records only the smaller currents of the arc state -- typically 3 to 25 amperes -- and enables accurate measurement of the arc impedance, compared to the lower trace which records the "fault" current and has a resolution typically 1/10 that of the upper trace.

The dc supply voltage consisted of a bank of ten 12.6-volt automotive lead-acid batteries for most of the fuse tests conducted. This supply, shown in Figure 18, is a very convenient low-impedance source, with an internal resistance of approximately 0.1 ohm and an inductance of approximately 5 μ H due to the connecting leads. The other circuitry contributed at least 10 μ H of lead inductance, or 15 μ H minimum inductance for these fuse tests. A selector switch provides a range from 36 to 120 volts, in 12-volt steps. Tests were also conducted using a 6-phase rectified (60-Hz ac) supply with an internal resistance of 0.1 ohm, a 150- μ H inductance, and a voltage variable from 0 to 80 volts dc. A 125-volt plant-wide dc supply line was also used for some tests. This supply has an internal resistance of 0.2 ohm and an inductance of 300 μ H. The inductance-limited response time of the battery-bank supply was comparable to the performance of modern solid state fast-acting circuits and therefore was more appropriate for fuse tests than the more inductive supplies. For example, higher peak fault currents are experienced by fast-acting circuits.

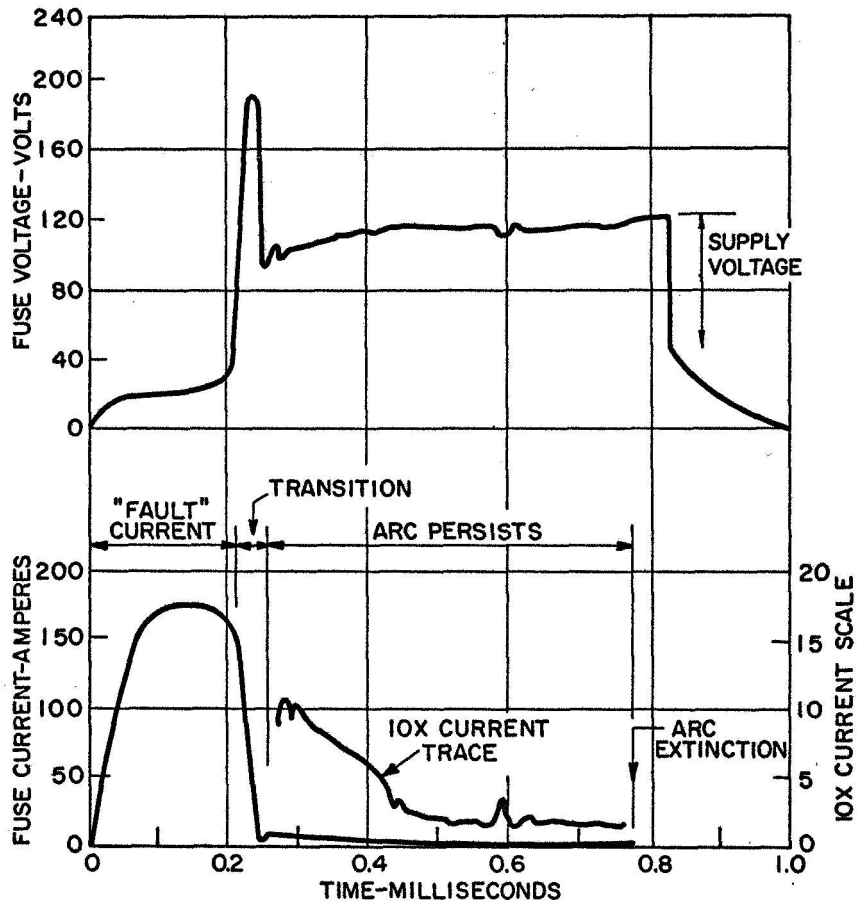
PROCESSING EQUIPMENT

Existing vacuum equipment was adapted for use in processing these fuses, ie. for evacuating fuses and loading or unloading the mercury fill. The processing station depicted in Figure 19, consists of a mechanical vacuum pump, liquid nitrogen trap, vacuum gage, glass valve, and rotatable glass mercury-loading adapter. The glass assembly is heated by heating tape* to "outgas" the glass and to redistill mercury to obtain mercury of very high purity when desired (no improvement in fuse performance could be noted when commercial triple-distilled mercury was redistilled). The liquid nitrogen trap improves vacuum pressure as well as effectively preventing mercury from contaminating the vacuum gage and pump.

*"Briskeat" No. B-2 1/2 tape, Briscoe Mfg. Company, Columbus, Ohio



(a) Photograph of Oscilloscope Traces



(b) Waveforms Separately Redrawn

Figure 17 - Current and Voltage Waveforms for a Typical Fuse Test



Figure 18 - Battery DC Voltage Supply

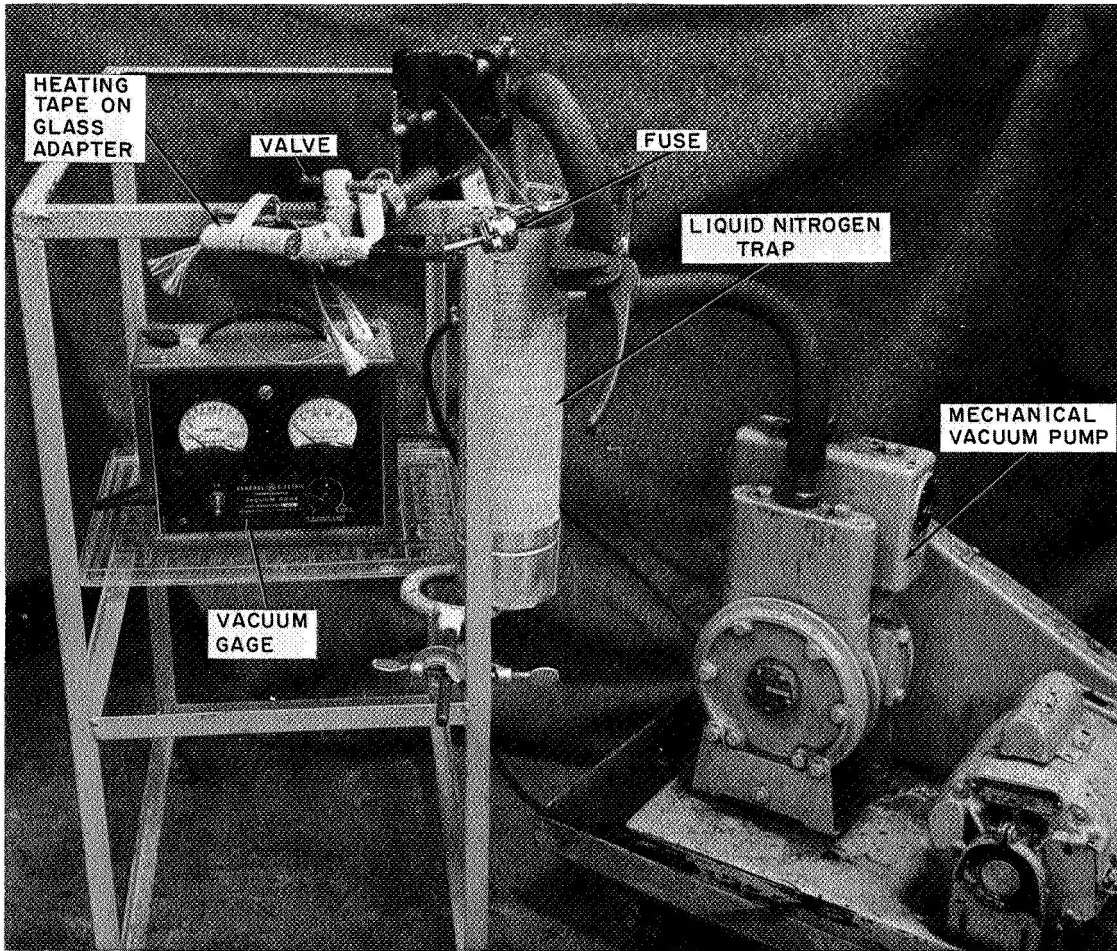


Figure 19 - Fuse Processing Apparatus

TEST PROCEDURES AND RESULTS

The test procedures used to evaluate fuse performance have been separated into five sections for convenience of reporting: (1) Circuit protection capability, (2) effects of transition explosion, (3) impedance of current-limiting arc, (4) thermally-induced bore erosion, and (5) multiple-channel devices. These procedures and test results are discussed in this order in the paragraphs that follow.

CIRCUIT PROTECTIVE CAPABILITY OF SELF-HEALING FUSES

The primary protective function of current limiting devices such as those investigated here is to limit the energy that other circuit devices are subjected to during circuit faults. This investigation has been limited to the protection of solid-state devices. The energy limit for solid-state devices due to joule heating of the junction is usually defined by an I^2t rating, where I is fault current in rms amperes and t is the fault duration time in seconds. This applies for a range from approximately 10^{-5} second to 10^{-2} second. For shorter periods, the time rates of change of current or voltage become the more important factors for solid-state devices due to carrier drift velocity limitations. For faults of longer duration, heat capacity and heat conduction of the structural members become important both for current limiters and solid-state devices. Figure 20 illustrates this energy relationship, including an approximate transition toward the steady-state rating for three typical solid-state devices and actual test performance of three fuses. These curves show that adequate protection for the 25-ampere SCR can be provided by the 0.020-inch "family" of fuses, while the 0.014-inch fuse would be applicable for the 7-ampere SCR. Fuse R3 illustrates the performance of a fuse of a non-circular bore cross-section. Inherently, such fuses have a mercury channel of larger wall area but smaller volume, for an equivalent fuse rating, as compared to a circular cross-section. Thus, the I^2t ratings of non-circular cross-section devices tend to be lower at high currents and the fuse R3 curve approximately represents the energy-limiting characteristic of most narrow-channel fuses tested.

Figure 20 also provides a convenient means of approximating the I^2t energy for each test, since the rms "fault" current can be readily approximated from the photographed oscilloscope trace made for most fuse tests, and the time can be directly read from the trace. By plotting the current and time on Figure 20 and extrapolating between the constant I^2t lines, a good approximation of the I^2t energy for the fuse test is easily obtained.

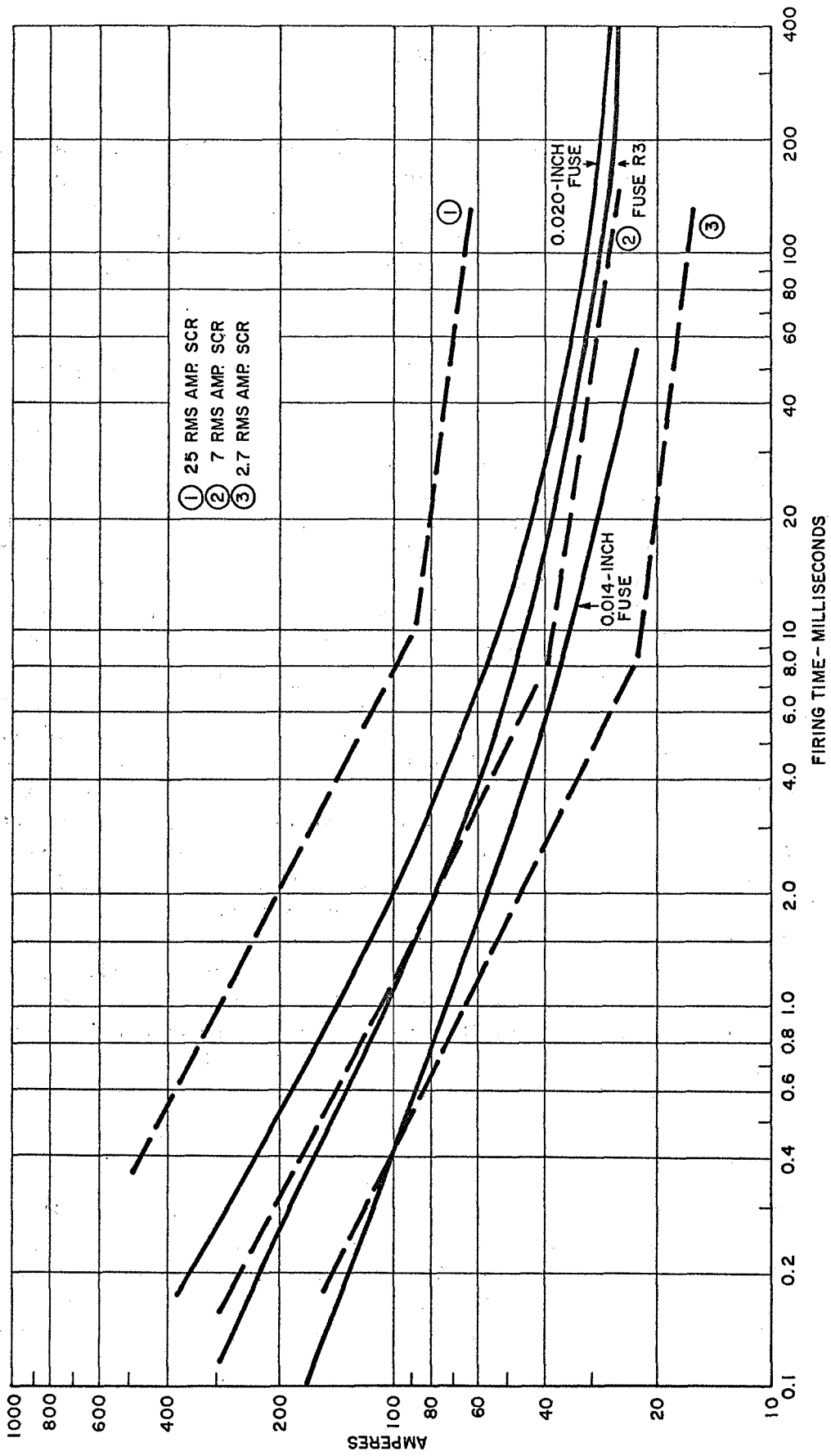


Figure 20 - Fuse Performance and SCR Protection Requirements

Two mechanisms primarily determine energy limiting characteristics of the fuse. These are specific heat capacity of the mercury in the fuse channel and heat conduction from the mercury in the channel to the walls of the fuse channel. Specific heat dominates for firing times of about one millisecond or less, and heat conduction dominates for times longer than 100 milliseconds with curved transition between these sections as shown in Figure 20.

The effects of current conducted by the fuse during the current-limiting arc state is neglected in the energy limiting considerations described above. This is usually a very good approximation for these fuses because the current during the arc state is usually comparable to the normal circuit current and thus contributes little energy during the occurrence of a circuit fault. The arc also often extinguishes itself after a very short time (10^{-3} second or less).

EFFECTS OF THE TRANSITION EXPLOSION

The principal experimental and analytical efforts during this program were directed toward evaluating the two major factors governing the durability of the fuses: (1) the device must mechanically withstand the explosive transition forces, and (2) the bore materials must resist erosion due to the large flux of heat energy generated within the fuse bore during fuse operation (refer to "Thermally Induced Bore Erosion" subsection).

Based on earlier work with self-healing fuses, it was logical that the more complex of these two factors would be the bore erosion factor. Consequently, most of the fuses fabricated were more heavily restrained than necessary in order to eliminate "explosion" failures, which will usually badly damage or destroy a fuse, thus allowing more opportunity to evaluate bore erosion.

Explosion forces also can generate comparatively minor damage which is cumulative with each test operation, in a manner similar to the effects of heat-induced erosion on fuse performance. Two of the molybdenum sandwich devices described previously, fuse C1 and fuse M4, performed in this manner during fuse tests. Enlarged sections showing the bores of these fuses after testing are presented in Figure 21 for fuse C1 and Figure 22 for fuse M4. Visual microscope examination of these sections indicates that cracking and chipping of the brittle insulating layers, caused by the explosive transition forces, contributed to the erosion of the insulating layers.

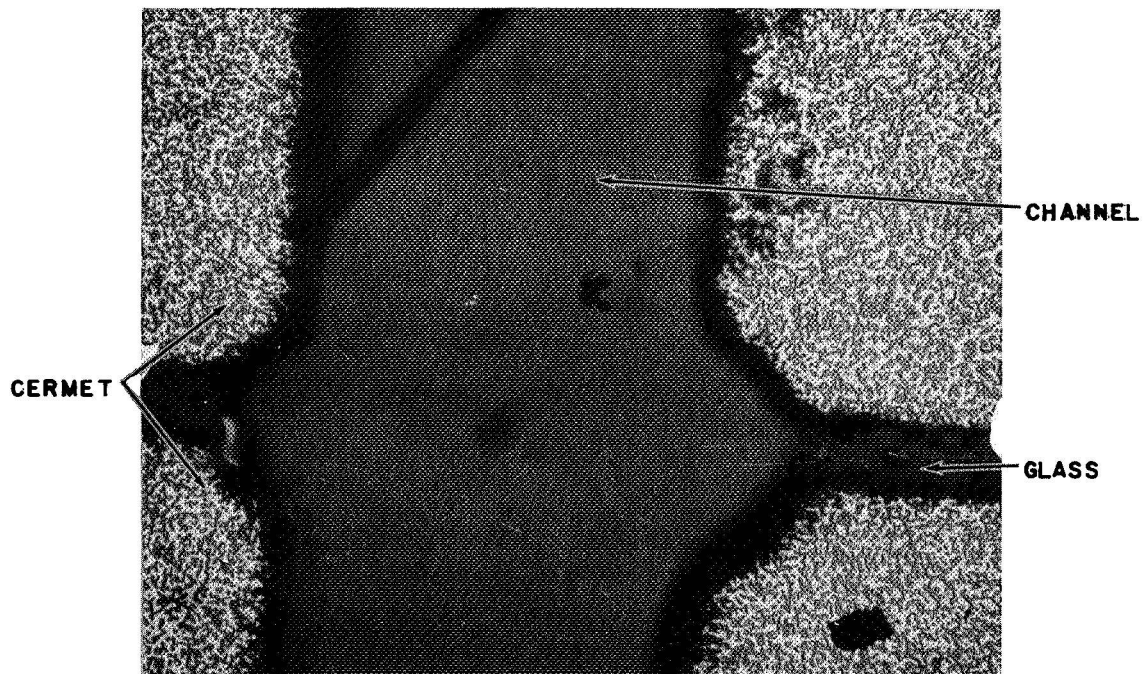


Figure 21 - Section of Fuse C1 Channel After Test
(100X Magnification)

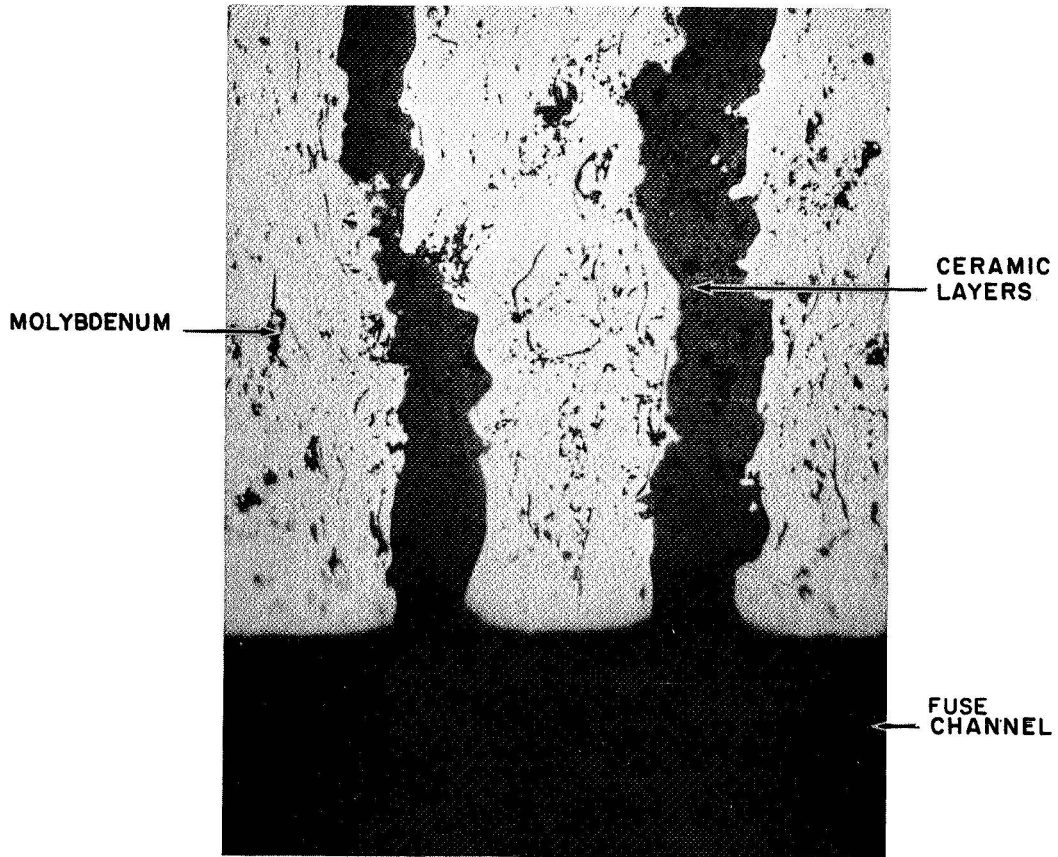


Figure 22 - Plasma-Sprayed Molybdenum-Alumina Sandwich of Fuse M4 After Test (180X Magnification)

The bore of fuse S3 was similarly cracked and chipped when examined after test. Fuse S3 was a sapphire cylindrical-bore type tested early in the program.

The performances of these fuses during testing, in terms of bore enlargement, are illustrated in Figure 23. The bore enlargement or erosion is represented by the lowering of the electrical resistance of the mercury in the fuse bore, which accurately measures the average cross-section of the bore. The approximate heat energy absorbed by the fuse bore is calculated as the sum of 2/3 the electrical energy dissipated during the transition explosion and all the energy dissipated by the fuse arc. These energies are calculated from the oscilloscope traces recorded at the fuse test.

The 2/3 factor is estimated by reasoning that 20 percent of the transition energy is expended in mechanically ejecting mercury from the arc channel during the transition explosion, which lasts less than 10^{-4} second. During this short period, the atomic density in the arc channel decreases by about a factor of 100, from the density of liquid metal to that of an arc of a few atmospheres pressure and perhaps $15,000^{\circ}\text{K}$ temperature. At least 0.01 eV of energy must be imparted to each mercury atom expelled from the channel to move it 0.5 cm in less than 10^{-4} second. The atoms remaining in the channel require a vaporization energy of about 0.6 eV per atom, a thermal energy of about 2 eV, and, with 10 percent ionization, 1.25 eV per atom for ionization and electron thermal energy. Thus, if other energy sinks have negligible effect during the transition, approximately 20 percent of the input energy must be expended in mechanically pushing material from the arc channel into the buffer volumes at the ends. Since most of the 0.6-eV vaporization energy is absorbed by the liquid mercury when it is returned to the fuse channel, the channel walls absorb the remainder, approximately 2/3 of the transition energy. After the transition, all the arc energy is absorbed by the channel walls because the energy situation is in comparative equilibrium and all energy input is continuously dissipated at the channel walls.

The behavior of fuse A2 shown in Figure 23 is considered to have resulted from extensive thermally induced bore erosion during testing. Fuse A2 was fabricated in the configuration of Figure 3, with commercial alumina of 99 percent purity as the bore material. The behavior of fuse S3 is shown here because the bore of this sapphire cylindrical bore fuse was more obviously cracked and chipped than other sapphire bore fuses tested. The surface of the fuse S3 bore is believed to have been cracked and weakened during operation prior to the sudden change shown in Figure 23, and the bore

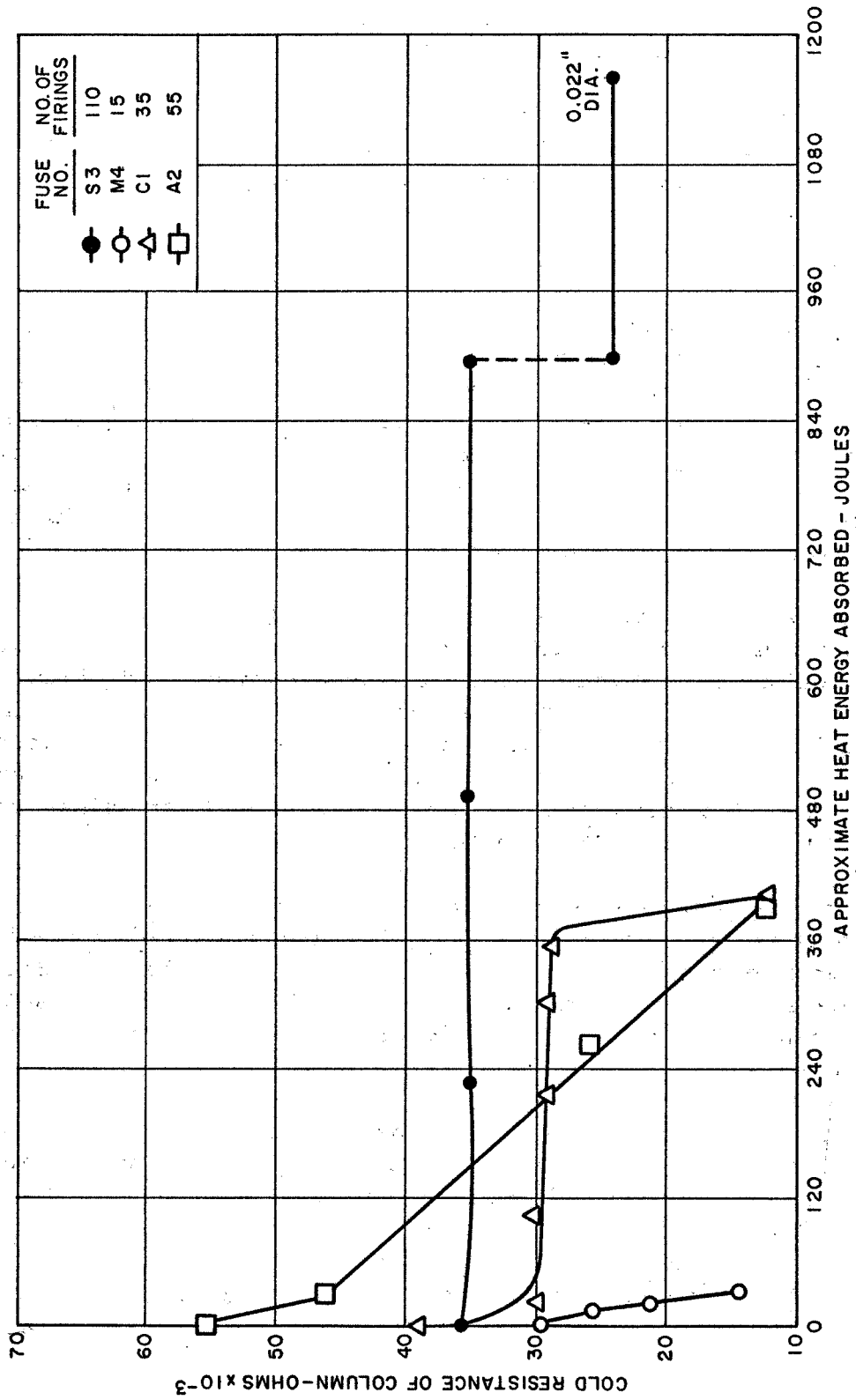


Figure 23 - Changes in Resistance with Fuse Operation I

material was then loosened and ejected from the bore during one of the fuse tests. Fuse S3 was fabricated in the configuration of Figure 2, using epoxy, which provides only moderate restraint to the sapphire and thus is more likely to experience mechanical damage.

When the fuse channel material was well restrained by the fuse structure and suffered very little mechanical damage during fuse testing, better data pertaining to bore erosion were obtained.

IMPEDANCE OF CURRENT-LIMITING ARC

The high impedance characteristic of the stable arc in narrow channels has been generally demonstrated by the narrow-channel devices tested. Figure 24 depicts the ratio of the impedance of the stable arc to the cold resistance of the liquid mercury, as a function of channel width for several experimental fuses. The data represent tests where the arc would persist for times on the order of 10^{-3} second, or until the arc was generally stable, as is shown by the oscilloscope trace. The "theoretical" arc impedance is derived from Figure 36 Appendix A.

The data illustrate the variable behavior of the stable arc for different devices, in that the average data shown in Figure 24 differ as much as 2 to 1 for different devices of essentially the same materials and geometry. Each device is comparatively consistent in its average performance, although the arc impedance varies with time over a 3 to 1 range for a given test firing of an individual device. The lower extreme in impedance would generally occur at about 10^{-4} second after firing (just at the end of the transition stage) and the higher extreme at 10^{-2} second or later.

There is also reasonable agreement between the theoretical and experimental performance for these devices, in that the ratio of theoretical to experimental impedances is approximately 1.8 for the data obtained. This is considered good agreement for an analytical treatment that uses a number of simplifying assumptions to provide approximate characteristics for such arc discharges.

The arc impedance was found to decrease with time for a few of the fuse tests recorded, contrary to the usual experience described above. For most of the test firings where the arc impedance decreased with time, it could also be established that the fuse channel was simultaneously being enlarged appreciably due to thermally induced bore erosion. Logically, the reason for the decreasing arc impedance would be the widening of the arc

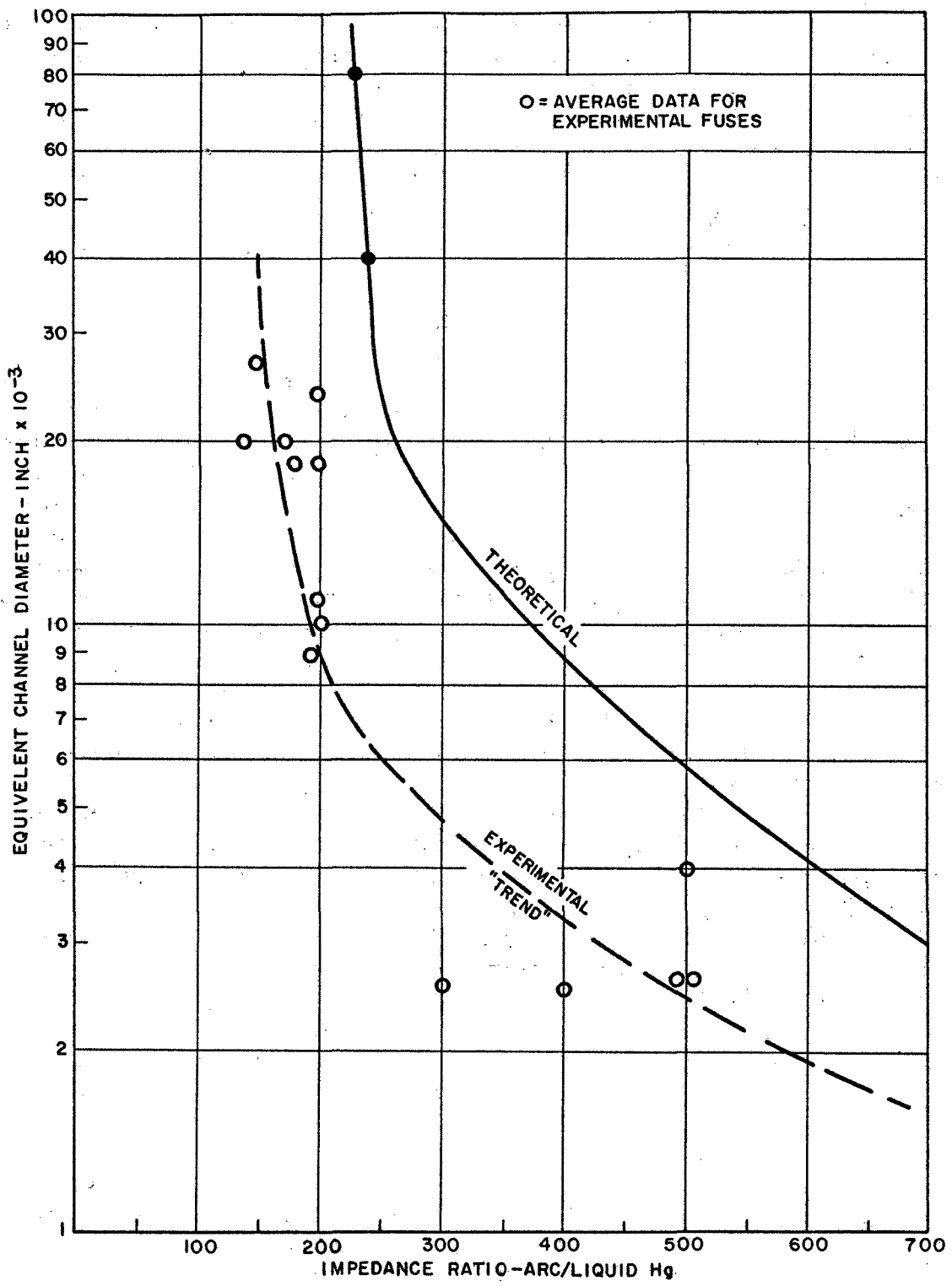


Figure 24 - Ratio of Arc Impedance to Liquid Mercury Resistance for Various Channel Diameters

channel. (Material evaporated off the channel would tend to cool and constrict the arc and thus increase impedance, and very few of the atoms likely to be present in these vapors would tend to reduce arc impedance appreciably.) The decreasing arc impedance can be noted in the fuse test current and voltage waveforms shown in Figure 25 for fuse S10. The impedance changed from approximately 22 ohms to 13 ohms in the 22 millisecond duration of the arc for this test firing. Further, the fuse bore was enlarged from 0.010 inch to 0.015 inch in diameter during this test firing.

THERMALLY-INDUCED BORE EROSION

In considering the complex mechanisms responsible for thermally induced bore erosion, there is one simplification that can be readily derived i.e. the thermal effects of the transition explosion are slight for materials as refractory as the high purity aluminas. Analytically, it can be calculated that, for a 100-volt low-inductance circuit that will provide 500 amperes of short-circuit current, less than 3 joules of thermal energy must be accommodated by the fuse bore, based on the mechanisms described earlier in the "Transition Explosion" discussion. Experimentally, it has been found that almost all thermal bore erosion occurs when the arc persists for times on the order of 10^{-2} second.

This factor makes the tendency of the fuse arc to be self-extinguishing important for reasons other than the fault-clearing function described earlier under "Circuit Protective Capability". For example, a fuse with a typical cold resistance of 0.04 ohm and an impedance ratio of 250 would limit the arc current to 10 amperes in a 100-volt circuit. This requires the fuse channel to dissipate 1 joule per millisecond. Thus the total thermal energy is doubled in 3 milliseconds, tripled in 6 milliseconds, etc. In five to ten milliseconds this massive energy input rate begins to overcome thermal inertia and the surface temperature increases more rapidly. (This time factor is also seen in the I^2t curves of Figure 20.) Evidence from fuse tests indicates that most bore erosion takes place when the arc persists 10 milliseconds or longer. The higher impedance ratio is also important in limiting thermal energy, of course -- a 500X ratio device having half the energy rate of 250X device.

The advantage of operation where the arc is self-extinguishing is well illustrated in Figure 26 for fuse A7. The test circuit SCR was bypassed for this test so the fuse continued to pass current until the protective circuit relay opened, and the fuse reclosed and refired twice after the initial firing. The striking factor in such test firings is the rapid reduction in circuit energy allowed by successive fuse firings.

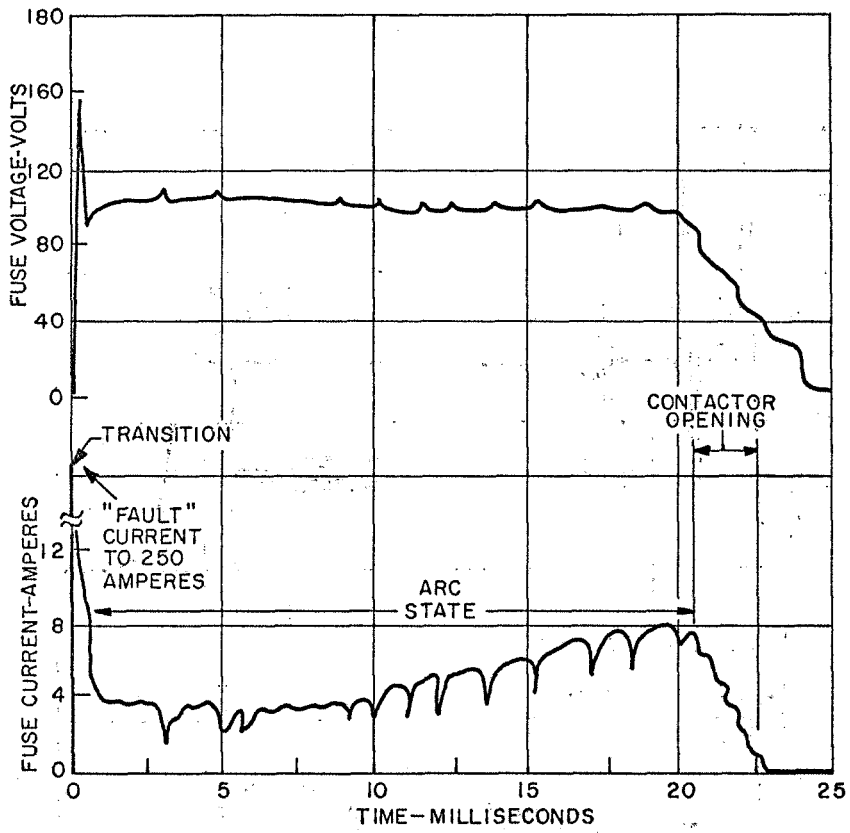


Figure 25 - Current Voltage Waveforms for S-8 Showing Decreasing Arc Impedance

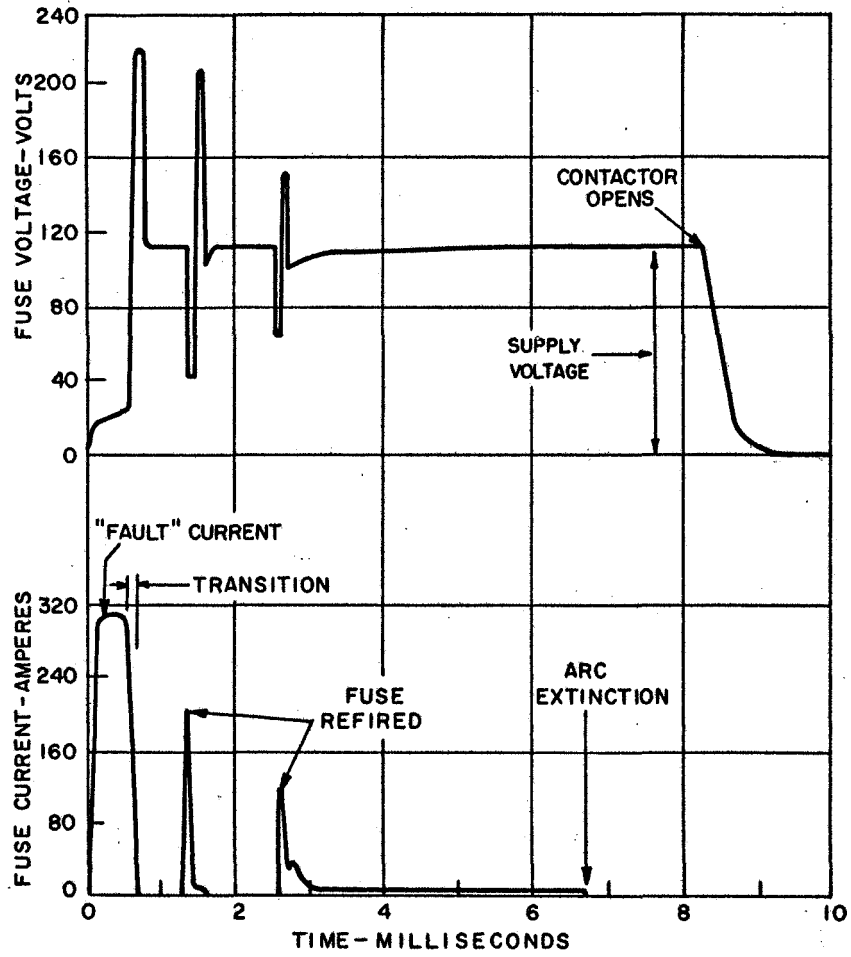


Figure 26 - Current Voltage Waveforms for Fuse A7 Showing Fuse Refiring

The I^2t energy was .4 joules for the first firing, 2 joules for the second, and 1 joule for the third. The time between firings also tended to increase. By contrast, the energy dissipated in the fuse bore during the arc stage alone was 3 joules, even though the arc was of unusually high impedance for a 0.024-inch diameter cylindrical bore fuse during this test firing. The bore experienced about 0.3 joule per millisecond when extinguishing and refiring, or about 0.7 joule per millisecond when the arc state persisted, as shown in Figure 26. The more usual fuse operation for arc self-extinction is shown in Figure 27 where arc extinction occurred at the end of the "transition" stage and the circuit SCR switched off the current.

The tendency of the arc to extinguish is greater when the arc is unstable, and the instability for a given device should be a function of the fuse voltage gradient imposed by the circuit. This relationship is represented by the arc behavior predicted in Figure 36 where the unstable behavior is expected for operation at voltage gradients below the curve for the channel width of the device. Experimentally, it has been demonstrated that specific fuses are reasonably consistent in their arc extinction characteristic, such that there is a voltage threshold above which more stable arc behavior is experienced. However, different devices of very similar geometry behave differently, leading to some inconsistency in this voltage relationship.

There is also an appreciable difference between the arc extinction behavior of sapphire fuse channels and other less refractory channel materials. Such arc extinction characteristics are shown in Figure 28 for a group of representative fuses, where the average threshold voltage gradient for arc stability is plotted as a function of channel width. The data indicated that the difference in arc extinction between sapphire devices and alumina devices is appreciable for the wider channels but may be slight for the very narrow channels, although consistent data were obtained from only one such alumina device. The one quartz device tested also exhibited similar behavior, as is shown in Figure 28.

The rate of thermally induced erosion was very difficult to define accurately because of the erratic behavior of the arc, which made it very difficult to predetermine the amount of energy for any single test operation. The data considered to be most representative of thermally-induced erosion are shown in Figure 29, which is similar to Figure 23 except for the "joules" scale. As in Figure 23, bore enlargement is represented by lowering of the electrical resistance of the mercury in the fuse bore. For these data, one or two test operations produced the discrete changes in bore area shown.

It is logical that the thermal erosion of the channel would be a function of energy per unit area, but this did not appear to hold strictly true. The

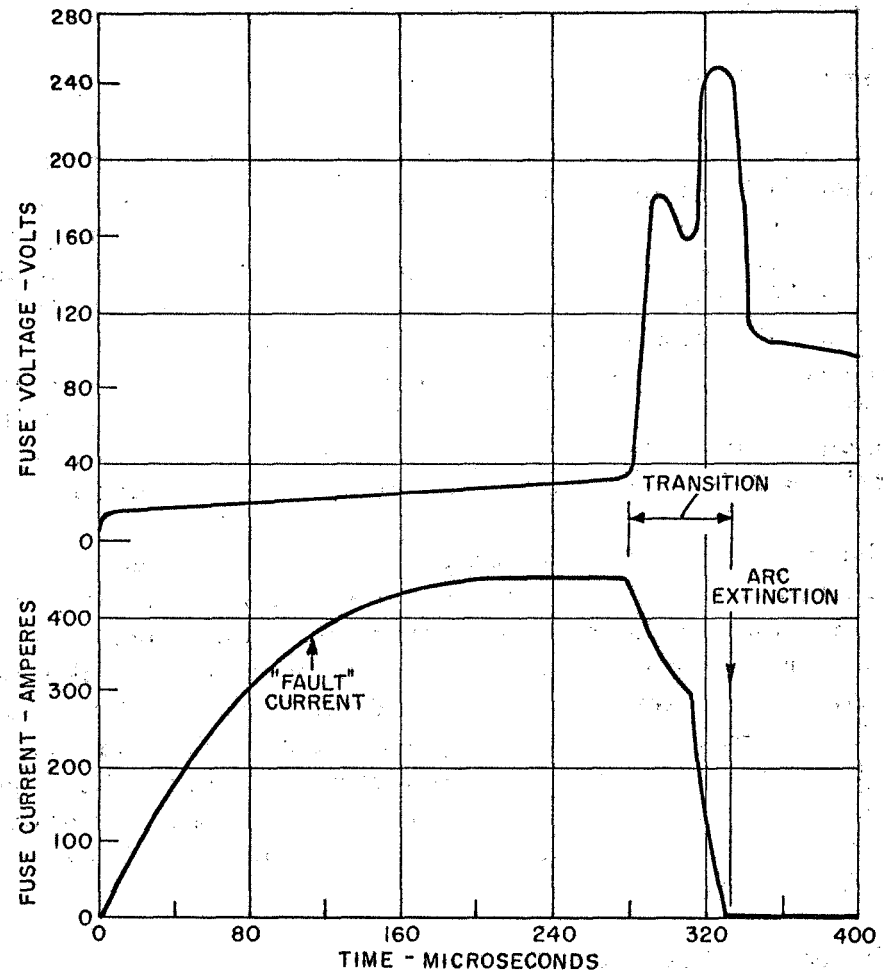


Figure 27 - Current and Voltage Waveforms for Fuse Operation with Rapid Arc Extinction

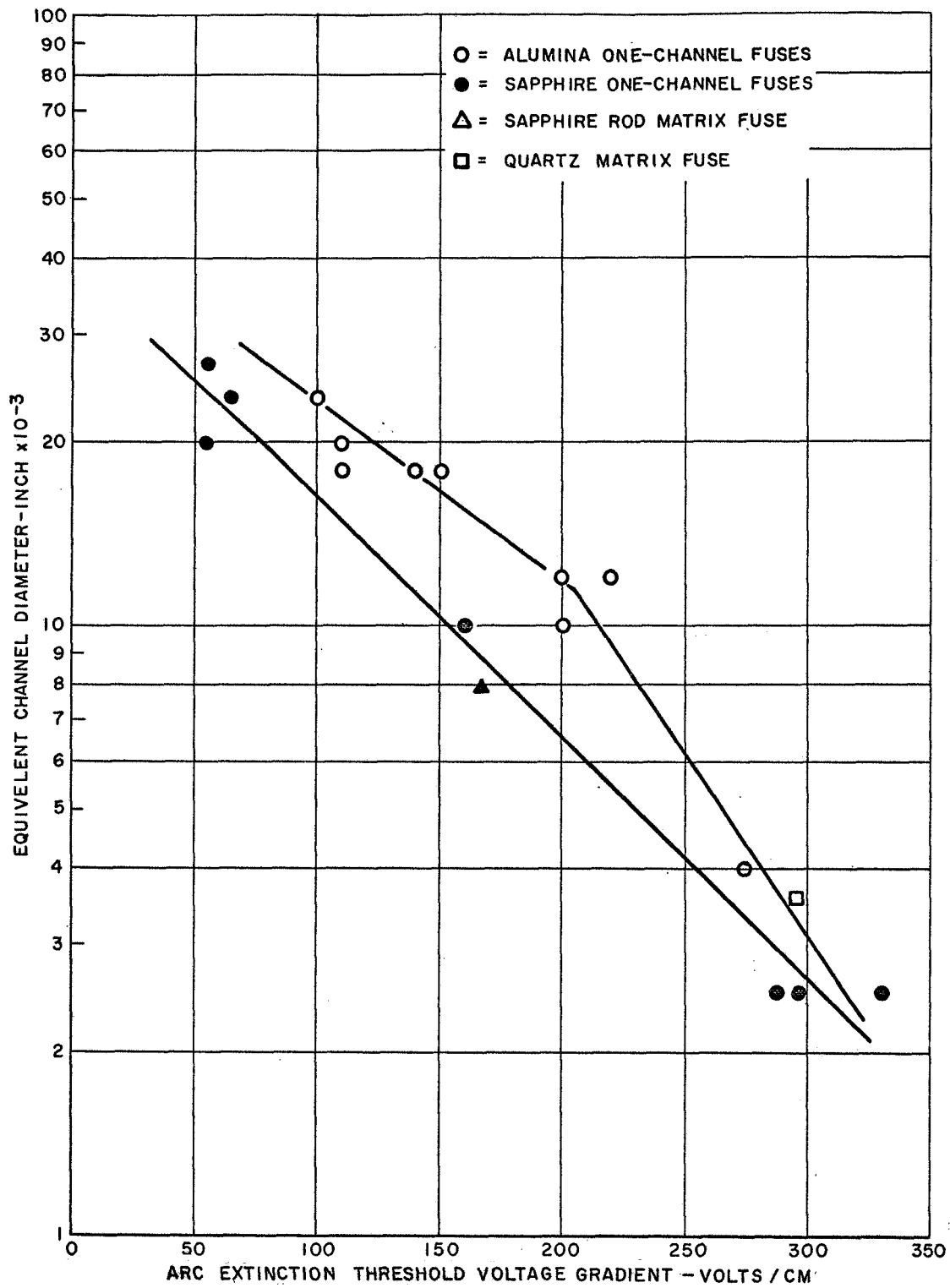


Figure 28 - Arc Extinction Threshold Voltage Variation with Channel Diameter

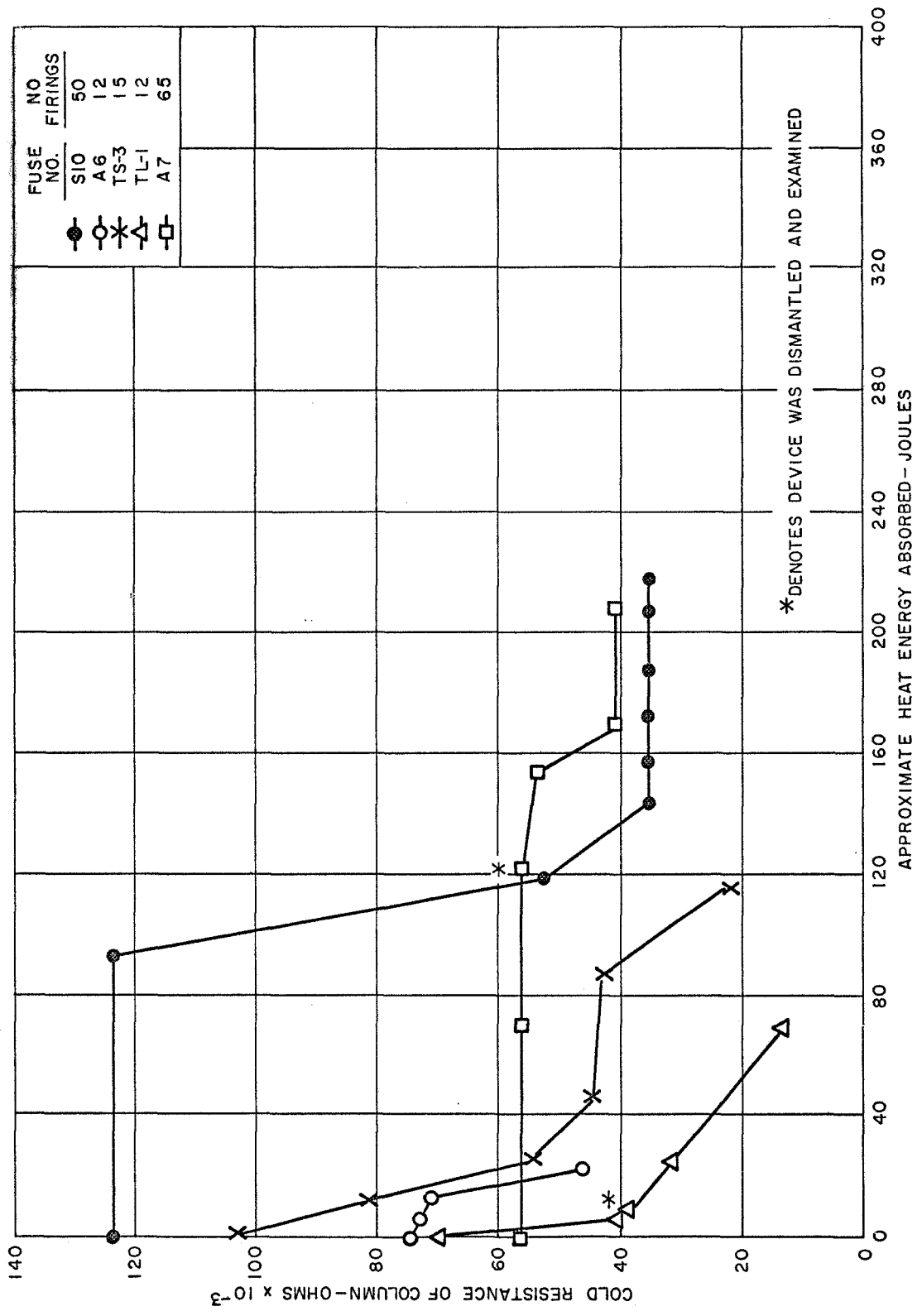


Figure 29 - Changes in Resistance with Fuse Operation II

"flat" channel devices -- ie. those having the very narrow rectangular channel cross-section of Figure 8 -- eroded with a lower energy density than the devices having cylindrical channels, by a factor of about 2 to 1. This is probably due to uneven distribution of the arc energy in the channel. One or both of the following factors may contribute to the uneven distribution:

(1) The channel width varies somewhat and a higher plasma temperature is expected for wider channels, based on the analysis in Appendix A. The radiation-transfer mechanism dominates here and is a fourth-power function of temperature, meaning a slight increase in plasma temperature causes a much larger increase in energy dissipated at the walls.

(2) The channels have a ratio of width to thickness of 24 or more, so the arc conditions may vary widely due to evaporation of less refractory materials such as glass bonding material from the channel walls, leading to selective restriction of the arc, comparable to the effect described above.

Moreover, the two flat channel devices which eroded were found to be enlarged to a round or oval opening, as may be seen in Figure 30, when the fuses were dismantled and examined after test. This follows logically from factor (1) above, since the arc energy would become more concentrated as the channel eroded, ie. there should be a trend toward eroding out a comparatively small oval channel rather than a general eroding away of the whole channel.

The data from cylindrical bore devices thus are considered more representative of the ability of these materials to resist thermal erosion. The cylindrical sapphire begins to erode at 200 to 300 joules per cm^2 with an arc duration of the order of 10^{-2} second, while the alumina cylindrical-channel devices begin to erode at 100 to 200 joules per cm^2 for a 10^{-2} second arc duration. Since the aluminas soften at about 85 percent of the sapphire softening temperature (2000°K vs. 2350°K), and the fourth-power radiation factor is applicable, a difference in energy tolerance of $0.85^{-4} = 1.93$ would be expected, so the ratio of about 2 to 1 between sapphire and alumina is in order. (The one quartz device tested indicated much poorer energy tolerance.)

The early erosion behavior of fuses TS-3 and TL-1 depicted in Figure 29 represents excess glass bonding material being eroded from the channel. (The excess glass was visible by microscope examination before test.) Fuse TL-1 was dismantled and examined at the point noted and no bore erosion was detectable. Fuses TS-1 and TS-2, identical in structure to fuse TS-3 (see Table III) experienced very similar early erosion of excess glass from the channel. Fuses TS-1 and TS-2 were examined by

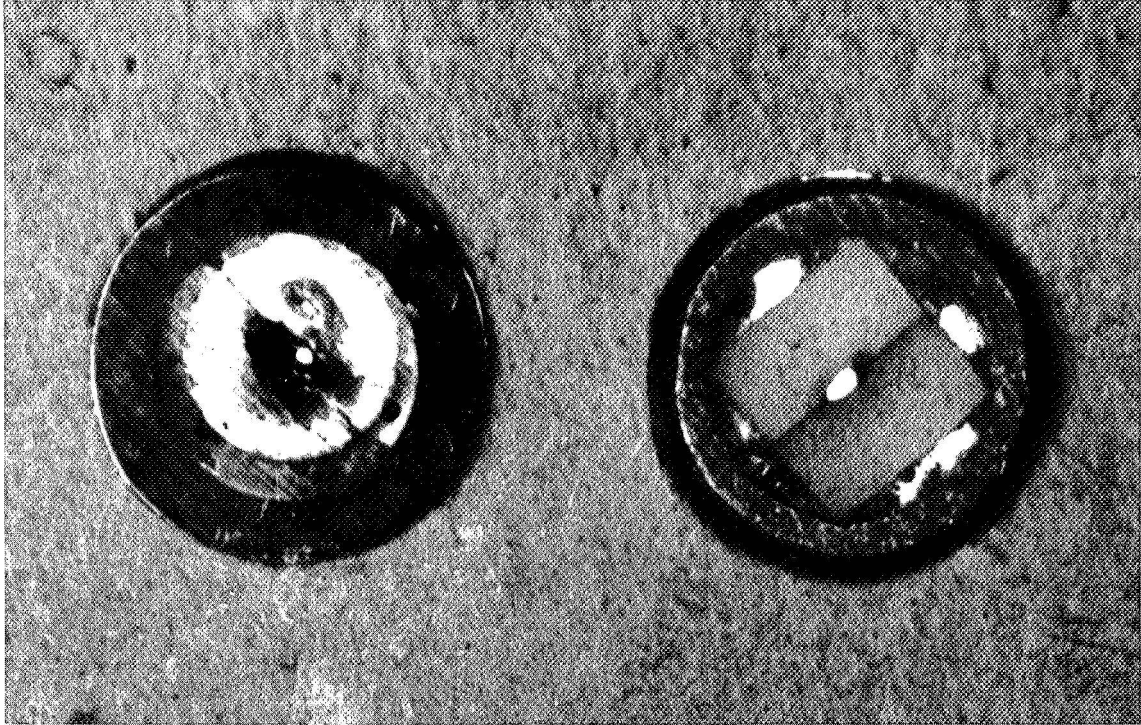


Figure 30 - Channel Structures of Fuses TS-3 (Left) and TL-1 After Test. (Fuse TS-3 has a hole approximately 0.015-inch in diameter at the center of its 0.0015 x 0.090 inch channel. Fuse TL-1 has an oval approximately 0.012 x 0.040 inch at the center of its 0.0025 x 0.065 inch channel.)

TABLE III - SUMMARY OF NARROW-CHANNEL DEVICES

<u>Fuse No.</u>	<u>Type of Design</u>	<u>Channel Material</u>	<u>Channel Min. Size x Length</u>	<u>No. Tests</u>	<u>Disposition</u>
F1	Fig. 11	Alumina (99%)	.003 x .180	13	Rod broken
R1	Fig. 11	Alumina (99%)	.002 x .140	12	Rod broken
R2	See text	Sapphire	.001 x .180	15	Rod broken
R3	Fig. 7	Sapphire	.005 x .210	15	(A)
TS-1	Fig. 8	Sapphire	.0015 x .180	55	Dismantled
TS-2	Fig. 8	Sapphire	.0015 x .150	70	(B)
TS-3	Fig. 8	Sapphire	.0015 x .150	15	Channel eroded
TL-1	Fig. 8	Alumina (99.8%)	.0025 x .150	12	Channel eroded
Q1	Fig. 10	Quartz	.001 x .200	80	Dismantled

Notes: (A) Center rod dislodged by last test

(B) External structure leaks mercury, could be rebuilt

- - - - -

microscope and no thermally induced erosion of the sapphire was found, because the arc tended strongly to extinguish in 10^{-3} second or less for these fuses. The cylindrical bore devices do not experience this early-erosion, of course, because there is no extraneous material in the channel.

Because of the factors described above, the cylindrical channel fuses furnished to NASA should enable the most representative data relative to bore erosion under long-term operating conditions. The objective of performing tests of 1000 or more operations should thus be performed using the 15 fuses furnished to NASA for use in such tests.

The characteristics of these fuses and the recommended maximum circuit voltage are shown in Table IV. The maximum voltage has been selected to limit the arc current to approximately half the fuse rated current, based on arc impedance.

Although the original objective had included 1000-operation tests for some of the fuses, the fuses were shipped to NASA instead for performance testing, at their request. The fuses furnished were fabricated of three materials, and in a variety of channel sizes (as shown in Table IV), to evaluate a range of fuse design parameters.

TABLE IV - OPERATING CHARACTERISTICS OF FUSES
SEND TO NASA

<u>Fuse No. *</u>	<u>Channel Dia. x Length</u>	<u>Approx. Arc Impedance Ohm</u>	<u>Max. Circuit Voltage</u>	<u>Notes</u>
A7	.020 x .450	7	90	(1)
A8	.020 x .300	6	75	
A9	.020 x .450	9	100	
L1, L2	.018 x .300	8	90	
L3	.018 x .450	12	100	
S4	.020 x .300	5	50	(2)
S5, S6, S7	.020 x .300	5	50	
S8, S9	.020 x .450	7	75	
S11	.009 x .220	28	75	(3)
S12	.020 x .450	7	75	
S13	.012 x .320	20	100	(4)

* All fuses are of the Fig. 4 design with fuse ratings of 15 amperes unless noted

Fuse channel materials are keyed by fuse number:

"A" denoted 99% alumina

"L" denotes 99.8+% alumina

"S" denotes sapphire

(1) Channel eroded to 0.024 inch diameter during tests; fuse rating is 20 amperes

(2) Badly damaged by test operation in unprotected circuit by NASA

(3) Fuse rating is 5 amperes

(4) Fuse rating is 7 amperes

MULTIPLE-CHANNEL DEVICES

In terms of arc extinction, arc impedance, and bore erosion, the behavior of the multiple-channel devices tested was substantially the same as that observed in the single-channel devices.

The performance of the six-channel devices fabricated from sapphire in the configuration of Figure 7 was as consistent as that of the 0.009 or 0.010 inch diameter cylindrical bore single-channel sapphire devices, and they were similar in arc-extinction voltage and arc impedance ratio, indicating that arcs were established in all six channels. There was also no tendency of fuse channels to reclose while the arc was passing current.

There was definite evidence of preferential erosion in tests of the devices shown in Figure 11, in that the outer alumina members eroded and sapphire inner members did not. This was not unexpected, based on the experience cited earlier for alumina and sapphire bore materials.

The only unusual behavior attributable to the multiple-channel configurations was experienced with fuse Q1, the 19-channel cross-section shown in Figure 10. In the majority of the fuse Q1 tests, the fuse would partly reclose for a few microseconds several times before the circuit SCR would turn off. This phenomenon is illustrated in Figure 31, where the SCR was bypassed and the circuit was opened by the protective circuit relay to enable better observation of the reclosing phenomenon. It is probable that the reclosing occurred in one, or a very few, of the fuse channels and thus the fuse would re-fire in a very short time.

Although, overall, the channels of fuse Q1 had enlarged 3 times in terms of cross-section after 90 test firings, microscopic examination after test showed visually that all 13 larger passages eroded about equally. No erosion of the six small passages could be detected. This again illustrates the advantage of narrower channels as well as the general tendency to divide current and energy evenly among parallel passages.

It is interesting to note that the three "flat" channel sapphire devices, made in the Figure 8 configuration, also indicated a slight tendency toward reclosing and re-firing. The very wide but thin cross-section (0.0015 inch by 0.090 inch) is believed to foster this behavior. Perhaps the liquid mercury is not always completely ejected from the channel, or the arc may be quenched by the re-entering liquid mercury at the ends of the channel where the energy density is low, as indicated by the selective erosion of one of these devices (see "Thermally-Induced Bore Erosion").

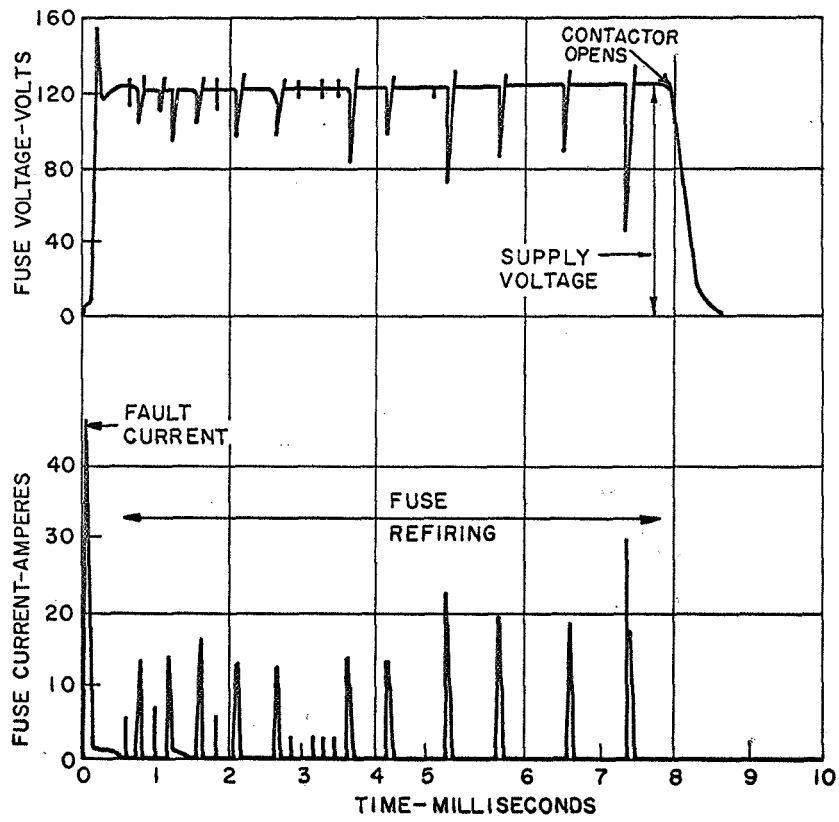


Figure 31 - Current and Voltage Waveforms for Fuse Q1 Showing Multiple Firing Action

DISCUSSION OF RESULTS

In discussing the results in this section, four major areas are treated in the order indicated: (1) factors in circuit protection, (2) arc behavior and thermal erosion, (3) fabrication and materials for the fuse channel, and (4) design parameters for the fuse channel.

FACTORS IN CIRCUIT PROTECTION

Circuit protection as provided by the fuses developed here is superior to conventional fuses in several respects. Faulted circuits being protected by these 15-ampere rated devices would experience response time and I^2t energy much lower than for 15-ampere-rated conventional fuses. Protection is comparable to 3 or 4 ampere-rated conventional fuses. The arc which develops in conventional fuses also often persists 10^{-2} second or longer at low impedance -- on the order of 1 ohm. Thus, the fault-induced energy allowed by a conventional fuse during the arc state is often comparable to the energy passed before the fuse "fires", while the self-healing fuse permits little arc-state energy. The requirements for switching a faulted circuit are also much more favorable for self-healing fuses, especially where the fuse operates in the arc-extinguishing mode in a solid-state circuit, such as for the test circuit used in this investigation. The fuse can fulfill a fault-clearing switch function by very quickly clearing short-term minor faults (such as occasional commutation failures in SCR-operated inverter circuits). A simple logic circuit function which delays operation of the circuit protective switch for about 10^{-4} second would allow the SCR to switch off without the protective switch being operated for minor faults. The protective switch would be required to switch comparatively little energy in any event, since the self-healing fuse passes little circuit energy even if the switch closed at peak fuse current, a few milliseconds after the initial fuse firing (refer to fuse operation shown in Figure 26). Thus the protective switch may have contacts of relatively low energy rating and be a light, fast-acting switch, compared to the large, heavy contacts required to open high fault currents where no fuse is used.

Where the self-healing fuse is used as a current limiter by taking advantage of the high-impedance arc, as might be advantageous in motor circuits, for example, the arc current would have to be limited to about half the fuse rated current to provide long fuse life. This requirement dictates an appreciable circuit loss for these devices, because impedance ratios

larger than 500 may be impractical, based on experiments reported herein. With 1/2 rated current as a limit, the 500 ratio results in 1/250th (or 0.4 percent) of the circuit power being continuously dissipated in the fuse during normal circuit operation.

Conventional fuses are superior in this respect, rarely dissipating over 1/1000 of the circuit power. However, specially designed one-time fuses which provide fast response and low energy limiting performance comparable to these self-healing types are more comparable in circuit dissipation.

ARC BEHAVIOR AND THERMAL EROSION

The erratic nature of the confined metal-vapor arc dealt with here makes specific design parameters difficult to derive, but trends and ranges of the arc parameters have been defined reasonably well.

The most critical parameter, the tendency of the arc to extinguish, was also the most erratic and elusive to accurately define. The most representative data are shown in Figure 28. The data points are average values obtained from fuses which were comparatively consistent in their arc extinction behavior as well as providing good performance as fuses. The fuses were cylindrical-bore single-channel devices, except for the equivalent diameter 0.004-inch alumina and 0.0025-inch sapphire devices. The latter devices were actually 0.0025 and 0.0015 inch "flat" channel fuses, respectively, and the equivalent diameter was derived by using a 1.25:1 geometry factor (refer to Appendix A). Two multiple-channel fuses are also separately plotted on Figure 28.

The striking but somewhat puzzling aspect of these data is the large difference between the extinction threshold voltages for alumina and sapphire fuses. For fuse channels 0.025 inch in diameter, the ratio is almost 2 to 1 in favor of alumina. This trend persists down to diameters of less than 0.010 inch. A similar trend was observed among other fuses which performed more erratically or were only given brief tests.

It is believed that ablation cooling of the arc due to material being vaporized off the less refractory alumina surface is probably responsible for the stronger tendency toward arc extinction. If this process is responsible for the better alumina performance, it would be related to the impurities in the alumina as compared to the impurity-free sapphire. It is surprising, then, that the ultra-pure alumina with about one fifth of the impurities of the 99 percent alumina performed much the same as the latter. It was also

noted that the 99-percent aluminas showed no appreciable tendency to change toward a lower arc extinction voltage as material was evaporated from the surface, a process that would tend to "refine" the melted alumina surface to a higher purity, thus leading to less ablation as testing continued. The ablation-cooling process, therefore, may not be the dominant factor in the arc extinction tendency of alumina devices, unless the alumina becomes porous enough to retain minute amounts of liquid mercury until after the transition explosion and the mercury then evaporates as the channel walls are heated, contributing to arc extinction.

For applications where rapid circuit switching (experienced when the fuse extinguishes and recloses) is undesirable, such as in high-inductance dc circuits or motor circuits, the current-limiting arc would be the more important factor. A fuse of this latter type would require the highest feasible impedance ratio, and sapphire should be used because of the high energy tolerance required. The only devices fulfilling these requirements, of those tested, are the flat channel sapphire fuses of 0.0015 inch or less channel thickness. Such fuse channels would be very short -- about 0.25 cm (0.10 inch) per 100 circuit volts -- and a separate parallel channel should be provided for each 5 amperes of fuse rating approximately, to overcome the concentration of arc energy (refer to "Thermally-Induced Bore Erosion").

FABRICATION AND MATERIALS FOR THE FUSE CHANNEL

Two principal areas of concern in fabrication of these fuses are (1) placing the precompression restraint around the alumina or sapphire channel material, and (2) techniques for fabricating the very narrow channels desirable in these devices.

The restraint problem can be well resolved by either of the designs shown previously in Figures 1 and 2, and described earlier in the text.

The glass-molded design has the advantage of being a smaller, lighter weight device and probably can be mass-produced at less cost since it is inherently a one-step fabrication process and requires less precision fitting of parts. The double-conical design could be improved in both these respects, by welding the two end caps (while under heavy force) rather than bolting the end caps together to apply the heavy restraint. The inner double-conical piece probably can be molded in glass also, eliminating the expensive, precise machining of the alumina or sapphire. (This was tried for one double-conical device with partial success, but the glass molding technique would need more refinement.)

Achieving a reliable channel structure in the case of very narrow channels is a more formidable problem for sapphire than for alumina, which can be extruded in multiple-channel forms with channel diameters as small as 0.008-inch and perhaps smaller.

Sapphire can be obtained in single 0.009-inch diameter channels, grown as single-crystal material. These pieces then are readily glass-molded into multiple-channel forms. The flat channel devices (refer to Figure 8) offer very narrow channels but are difficult to fabricate with channels free of the glass bonding material, in the case of either alumina or sapphire.

Either material can also be fabricated into the rod configuration shown in Figure 7, or similar rod configurations. Even though the extraneous glass problem was not as prevalent for the rod devices fabricated, the center rod must be well-bonded to resist being loosened by transition forces. In the Figure 7 configuration, filling two of the six open passages with glass bonding material should accomplish this.

Two classes of alumina were used for channel materials, high purity commercial alumina (99+ percent alumina) and a proprietary ultra-pure (99.8+ percent) alumina body prepared in General Electric's Microwave Tube Ceramic Laboratory. The ultra-pure alumina has advantages as a channel material in that it is about intermediate between commercial alumina and sapphire in refractoriness (softening temperature) and has exhibited arc extinction properties similar to the commercial alumina. Thus fuses designed for rapid arc extinction using ultra-pure alumina channels should be more reliable than commercial alumina types.

The sandwich devices offer the possibility of fabricating fuse channels of more erosion-resistant materials than the alumina or sapphire, but the fabrication problems are still formidable. The use of an outer structure similar to the double-conical structure of Figure 1 around a sandwich core of glass-bonded cermet or plasma-sprayed molybdenum (refer to the "Fuse Designs" section) is considered a good approach. This type of structure could provide both heavy axial and radial restraint for the sandwich core.

It is considered equally feasible to use other more refractory oxides for the bore material. Yttria, beryllia and thoria are candidates, but all would need to be of unusually high purity to be more refractory than sapphire. Ultra-pure yttria and thoria are available in limited forms at present and other refractories such as nitrides may become available. The more erosion-

resistant materials are not considered necessary unless fuses which operate in the high-impedance arc mode are to be fabricated, as was discussed previously.

At the other extreme of much less refractory materials is silicone rubber. Two sandwich devices utilizing rubber for insulating layers were tested and two factors were noted about their performance: (1) the arc would self-extinguish very rapidly, and (2) the erosion of the rubber after ten test firings was negligible although the surface was "charred" in appearance. These factors in combination suggest that a very small quantity of bore material (perhaps only a few atomic layers) vaporized from the surface would ablation-cool the arc and lead to rapid extinction. The cause for fuse failure was injection of liquid mercury into the thin rubber layers of the molybdenum sandwich (refer to "Fuse Design"), suggesting that a silicone rubber insulated sandwich device using thicker layers of rubber and with heavy restraint parallel to the fuse bore would operate reliably for up to fifty operations. Such a device could be less expensive to fabricate than the more refractory materials.

DESIGN PARAMETERS FOR FUSE CHANNELS

Because the arc extinction threshold voltage falls rapidly for larger bores, it becomes difficult to design fuse bore of more than 0.011 inch (equivalent diameter) of sapphire or 0.015 inch of alumina, when operation with arc extinction is to be assured. For very narrow channels, (refer to Figure 28) the channel size can be doubled with an attendant reduction of only 25 percent in extinction voltage. This affords considerable flexibility in design parameters, especially for the "flat" channel devices (shown in Figure 8); the cross-section of the fuse channel can be changed considerably without appreciably changing the wall area of these wide, thin-channel configurations, as discussed below. The use of channels about 0.010-inch diameter in high-purity alumina is also desirable because such material can be readily fabricated in multiple-channel forms. Suggested fuse channel designs of these types are shown in Figure 32.

It would be advantageous to make flat-channel devices with the wide channel divided into two or more channels, to overcome the concentration of arc energy and channel erosion described earlier under "Thermally Induced Bore Erosion". Because of the erratic nature of the arcs occurring in these fuses, there is a small probability that the arcs may persist several milliseconds for any fuse design, and this consideration makes the

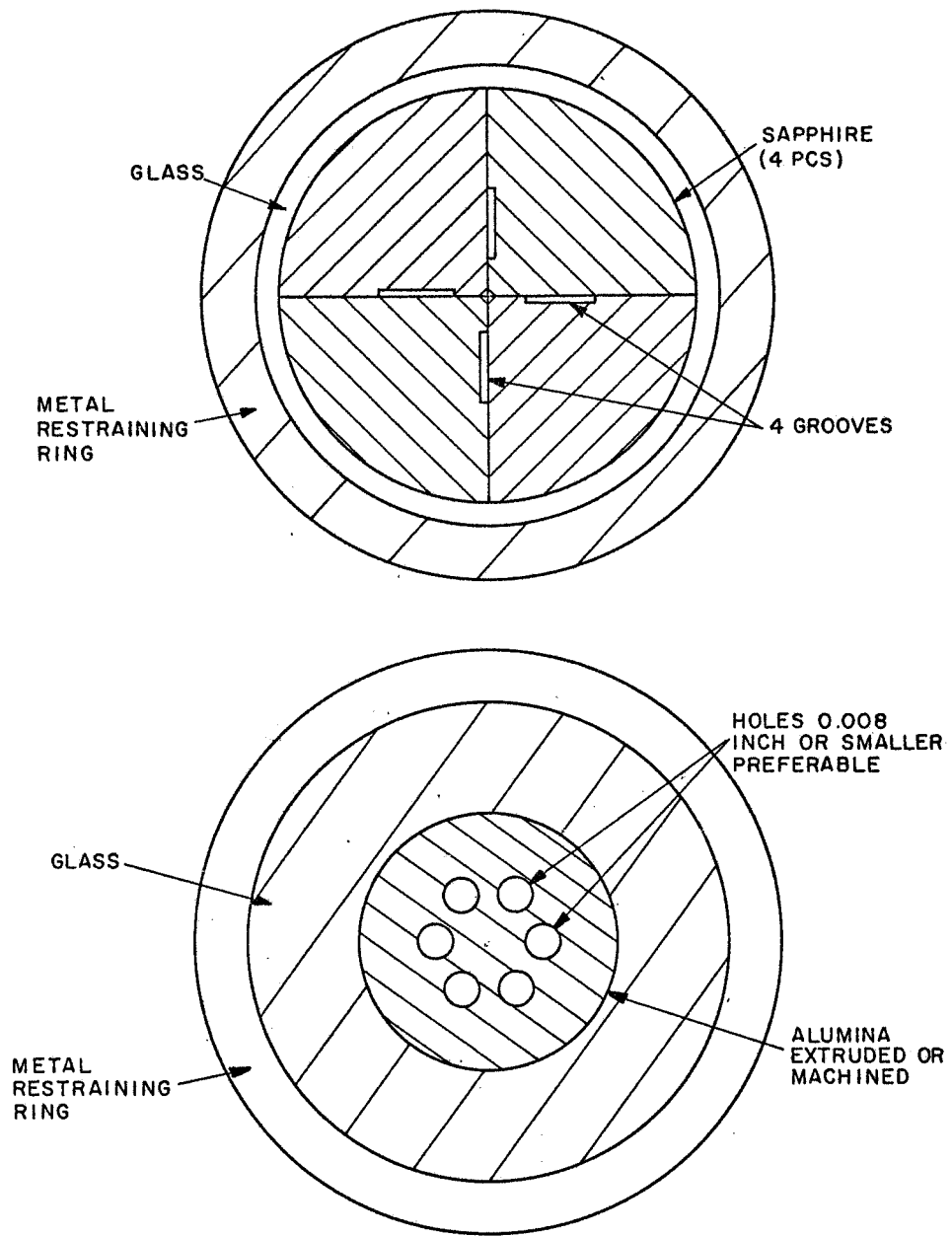


Figure 32 - Suggested Design Improvements for Fuse Channels

higher arc impedance desirable, more so for the alumina devices than sapphire, which is more refractory. Therefore, the arc impedance data shown in Figure 24 indicate that devices of less than 0.008 inch (equivalent diameter) would be more reliable in the presence of an occasional arc of substantial duration.

Some straightforward calculations will aid in designing fuse channels with respect to the I^2t protection a fuse will provide, and in calculating the fuse current rating for long-term operation. These calculations are based on the energy mechanisms which determine long-term and short-term operation. The specific heat capacity of the mercury in the fuse channel determines characteristics for times less than 10^{-3} second, while heat conduction from the mercury to the walls of the fuse channel is the dominant mechanism for times longer than 10^{-1} second.

A simple expression for the short-term I^2t energy due to specific heat is derived in Appendix C. This relationship has been found to hold reasonably well for the fuses tested during this program, for short fuse firing times. The heat conduction characteristics, measurements, and calculations used in estimating fuse current ratings for long-term operation are also included in Appendix C. The calculations are also useful in designing fuses of various ratings, based on the resistance calculated from the channel geometry for obtaining the I^2R wattage of the channel, and the relationship $I^2R = 360 a_w$, where a_w is the fuse channel wall area in cm^2 .

The ability of a given fuse channel to resist thermally induced erosion is directly related to the area of the channel wall, assuming the arc energy to be evenly distributed over the wall area. Thus it is desirable to design a fuse channel for maximum wall area, while the fuse current rating limits the wall area, as described above.

For a single cylindrical channel the only design adjustment available is to design for maximum allowable R . For non-cylindrical configurations of single channels, the geometry can be adjusted to provide larger wall areas for a given R , but the gains are limited due to the uneven energy distribution, as discussed above.

There is an additional flexibility in design afforded by the multiple-channel configurations, in that part of the wall area of some fuse channels does not contribute to the long-term thermal balance because no net heat is conducted through the channel walls. For example, the 7-rod design of Figure 7 would conduct little heat from the fuse channels into the center

of the structure for the long fuse channels in these devices. Thus, the Figure 7 configuration is considered to utilize only 2/3 of the actual channel wall area in selecting a value of a_w to calculate a fuse current rating. Experimental data confirm that this assumption is reasonable.

Similarly, the configuration shown in Figure 10 would use an effective wall area a_w equal to the cylinder formed by the inside diameter of the outer tubing. Channels formed by a close-spaced ring of holes as shown in Figure 32 would have a representative a_w approximated by a cylinder passing through the hole centers. Since the high purity aluminas can be readily extruded or machined in such forms, this design becomes very attractive for future fuse designs.

CONCLUSIONS

Extensive self-healing fuse tests performed which simulated the protection of a faulted SCR circuit show these fuses to be superior to conventional fuses in protecting solid state devices, in that better energy-limiting action and faster switching action are obtained. Test data obtained show consistent performance, in terms of the energy-limiting action, for several fuse configurations and materials. The available data can be projected to design fuses which will protect a range of solid state devices.

It has been found that containment requirements imposed by the explosive transition state of fuse operation can be fulfilled by either of two design configurations. Fuses of one of these configurations were furnished to NASA for further tests.

The durability of the fuses tested was most critically related to the tendency of the arc to quickly extinguish. With the smaller fuse channel this tendency improved. Because of this factor, sapphire fuses with a diameter of less than 0.011 inch or alumina fuses less than 0.015 inch provided better durability, and even smaller sizes are expected to show greater improvement.

Very high arc impedance was obtained for channels less than 0.002 inch across and these devices can provide longer-term operation as non-switching current limiters. Sapphire was found capable of withstanding twice the heat flux tolerated by alumina for such devices.

A simple bellows, mechanically restrained to resist impact forces, adequately provides the elastic characteristics required of the fuse container. A new seal-off technique utilizing silicone rubber was developed for use in these devices.

Appendix A

AN ANALYSIS OF HIGH-PRESSURE METAL VAPOR ARCS IN NARROW CHANNELS

INTRODUCTION

This appendix describes calculations performed for the voltage-current-temperature characteristics of high pressure metal vapor arc in narrow channels. Several power dissipation mechanisms are considered here: atomic thermal conduction, electronic thermal conduction, ionic diffusion and recombination, and thermal radiation. All of these are shown to be significant in mercury vapor arcs, at thicknesses below a millimeter, operated near the minima of the volt-ampere characteristics. A procedure is also developed for combining calculations for arcs in which a single dissipation mechanism dominates into characteristics that can be compared with experimental data on arcs in which several dissipation mechanism are important.

Although we tend to associate negative incremental resistances with high-pressure arc columns, experience has shown that this association is valid only for a limited range of operating conditions. Any given arc device usually exhibits a falling volt-ampere characteristic (negative incremental resistance) at low currents, but a positive incremental resistance for sufficiently high currents. The physics of this transition from negative to positive resistance often is not clear, and may differ among different devices, but it can be described by the following simple analysis.

The power input P to unit length of a steady, axially uniform arc column subject to electric field E and carrying current I is

$$P = EI$$

The conductance G of unit length of that arc column is

$$G = \frac{I}{E}$$

Then

$$E^2 = P/G,$$

$$I^2 = PG$$

and

$$\frac{dE}{dI} = \frac{1}{G} \left[\frac{1 - \frac{d(\ell n G)}{d(\ell n P)}}{1 + \frac{d(\ell n G)}{d(\ell n P)}} \right] \quad (1)$$

Equation (1) shows that the sign of (dE/dI) , the incremental resistance of unit length of arc column, is determined by whether or not $d(\ell n G)/d(\ell n P)$ exceeds unity, i. e., by whether or not the column conductance increases relatively faster or slower than the power input to the column. Thus the factors determining the column resistivity are those affecting the number, distribution, and mobility of charge carriers, and the dissipation mechanisms transferring the electrical energy input to the walls surrounding the arc column. It should be noted that the differentials in Equation (1) are total differentials that include the effects of changes in temperature and current density distributions.

The high pressure arc columns encountered in specific devices may be any of several types having the common feature that the power dissipated in the discharge is largely thermalized in the column, then delivered to the surrounding walls by either thermal conduction or radiation. (Convective heat transport is a negligible factor in the relatively long thin channels of principal interest here.) The characteristics of these discharge types are determined largely by whether:

(a) the electron mobility in the channel is governed by electron-atom ("slightly-ionized plasma") or electron-ion ("fully-ionized plasma") interactions;

(b) the transmission of power to the channel walls is accomplished mainly by atomic thermal conduction, electronic thermal conduction, or radiation.

Not all possible combinations of these factors have interest, but the following modes seem likely to occur in physical situations:

- (2) slightly-ionized plasma, atomic-conduction cooling,
- (3) slightly-ionized plasma, electronic-conduction cooling,
- (4) slightly-ionized plasma, ion diffusion cooling,
- (5) fully-ionized plasma, electronic-conduction cooling,
- (6) slightly ionized or fully-ionized plasma, radiation cooling.

Mode 2 and mode 6 at low currents give negative resistances. The other modes yield positive incremental resistances.

SLIGHTLY-IONIZED, ATOMIC-CONDUCTION COOLED DISCHARGE (Mode 2)

For simplicity in describing this mode, the assumption is made that momentum transfer in electron collisions with the walls of the discharge channel can be neglected. In addition, it is assumed that the energies of the electrons and atoms in the channel can be described in terms of a single temperature function T , and that the fractional ionization is small and corresponds to local thermal equilibrium at that temperature. These assumptions give

$$\sigma = \frac{e^2}{m} \left(\frac{n_e}{n_a} \right) \left(\frac{n_a}{\nu_{ea}} \right) \quad (2)$$

and a temperature dependence of electrical conductivity that is approximately

$$\sigma \sim \epsilon - \frac{eU}{2kT} \quad (3)$$

corresponding to the principal temperature dependence of the fractional ionization. Here σ is the electrical conductivity, e and m the electron charge and mass, k the Boltzmann constant, U the lowest ionization potential of the vapor, n_e and n_a the electron and atom densities, and ν_{ea} the frequency for electron momentum transfer to the neutral atoms. The expression for the thermal conductivity K_a of the neutral vapor is taken from kinetic theory¹:

$$K_a = \frac{k}{2} \frac{\langle v_a \rangle}{A_{aa}}, \quad (4)$$

where A_{aa} is the appropriate cross section for atom-atom collisions (about 30 \AA^2 for mercury) and $\langle v_a \rangle$ is the average thermal speed of the neutral atoms. The thermal conductivity then varies as the square root of the temperature,

$$\frac{d(\ln K_a)}{d(\ln T)} = 1/2 \quad (5)$$

The transport of heat in the channel is described by the usual energy balance

$$-\nabla \cdot (K_a \nabla T) = \sigma E^2, \quad (6)$$

which also may be written as

$$\nabla^2 T + \frac{d(\ln K_a)}{d(\ln T)} \frac{(\nabla T)^2}{T} = - \frac{\sigma E^2}{K_a} \quad (7)$$

For the flat-channel geometry shown in Figure 33, Equation (7) becomes

$$T \frac{d^2 T}{dx^2} + \frac{d(\ln K_a)}{d(\ln T)} \left(\frac{dT}{dx} \right)^2 = - \frac{T \sigma E^2}{K_a} \quad (8)$$

or equivalently

$$\frac{T}{2} \frac{d}{dT} \left[\left(\frac{dT}{dx} \right)^2 \right] + \frac{d(\ln K_a)}{d(\ln T)} \left(\frac{dT}{dx} \right)^2 = - \frac{T \sigma E^2}{K_a} \quad (9)$$

Equations (9) and (5) have the first integral

$$\left(\frac{dT}{dx} \right)^2 = - \frac{1}{T} \int_{T_0}^T \frac{2T \sigma E^2}{K_a} dT \quad (10)$$

if $T = T_0$ at channel center ($x = 0$) where $(dT/dx) = 0$. To permit an approximate solution of Equation (10), only the exponential temperature variation of the integrand caused by ionization changes is considered,

$$\begin{aligned} \left(\frac{dT}{dx} \right)^2 &\approx - \frac{2T_0 \sigma_0 E^2}{TK_{a0}} \int_{T_0}^T \frac{\sigma}{\sigma_0} dT \\ \left(\frac{dT}{dx} \right)^2 &\approx - \frac{2T_0 \sigma_0 E^2}{TK_{a0}} \epsilon^{\frac{eU}{2kT_0}} \int_{T_0}^T \epsilon^{-\frac{eU}{2kT}} dT \quad (11) \\ \left(\frac{dT}{dx} \right)^2 &\approx \frac{eUT_0 \sigma_0 E^2}{kTK_{a0}} \epsilon^{\frac{eU}{2kT_0}} \int_{\frac{eU}{2kT_0}}^{\frac{eU}{2kT}} \frac{\epsilon^{-u}}{u^2} du \end{aligned}$$

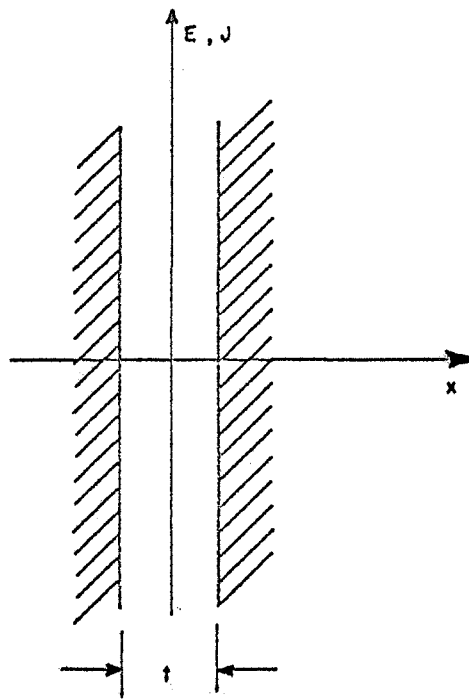


Figure 33 - Geometry for Flat-Channel Discharge

Because the values of eU/kT_o of interest here are quite large, 20 to 50, for values of T not too close to T_o and the slow variation of the $1/u^2$ term can be neglected and the intergral is approximately

$$\int_{\frac{eU}{2kT_o}}^{\frac{eU}{2kT}} \frac{\epsilon^{-u}}{u^2} du \approx \left(\frac{2kT_o}{eU} \right)^2 \epsilon^{-\frac{eU}{2kT_o}}$$

Then

$$\left(\frac{dT}{dx} \right)^2 \approx \frac{4k}{eU} \frac{T_o^3 \sigma_o E^2}{TK_{ao}} \quad (12)$$

The solution to Equation (12) giving $T = T_w$ at $x = x_w$ is

$$\frac{T^{3/2} - T_w^{3/2}}{T_o^{3/2}} = \left[\frac{9k\sigma_o E^2 (x_w - x)^2}{K_{ao} eU} \right]^{1/2} \quad (13)$$

In particular, since $x_w = t/2$, (where t is the channel width) and $T = T_o$ at $x = 0$, Equation (13) gives

$$\frac{(\sigma_o / K_{ao})}{\left[1 - (T_w / T_o)^{3/2} \right]^2} = \frac{4eU}{9kE^2 t^2} \quad (14)$$

The left side of this equation depends only on T_o for given T_w and metal vapor pressure. It increases strongly as T_o increases, for practical values of T_w and T_o , because of the strong temperature dependence of σ_o . The right side depends only on E and t . Thus Equation (14) determines the central arc temperature T_o as a function of the experimental parameters, and shows that T_o tends to decrease slowly as E increases.

The power P_w delivered to unit area of the wall may be estimated from

$$P_w = \int_0^{x_w} \sigma E^2 dx = \sigma_o E^2 \int_{T_o}^{T_w} \left(\frac{\sigma}{\sigma_o} \right) \left(\frac{dx}{dT} \right) dT, \quad (15)$$

which becomes, with use of Equations (3) and (12)

$$P_w = \sigma_o E^2 \left(\frac{eUK_{ao}}{4kT_o^3 \sigma_o E^2} \right)^{1/2} \epsilon^{\frac{eU}{2kT_o}} \int_{T_o}^{T_w} \sqrt{T} \epsilon^{-\frac{eU}{2kT}} dT$$

Again, provided that T_w differs from T_o by at least 10 or 20 percent, the integral can be approximated to give

$$P_w = \sigma_o E^2 \left(\frac{eUK_{ao}}{4k\sigma_o E^2} \right)^{1/2} \left(\frac{2kT_o}{eU} \right)$$

or, with use of Equation (14)

$$P_w = \frac{2}{3} \frac{K_{ao} T_o}{t} \left[1 - \left(\frac{T_w}{T_o} \right)^{3/2} \right] \quad (16)$$

The average current density in the discharge $\langle J \rangle$ is then

$$\langle J \rangle = \frac{2}{t} \frac{P_w}{E} = \frac{4K_{ao} T_o}{3Et^2} \left[1 - \left(\frac{T_w}{T_o} \right)^{3/2} \right] \quad (17)$$

Because T_o decreases somewhat as E increases, the average current density $\langle J \rangle$ also decreases as E increases, somewhat more rapidly than $(1/E)$. This is a negative resistance arc with properties similar to those of atmospheric-pressure arc columns.² Substitution of Equation (14) in Equation (17) to eliminate K_{ao} yields the form

$$\langle J \rangle = \sigma_o E \frac{(3kT_o/eU)}{\left[1 - (T_w/T_o)^{3/2} \right]} \quad (18)$$

which shows that the average current density is, for reasonable values of T_o and T_w , considerably below its value at the center of the discharge. Thus this is a heavily contracted discharge.

The negative resistance characteristic of this type of arc column is related easily to the introductory analysis given in the "Introduction" of this Appendix. For values of T_w that are sufficiently small, Equations (18) and (3) give

$$G \sim T_o \epsilon^{-\frac{eU}{2kT_o}}$$

while Equations (16) and (5) give

$$P \sim T_o^{3/2}$$

when the channel geometry is fixed. Then

$$\frac{d(\ell n G)}{d(\ell n P)} = \frac{2}{3} \left(\frac{eU}{kT_o} + 1 \right) \gg 1$$

and a strongly negative incremental resistance is assured.

SLIGHTLY-IONIZED, ELECTRONIC-CONDUCTION COOLED DISCHARGE (Mode 3)

If the electron density in the discharge becomes sufficiently large, the electrons can take over the thermal conduction function from the neutral atoms. In analyzing this possibility, the assumption is made that the populations of the various electronic states are distributed according to single electron temperature T . This temperature, however, need no longer equal the neutral-atom temperature.

Equations (2) and (3) still hold, and so do Equation (6) through (9) if K_a is replaced by the electronic thermal conductivity K_e . The Wiedemann-Franz law gives a convenient relation between σ and K_e ,

$$K_e = 3 \left(\frac{k}{e} \right)^2 T \sigma \quad (19)$$

which replaces Equation (4). The derivative of the thermal conductivity is now

$$\frac{d(\ell nK_e)}{d(\ell nT)} = 1 + \frac{d(\ell n\sigma)}{d(\ell nT)} = 1 + \frac{eU}{2kT} \quad (20)$$

Substitution of Equations (19) and (20) in Equation (9) gives

$$\frac{d}{dT} \left[\left(\frac{dT}{dx} \right)^2 \right] + \frac{2}{T} \left(1 + \frac{eU}{2kT} \right) \left(\frac{dT}{dx} \right)^2 = - \frac{2}{3} \left(\frac{eE}{k} \right)^2 \frac{1}{T} \quad (21)$$

which has the first integral

$$\left(\frac{dT}{dx} \right)^2 = \frac{2}{3} \left(\frac{eE}{k} \right)^2 \frac{\epsilon \frac{eU}{kT}}{T^2} \int_T^{T_0} T \epsilon^{-\frac{eU}{kT}} dT \quad (22)$$

giving $(dT/dx) = 0$, $T = T_0$, at $x = 0$. An approximate integration gives

$$\left(\frac{dT}{dx} \right)^2 \approx \frac{2}{3} \left(\frac{eE}{k} \right)^2 \left(\frac{kT_0}{eU} \right) \left(\frac{T_0}{T} \right)^2 \left[\epsilon^{\frac{eU}{k} \left(\frac{1}{T} - \frac{1}{T_0} \right)} - 1 \right] \quad (23)$$

This equation gives a temperature profile that is quite uniform over the central half of the channel, and plunges sharply to wall temperature in the outer quarters. The integration of Equation (23) can be accomplished in approximate fashion by dividing the channel in two parts. Let x_s be the coordinate at which $eU/k (1/T - 1/T_0) = 1$. Then for $x \leq x_s$, $T \cong T_0$, and the exponential term can be approximated by the first two terms in its series expansion to give

$$\frac{dT}{dx} \approx - \frac{eE}{k} \sqrt{\frac{2}{3}} \left(\frac{T_0 - T}{T_0} \right)^{1/2}, \quad x < x_s \quad (24)$$

which has the solution

$$\frac{T_0 - T}{T_0} \cong \frac{kT_0}{eU} \left(\frac{x}{x_s} \right)^2, \quad x < x_s \quad (25)$$

where

$$x_s = \frac{kT_o}{eE} \left(6 \frac{kT_o}{eU} \right)^{1/2} \quad (26)$$

For $x > x_s$, the exponential term in the brackets of Equation (23) is large and

$$\frac{dT}{dx} \simeq - \frac{eE}{k} \sqrt{\frac{2kT_o}{3eU}} \left(\frac{T_o}{T} \right) \epsilon^{\frac{eU}{2k} \left[\frac{1}{T} - \frac{1}{T_o} \right]}, \quad x > x_s \quad (27)$$

The solution to this equation matching the solution at $x = x_s$ is

$$\frac{eE(x - x_s)}{k} \sqrt{\frac{2kT_o}{3eU}} = \frac{1}{T_o} \left(\frac{eU}{2k} \right)^2 \int_{u_o + 1/2}^u \frac{\epsilon^{-(u - u_o)}}{u^3} du, \quad x > x_s \quad (28)$$

where $u = (eU/2kT)$. For the large values of u_o and the even larger values of u of interest here, x varies little with temperature. The wall coordinate x_w therefore may be taken as the value of x for which $T \rightarrow 0$, $u \rightarrow \infty$.

Then

$$(x_w - x_s) = \frac{1}{\sqrt{\epsilon}} \frac{kT_o}{eE} \frac{\sqrt{6kT_o/eU}}{\left[1 + (kT_o/eU) \right]^3} \quad (29)$$

and, with Equation (26) and the assumption $kT_o/eU \ll 1$,

$$\frac{eEt}{2kT_o} \simeq \left(1 + \frac{1}{\sqrt{\epsilon}} \right) \sqrt{\frac{6kT_o}{eU}} \quad (30)$$

This relation determines the central temperature T_o , and shows that for this discharge mode the temperature increases with electric field.

The power delivered to the wall may be estimated by dividing the integral of Equation (15) into two parts, for $0 < x < x_s$ and $x_s < x < x_w$, and substituting for dx/dT from Equations (24) and (27). The contribution from $0 < x < x_s$ is

$$\frac{\sigma_o E^2}{\frac{eE}{kT_o} \left[\frac{2}{3} \left(1 + \frac{kT_o}{eU} \right) \right]^{1/2}} \int_{T_o}^{T_s} \frac{1 - \frac{eU}{2kT_o} \left[1 - (T/T_o) \right]}{-\sqrt{1 - (T/T_o)}} d\left(\frac{T}{T_o}\right) \approx \frac{5}{6} \sigma_o E^2 x_s$$

and that from $x_s < x < x_w$ is

$$\frac{\sigma_o E^2}{\frac{eE}{k} \sqrt{\frac{2kT_o}{3eU}}} \int_{T_s}^{T_w} -\epsilon \frac{-\frac{eU}{k} \left(\frac{1}{T} - \frac{1}{T_o} \right)}{dT} \approx \frac{\sigma_o E^2}{\sqrt{4\epsilon}} (x_w - x_s)$$

In these evaluations, free use has been made of the assumptions $(T_o/T_s) \approx 1$ and $(eU/kT_o) \gg 1$. Thus the power to the wall is given by

$$P_w \approx \frac{\sqrt{\epsilon}}{\sqrt{\epsilon+1}} \left[\frac{5}{6} + \frac{1}{2\epsilon} \right] \sigma_o E^2 x_w \approx 0.63 \sigma_o E^2 x_w \quad (31)$$

The average current density is about 63 percent of its peak value, and the discharge is relatively uniform across the channel. Since σ_o increases with T_o , and T_o increases with E , the electrical characteristic for this mode exhibits positive incremental resistance.

In the terms of the introductory analysis, the conductance varies as

$$G \sim \sigma_o \sim \epsilon^{-\frac{eU}{2kT_o}}$$

while Equations (31) and (30) give

$$P = \frac{P_w}{x_w} \sim G E^2 \sim G T_o^3$$

when the geometry is fixed. Then

$$\frac{d(\ln G)}{d(\ln P)} = \frac{1}{1 + (6kT_o/eU)} < 1$$

and a slightly positive incremental resistance prevails.

SLIGHTLY-IONIZED, ION DIFFUSION COOLED DISCHARGE (Mode 4)

As the electron density in the discharge increases, the ion density increases in equal amount, and neutralization of ions at the wall of the discharge can provide a significant energy loss. In estimating these losses each ion may be considered to carry a potential energy eU equal to the ionization energy. Then with the density Γ_i of ion particle diffusion, there is associated a flow of energy $eU\Gamma_i$. If this flow provides the dominant energy loss, the energy balance for the arc gives

$$\nabla \cdot (eU\Gamma_i) = \sigma E^2 \quad (32)$$

The ion flux density Γ_i is given by

$$\Gamma_i = -D_a \nabla n_i \quad (33)$$

where D_a is the ambipolar diffusion coefficient

$$D_a = \mu_{ia} \frac{k}{e} (T_i + T_e) \quad (34)$$

and μ_{ia} is the mobility of ions determined by ion-atom collisions. It is assumed in the following that electronic and ionic temperatures are equal.

$$T_i = T_e \triangleq T \quad (35)$$

Then since the electrical conductivity σ given by Equation (2) also can be expressed as

$$\sigma = n_e e \mu_{ea} = n_i e \mu_{ea} \quad (36)$$

Equation (32) can be written

$$\frac{d^2 n_i}{dx^2} + \left[\frac{\mu_{ea}}{\mu_{ia}} \frac{eE^2}{2UkT} \right] n_i = 0 \quad (37)$$

for plane-parallel geometry. The temperature has been taken as a constant in Equation (37) because it usually varies much less rapidly than the ion density in these discharges.

The solution to Equation (37) giving a maximum ion density at channel center and $n_i \rightarrow 0$ at the wall is

$$n_i = n_{i0} \cos (\pi x/t) \quad (38)$$

with

$$\frac{kT}{e} = \frac{\mu_{ea}}{\mu_{ia}} \frac{E^2 t^2}{2\pi^2 U} \quad (39)$$

The ion density n_{i0} at channel center is not determined by this analysis. Since the diffusive loss from the central region is small, n_{i0} can be calculated from conditions for thermal equilibrium and charge neutrality at channel center.

From Equation (38) the average ion density in the channel is $(2/\pi) n_{i0}$. The average conductivity is similarly related to that at channel center σ_o , and the average current density is

$$\langle J \rangle = \frac{2}{\pi} \sigma_o E \quad (40)$$

The conductance derivative for this situation is

$$\frac{d(\ln G)}{d(\ln P)} \approx \frac{1}{1 + (2kT_o/eU)} < 1$$

so that the incremental resistance is slightly positive but less than that for mode 3.

FULLY-IONIZED, ELECTRONIC-CONDUCTION COOLED DISCHARGE (Mode

If the electron and ion densities in the discharge become sufficiently large, electron collisions with ions become the dominant factor limiting the electron mobility, and the fourth discharge mode appears. In this situation, Equation (2) for the electrical conductivity is replaced by

$$\sigma = \frac{e^2}{m} \left(\frac{n_e}{n_i} \right) \left(\frac{n_i}{\nu_{ei}} \right) \quad (41)$$

where n_i is the ion density. For discharge temperatures up to a few volts, the ions are predominantly singly charged. For channels much wider than a plasma Debye length, which is the usual situation for this mode, the plasma is electrically neutral almost everywhere and

$$\frac{n_e}{n_i} \approx 1$$

The electrical conductivity then varies as

$$\sigma \sim \frac{n_i}{\nu_{ei}} \sim T^{3/2} \quad (42)$$

The proportionality constant here is a function of the physical properties of electrons, and can be obtained from Spitzer's analysis.³

The Wiedemann-Franz law, Equation (19) is useful here also, and shows with Equation (42) that

$$K_e \sim T^{5/2}$$

and

$$\frac{d(\ln K_e)}{d(\ln T)} = \frac{5}{2} \quad (43)$$

Substitution of Equation (19) and (43) in the energy balance Equation (9) (with K_a replaced by K_e) gives

$$T \frac{d}{dT} \left[\left(\frac{dT}{dx} \right)^2 \right] + 5 \left(\frac{dT}{dx} \right)^2 = - \frac{2}{3} \left(\frac{eE}{k} \right)^2 \quad (44)$$

The first integral of Equation (35) giving $(dT/dx) = 0$ at $x = 0$, $T = T_0$ is

$$\left(\frac{dT}{dx} \right)^2 = \frac{2}{15} \left(\frac{eE}{k} \right)^2 \left[\left(\frac{T}{T_0} \right)^5 - 1 \right] \quad (45)$$

The temperature distribution then should be obtained by integration of

$$- \int_{T_0}^T \frac{dT}{\left[\left(\frac{T_0}{T} \right)^5 - 1 \right]^{1/2}} = \sqrt{\frac{2}{15}} \left(\frac{eE}{k} \right) x \quad (46)$$

Again it is necessary to do the integration approximately by dividing the interval into two parts. Let x_s be the coordinate at which there occurs the temperature T_s defined by $(T_0/T_s)^5 = 3$. Then for $x < x_s$, $T \simeq T_0$ and Equation (45) becomes

$$\frac{dT}{dx} \simeq - \sqrt{\frac{2}{3}} \left(\frac{eE}{k} \right) \left(\frac{T_0 - T}{T_0} \right)^{1/2}, \quad x \leq x_s \quad (47)$$

An integration then gives

$$\frac{T}{T_0} \simeq 1 - \frac{1}{6} \left(\frac{eEx}{kT_0} \right)^2, \quad x \leq x_s \quad (48)$$

for the profile starting at $x = 0$, $T = T_0$. For $T = T_s$ Equation (48) gives

$$\frac{eEx_s}{kT_0} \simeq \sqrt{6 \left(1 - \frac{T_s}{T_0} \right)} = 1.09 \quad (49)$$

For $x > x_s$, the unity term in the bracket of Equation (45) may be neglected. Then

$$\frac{dT}{dx} \simeq - \sqrt{\frac{2}{15}} \left(\frac{eE}{k} \right) \left(\frac{T_0}{T} \right)^{5/2}, \quad x > x_s \quad (50)$$

The solution to this equation matching Equation (48) at $x = x_s$ is

$$- \int_{T_s}^T \left(\frac{T}{T_0} \right)^{5/2} dT = \sqrt{\frac{2}{15}} \frac{eE(x-x_s)}{k}$$

which gives

$$\left(\frac{T_s}{T_o}\right)^{7/2} - \left(\frac{T}{T_o}\right)^{7/2} = \sqrt{\frac{49}{30}} \frac{eE(x-x_s)}{kT_o} \quad (51)$$

The requirement that this curve passes through (x_w, T_w) gives for $(T_s/T_w)^{7/2} \gg 1$

$$\frac{eE(x_w - x_s)}{kT_o} \approx \sqrt{\frac{30}{49}} \left(\frac{1}{3}\right)^{7/10} = 0.36 \quad (52)$$

Combination of Equations (49) and (52) gives for the relation between electric field, channel size, and central arc temperature

$$\frac{eEt}{2kT_o} \approx 1.45 \quad (53)$$

The power delivered to unit area of the wall again may be estimated as the sum of the powers dissipated in the channel for $0 < x < x_s$ and $x_s < x < x_w$. The first integral is, from Equations (15), (42) and (47),

$$\begin{aligned} \frac{-\sigma_o E^2}{\frac{eE}{k} \sqrt{\frac{2}{3}}} \int_{T_o}^{T_s} \left(\frac{T}{T_o}\right)^{3/2} \left(\frac{T_o - T}{T_o}\right)^{-1/2} dT &\approx \frac{\sigma_o E^2}{\frac{eE}{kT_o} \sqrt{\frac{2}{3}}} \int_0 \left(1 - \frac{T_s}{T_o}\right)^{1 - \frac{3}{2} y} \frac{1 - \frac{3}{2} y}{y^{1/2}} dy \\ &\approx 0.98 \left(\frac{kT_o}{eE}\right) \sigma_o E^2 \end{aligned}$$

since $(T/T_o) \approx 1$ in this range. The second integral is, from Equations (15), (42) and (50),

$$\frac{-\sigma_o E^2}{\frac{eE}{k} \sqrt{\frac{2}{15}}} \int_{T_s}^{T_w} \left(\frac{T}{T_o}\right)^{3/2} \left(\frac{T}{T_o}\right)^{5/2} dT = \sqrt{\frac{3}{10}} \left(\frac{kT_o}{eE}\right) \sigma_o E^2 \left[\left(\frac{T_s}{T_o}\right)^5 - \left(\frac{T_w}{T_o}\right)^5 \right]$$

$$\approx .18 \left(\frac{kT_o}{eE}\right) \sigma_o E^2$$

for $(T_s/T_w)^5 \gg 1$. Then the power density at the wall is approximately

$$P_w \approx 1.16 \left(\frac{kT_o}{eE}\right) \sigma_o E^2 \quad (54)$$

or, in view of Equation (53)

$$P_w \approx 0.80 \sigma_o E^2 x_w \quad (55)$$

Thus the average current density in the channel is about 80 percent of its maximum value for this mode. This discharge also is quite uniform and exhibits positive incremental resistance. The conductance varies as

$$G \sim \sigma_o \sim T_o^{3/2}$$

while Equation (54) and (53) give

$$P = \frac{P_w}{x_w} \sim G E^2 \sim G T_o^2$$

when the geometry is fixed. Thus

$$\frac{d(\ln G)}{d(\ln P)} = \frac{3}{7}$$

and the incremental resistance is rather strongly positive.

RADIATION-COOLED DISCHARGE (Mode 6)

When radiation is the main energy loss mechanism, the discharge temperature, particle densities, and current density tend to be uniform throughout the discharge, and the discharge equations take the simple form

$$J = \sigma_o E \quad (56)$$

and

$$E \cdot J = \frac{2\epsilon_r}{t} s T_o^4 \quad (57)$$

Here ϵ_r is the emissivity of the discharge, s the Stefan-Boltzmann constant (5.67×10^{-8} watts/m²-°K⁴) and the remaining symbols have the usual meanings. Substitution of Equation (56) in Equation (57) gives

$$E = \left[\frac{2\epsilon_r}{\sigma_o t} s T_o^4 \right]^{1/2} \quad (58)$$

Thus if $\sigma_o(p, T_o)$ and $\epsilon_r(p, T_o, t)$ are known, Equation (58) can be used to calculate the electric field E for any temperature T and pressure p , and Equation (56) then can be used to calculate the corresponding current density J . Determination of the conductivity is a straightforward process involving calculation of electron densities from the Saha equation, the use of these densities in Equation (2) to calculate resistivities associated with electron-atom interactions, and the use of Spitzer's analysis to calculate resistivities caused by electron-ion interactions. Determination of the emissivity is a more complex problem, and because of this complexity much of the simplicity of the preceding development is only apparent.

Radiation from the discharge comes as atomic line radiation, molecular band radiation, and electronic continua. The electronic continua may come from free electrons recombining into discrete states (free-bound transitions) or from free electrons interacting with electromagnetic fields (free-free transitions). For the metal vapor discharges of principal interest here, molecular band radiation and recombination continua should be minor factors, and the principal sources should be atomic line radiation (dominant at low current densities) and the free-free electron continuum (dominant at high current densities).

The free-free continuum radiation can be estimated by calculating the energy absorbed by the free electrons in equilibrium with the thermal radiation field, and then equating the powers absorbed and radiated. The motion of a single electron driven by an electric field \underline{E} and undergoing momentum transfer collisions with an average frequency ν is described by the momentum balance

$$m \frac{dv}{dt} + \nu m \underline{v} = -e \underline{E} \quad (59)$$

The component of the velocity that is correlated with the \underline{E} field is then

$$\underline{v}(t) = -\frac{e}{m} \int_0^{\infty} \epsilon^{-\nu\tau} \underline{E}(t-\tau) d\tau \quad (60)$$

and the average rate at which the electron gains energy from the field is

$$-e \langle \underline{v}(t) \cdot \underline{E}(t) \rangle = \frac{e^2}{m} \int_0^{\infty} \epsilon^{-\nu\tau} \langle \underline{E}(t) \cdot \underline{E}(t-\tau) \rangle d\tau \quad (61)$$

For a single sinusoidal field component

$$\underline{E} = \underline{E}_{\max} \cos \omega t$$

the average in the integral on the right of Equation (61) is

$$\langle \underline{E}(t) \cdot \underline{E}(t-\tau) \rangle = \frac{E_{\max}^2}{2} \cos \omega\tau$$

and the average power absorbed from the field by the electron (and dissipated in collisions) is

$$-e \langle \underline{v}(t) \cdot \underline{E}(t) \rangle = \frac{e^2}{m} \frac{\nu}{\nu^2 + \omega^2} \frac{E_{\max}^2}{2} \quad (62)$$

Then the absorption length L for incoherent absorption of frequency ω by a plasma containing electron density n_e is

$$\begin{aligned} L &\equiv \frac{\Delta}{\text{incident power per unit area}} \\ &= \frac{\text{power absorption per unit volume}}{\text{incident power per unit area}} \\ &= \frac{\epsilon_0 \frac{E_{\max}^2}{2} C}{\frac{n_e e^2}{m} \frac{\nu}{\nu^2 + \omega^2} \frac{E_{\max}^2}{2}} \end{aligned} \quad (63)$$

$$L = \frac{C(\nu^2 + \omega_p^2)}{\nu \omega_p^2}$$

where ω_p is the usual electron plasma frequency

$$\omega_p = (n_e e^2 / m \epsilon_0)^{1/2}$$

The significance of the absorption length is that a beam of frequency ω incident on the plasma decreases in power with penetration x into the plasma as $\exp - (x/L)$.

If the plasma is in thermal equilibrium with an enclosure at temperature T , it is subjected to isotropic thermal radiation having the Planck spectrum

$$\frac{\hbar \omega^3}{4\pi^2 C^2 (\epsilon (\hbar \omega / kT) - 1)} \quad \begin{array}{l} \text{power per unit area} \\ \text{per unit frequency} \end{array}$$

Then if the plasma is in the form of a slab of thickness t , so that the average path length through the plasma is $2t$ for isotropic radiation, the total power absorbed by the plasma from the radiation is

$$\int_0^{\infty} \frac{\hbar \omega^3}{4\pi^2 C^2 (\epsilon (\hbar \omega / kT) - 1)} \left[1 - \epsilon^{-\left(\frac{2\nu \omega_p^2 t}{C(\nu^2 + \omega^2)} \right)} \right] d\omega$$

In thermal equilibrium the plasma must radiate an equal amount of power: Since the radiation per unit area also can be expressed as $\epsilon_r sT^4$, the plasma emissivity ϵ_r must be

$$\epsilon_r = \frac{1}{sT^4} \int_0^{\infty} \frac{\hbar \omega^3 \left[1 - \epsilon^{-\left(\frac{2\nu \omega_p^2 t}{C(\nu^2 + \omega^2)} \right)} \right]}{4\pi^2 C^2 (\epsilon (\hbar \omega / kT) - 1)} d\omega \quad (64)$$

This integral cannot be evaluated exactly in closed form and must be calculated numerically or, as done here, approximated by a simpler expression.

The approximation used here in evaluating the plasma emissivity can be motivated by noting that the spectral emissivity

$$\left[1 - \epsilon - \frac{2\nu \omega_p^2 t}{C(\nu^2 + \omega^2)} \right]$$

is highest at low frequencies and approaches zero as $\omega \rightarrow \infty$. The dividing line between "low" and "high" frequencies occurs where the argument of the exponential has unit magnitude,

$$1 = \frac{2\nu \omega_p^2 t}{C(\omega^2 + \nu^2)}$$

$$\omega^2 = \frac{2\nu \omega_p^2 t}{C} \left[1 - \frac{\nu C}{2\omega_p^2 t} \right]$$

$$\omega^2 = \frac{2\nu \omega_p^2 t}{C} \left[1 - \frac{\epsilon_o C}{2\sigma t} \right]$$

Above this critical frequency the spectral emissivity goes rapidly to zero; at lower frequencies it approaches

$$\left[1 - \epsilon - \frac{2\sigma t}{\epsilon_o C} \right]$$

which is close to unity for the range of conditions where electron radiation is significant, $\sigma > 100$ mho/m and $t > 10^{-5}$ m. Thus the spectral emissivity can be approximated by a function that is unity for

$$\omega < \left[\frac{2\nu \omega_p^2 t}{C} \left(1 - \frac{\epsilon_o C}{2\sigma t} \right) \right]^{1/2} \approx \left(\frac{2\nu \omega_p^2 t}{C} \right)^{1/2}$$

and zero otherwise. The total emissivity (for the free-free electron continuum) given by Equation (64) then is approximately

$$\epsilon_r \approx \frac{1}{sT^4} \int_0^{\sqrt{\frac{2\nu\omega_p^2 t}{C}}} \frac{\hbar\omega^3 d\omega}{4\pi^2 C^2 (\epsilon^{\hbar\omega/kT} - 1)} \quad (65)$$

Equation (65) can be expressed in terms of an integral over wavelength λ giving

$$1 - \epsilon_r \approx \frac{1}{sT^4} \int_0^{2\pi C \sqrt{\frac{C}{2\nu\omega_p^2 t}}} \frac{2\pi hC^2}{\lambda^5} \left[\epsilon^{\hbar C/\lambda kT} - 1 \right]^{-1} d\lambda \quad (66)$$

This formulation has the advantage that the right side of Equation (66) is a tabulated function.⁴

Equation (66) should give a good approximation to the emissivity of the discharge when the fractional ionization is large and most of the radiation comes from thermal electrons. At low fractional ionization it gives too low values because most of the emission is atomic line radiation. To account roughly for this atomic radiation, while avoiding the complexities of calculating radiation associated with particular atomic structures, a lower limit is put here at the ratio (ϵ_r/t) used in Equations (57) and (58). For present purposes the emissivity calculated from Equation (66) is used if that value satisfies $(\epsilon_r/t) \geq 200 \text{ m}^{-1}$. When the value calculated from Equation (66) falls below this limit, that calculation is ignored, and a value $(\epsilon_r/t) = 200 \text{ m}^{-1}$ is used in Equations (57) and (58). This is a very crude approximation, but a useful one in an initial study of the conditions under which the various dissipation mechanisms are important. The value $(\epsilon_r/t) = 200 \text{ m}^{-1}$ corresponds to a value $(\epsilon_r/d) = 100 \text{ m}^{-1}$ for cylindrical discharges and is based on the observation that metal vapor lamp discharges of a few atmospheres pressure and a centimeter diameter, where atomic radiation is a dominant factor, are approaching opacity.

The incremental resistances of radiation cooled discharges may be either positive or negative. At the lower current densities, the electrical conductivity varies with temperature more rapidly than the radiated power and the discharge exhibits negative incremental resistance. At high current densities where a high fraction of the metal vapor is ionized the converse is true.

CALCULATION OF VOLT-AMPERE CHARACTERISTICS

Figures 34 and 35 show volt-ampere plots for discharges in 0.002- and 0.020-inch wide channels in mercury vapor at one atmosphere pressure.* Each of the numbered curves in these figures was calculated assuming that the corresponding mode of discharge operation dominated. Table V identifies the modes (whose numbering corresponds to the preceding section numbers) and summarizes the calculations for each mode. In addition to these calculations, which have been specified in detail in the preceding sections, it is necessary to calculate electron density and electrical conductivity for various temperatures and pressures as outlined in a subsequent section.

From Figures 34 and 35 it appears that all the processes discussed contribute significantly to discharge behavior within the range of channel widths covered and that modes 2, 3, 5, and 6 all are dominant under some conditions within the range. Dominance here is indicated by the largest voltage gradient (and thus the strongest energy loss mechanism) for a given average current density. Only qualitative conclusions should be drawn from these figures, however, because the central discharge temperature varies as a function of current density differently along the different mode curves. In addition the temperature and current density profiles differ among the various modes at a given average current density. Thus, in particular, it is not possible to get a total discharge voltage gradient for a fixed current simply by adding the voltage gradients for the five modes at that current.

Inspection of Table V shows that modes 3, 4, 5, and 6 are similar in providing fairly uniform temperature and current density distributions within the discharge. The ratio of peak current density to average current density ranges from 1.0 to 1.6 for these four modes. For these modes it appears reasonable to assume that the modes can coexist without much interaction and that the total power loss at a fixed central temperature is the sum of the individual mode losses at that temperature. (Of course, modes 3 and 5 do not exist together, since these are just two asymptotic approximations to discharges in which a single energy dissipation mechanism dominates, that of electronic thermal conduction.) On the other hand, mode 2 is a heavily

*See footnote on page 94

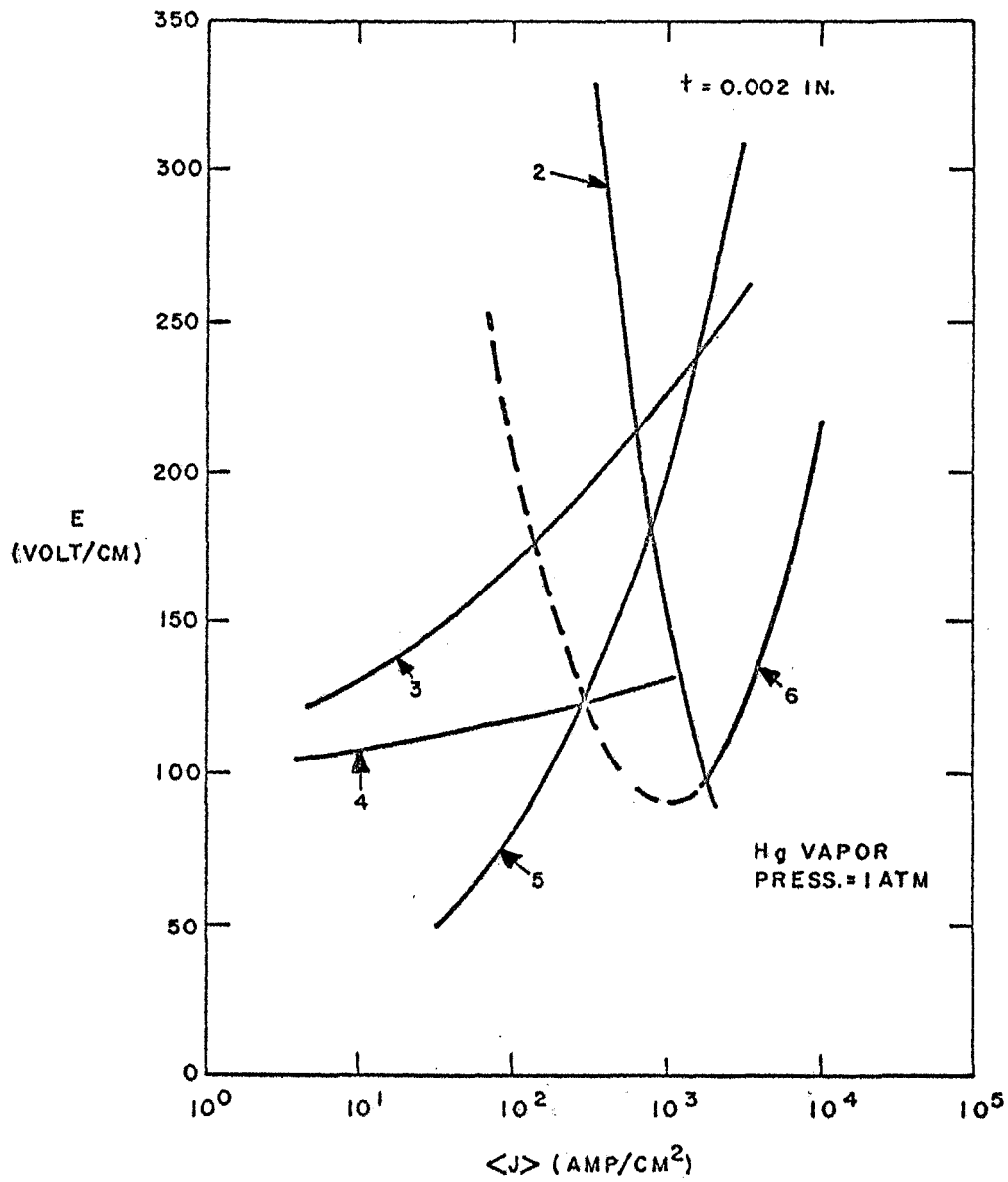


Figure 34 - Voltage-Current Characteristics for the Five Modes in an Atmospheric-Pressure Mercury Vapor Discharge 0.002-Inch Thick

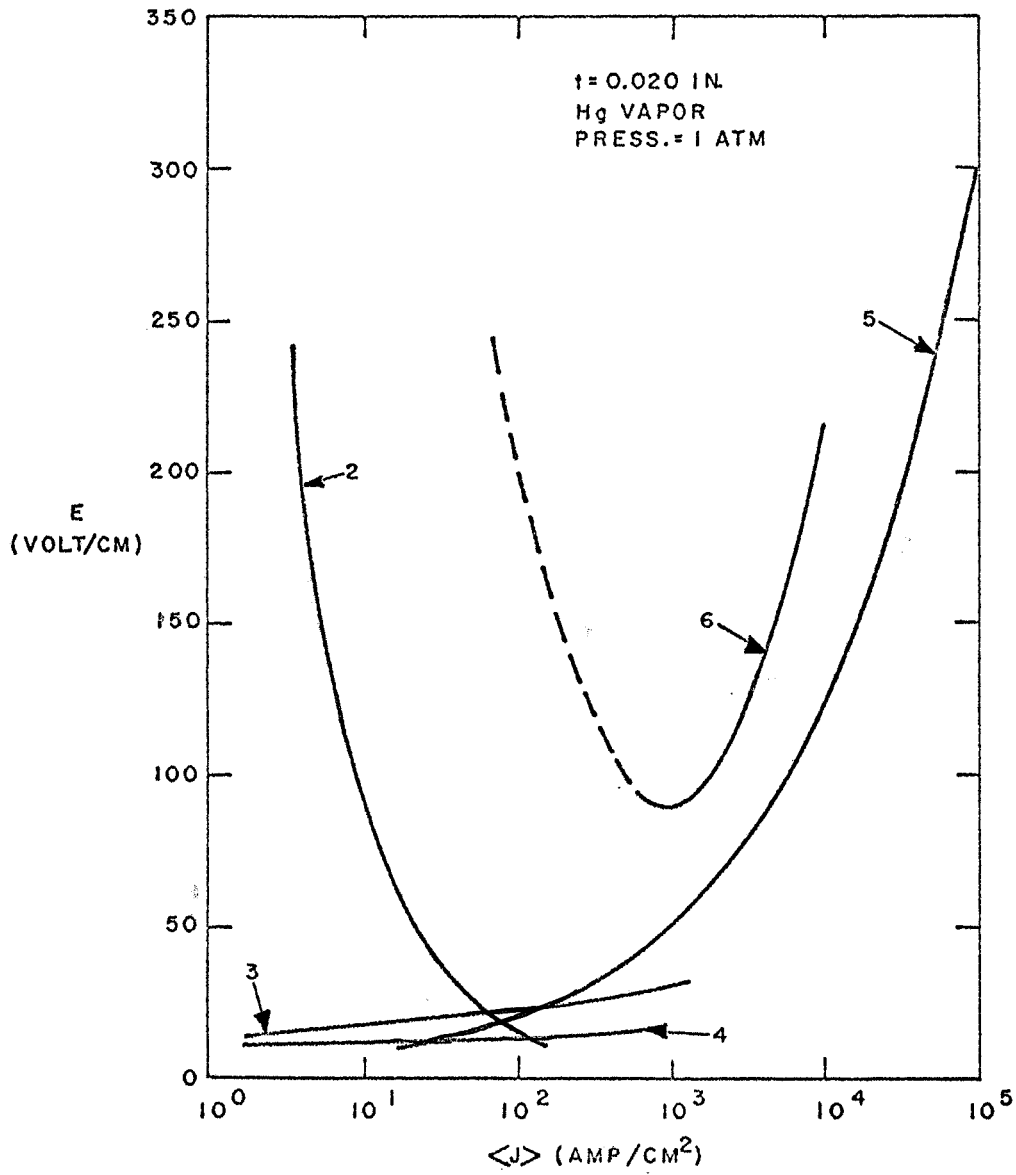


Figure 35 - Voltage-Current Characteristics for the Five Modes
 in an Atmospheric-Pressure Mercury Vapor Discharge
 0.020-Inch Thick

Table V - Summary of Calculations for Individual Modes

MODE	THERMAL TRANSPORT BY	FRACTIONAL IONIZATION	E vs. (p, T ₀)	$[\langle J \rangle / \sigma_0 E]$	REMARKS
2	Atomic Conduction	Slight	Eq. (14)	$\frac{3(kT_0/eU)}{1 - (T_w/T_0)^{3/2}}$	Calculations for T _w = 0 A _{aa} = 30 Å ² for H _g
3	Electronic Conduction	Slight	Eq. (30)	0.63	$\mu_{ea} = 4 \times 10^{23}$ (m-volt-sec) ⁻¹ for H _g
4	Ion Diffusion	Slight	Eq. (39)	2/π	$\mu_{ia} = 1.3 \times 10^{21}$ (m-volt-sec) ⁻¹ for H _g
5	Electronic Conduction	High	Eq. (53)	0.80	---
6	Radiation	Any	Eq. (58)	1	Emissivity for calculations is the greater of: 1) the value from Eq. (66) or 2) the value given by (ε _r /t) = 200 m ⁻¹

contracted, nonuniform discharge in which the peak current density typically is 10 or more times the average. This mode is not likely to coexist with the others without great distortion; either it or they will dominate.

The preceding reasoning indicates that the problem of generating volt-ampere characteristics for practical discharges in which several dissipation mechanisms are active can be handled in two stages. First, the characteristic of the contracted discharge cooled by atomic thermal conduction mode 2 can be calculated as outlined in Table V. Next, the characteristic of the relatively uniform discharge cooled by electronic thermal conduction, ion diffusion, and radiation can be calculated. A plot of these two characteristics always shows that at low current the mode 2 discharge dissipates the larger power and requires the greater voltage gradient, while at high currents the uniform discharge dissipates the larger power. Since all the dissipation mechanisms actually are operating in every real discharge, and since the strongest dissipation mechanisms determine discharge behavior, the real discharge should approximate the mode 2 discharge at low currents and the uniform discharge at high currents. The transition from the contracted to the uniform discharge is assumed here to occur at conditions where the two volt-ampere characteristics cross.

A need remains for a procedure by which the calculations for modes 3, 4, 5, and 6, as outlined in Table V, can be combined to provide volt-ampere characteristics for the uniform discharge. At any given central temperature T_0 and total pressure p , the average electrical conductivity of the uniform discharge is determined, and the power dissipated is proportional to E^2 . Thus if the uniform discharge is to dissipate, at fixed T_0 and p , the sum of the powers dissipated by mode 6, mode 4, and the more relevant of modes 3 and 5, the square of its voltage gradient must equal the sum of the squares of the individual mode voltage gradients at that temperature and pressure. The average current density of the uniform discharge then is approximately the product of the resulting voltage gradient E and the known conductivity σ_0 .

The curves of Figure 36 were constructed according to the preceding prescription. The central discharge temperatures vary along each curve from about 0.4 eV on the left to about 1.0 eV on the right. In the upper left corner the results are dominated by mode 2, in the upper right by mode 5, in the lower right by mode 6, and in the lower left by combinations of modes 3 and 6. The minimum voltage gradients obtained vary slowly with thickness at the larger discharge thicknesses where radiative dissipation predominates, and more rapidly at the smaller thicknesses where conductive dissipation predominates, approaching a dependence like $E_{\min} t = (\text{constant})$. The

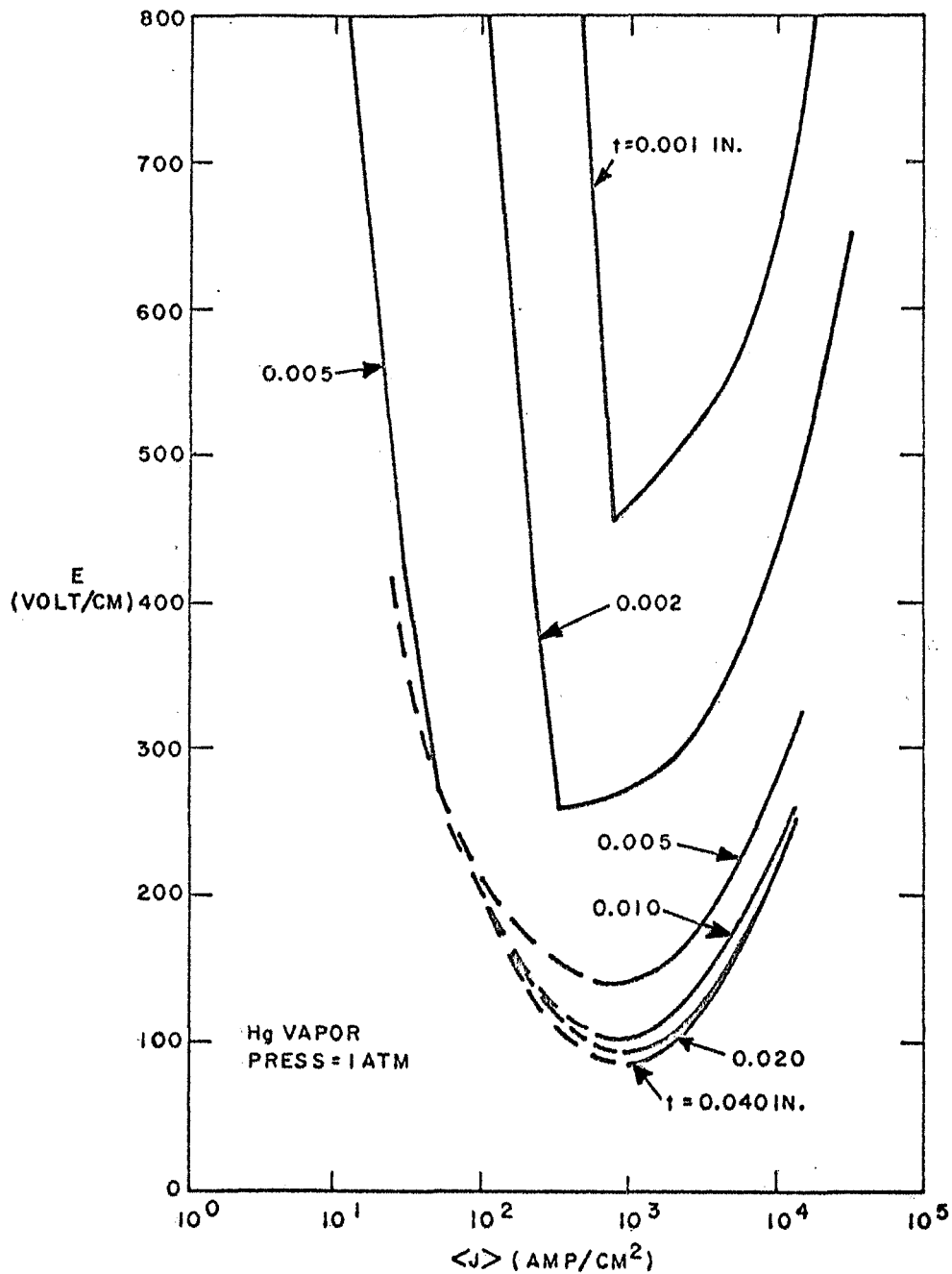


Figure 36 - Combined Voltage-Current Characteristics for Atmospheric Pressure Mercury Vapor Discharge of Several Thicknesses

voltage minima occur near an average current density of 1000 amp/cm² over the range of discharge thicknesses studied. This relative constancy of average current density at voltage minimum may be a fortuitous result valid only for mercury vapor.

Portions of the curves in Figures 34, 35, and 36 are drawn with a dashed line to indicate regions where the present calculations indicate that atomic line radiation provides the dominant power loss. Because of the crudeness of the approximation used in calculating the loss due to line radiation, these portions of the curves should be regarded as tentative approximations. With additional work it should be possible to do much better; the present approximation is sufficient, however, to outline the regions where line radiation may be an important loss process.

In comparing these calculations with experimental data it may be convenient to use experimental results for cylindrical discharges. When this is done, cylinders and slabs of the same surface-to-volume ratio should be compared in the regions where radiative effects dominate, and cylinders and slabs having the same "diffusion length" should be compared in regions where conductive losses dominate. For the same surface-to-volume ratio of a cylinder of diameter d and a slab of thickness t

$$d = 2t$$

Equality of diffusion lengths requires that

$$d = \frac{(2)(2.4)}{\pi} t \simeq 1.5 t$$

Thus these slab calculations may be compared with results for cylindrical discharges of diameters 1.5 to 2 times the slab thicknesses.

CONCLUSIONS

The calculations performed here show that several dissipation mechanisms - atomic thermal conduction, electronic thermal conduction, ionic diffusion, and radiation, have significant effects on high pressure mercury vapor arcs, at thicknesses up to one millimeter, operated near the voltage minima of the volt-ampere characteristics.* Similar effects are expected in other metal vapors. Of these dissipation mechanisms, all but ionic diffusion become the dominant loss mechanism for some conditions within the ranges studied.

* See footnote on page 94

The computational procedure developed here provides a reasonable, but as yet untested, way of combining the relatively elementary calculations for volt-ampere-temperature characteristics of discharges in which one loss mechanism dominates to provide approximate characteristics for real discharges in which several loss processes are present simultaneously.

The results obtained point out the need for a better treatment of atomic line radiation than is given here, particularly for the calculation of the minimum electric fields that will support mercury vapor discharges in channels of thicknesses exceeding 0.002 inch.

Few experimental results are available at present to check these calculations and no detailed comparisons have been performed yet. A cursory inspection of some experimental data for mercury vapor arcs in channels of 0.020- to 0.040-inch thicknesses driven by low impedance sources providing electric fields of 100 to 200 v/cm indicates that the calculated curves give good agreement with experiment in this radiation-dominated region.

CALCULATION OF ELECTRON DENSITIES AND ELECTRICAL CONDUCTIVITIES

The calculations outlined in the preceding sections require evaluation of the electron densities and electrical conductivities at the center of the discharge for given pressure and central temperature. The electron density is obtained by simultaneous solution of the equation for electrical neutrality,

$$n_e = n_i$$

the ideal gas law,

$$p = (n_{ao} + n_{eo} + n_{io}) kT_o$$

and the thermal equilibrium condition or Saha equation

$$\frac{n_{eo} n_{io}}{n_{ao}} = \left(\frac{g_e g_i}{g_a} \right) \left(\frac{2\pi mkT_o}{h^2} \right)^{3/2} \exp \left(- \frac{eU}{kT_o} \right)$$

Here g_e , g_i and g_a are the degeneracy factors for the electron, ion, and atom, respectively equal to 2, 2, and 1 for mercury. These expressions are adequate for temperatures below the level (somewhat greater than 1 eV for mercury) where multiple ionization becomes a significant factor.

Once the electron and neutral densities are known the resistivity due to electron-atom interactions can be calculated from

$$\frac{1}{\sigma_{ea}} = \frac{1}{n_e e \mu_{ea}}$$

The mobility μ_{ea} for electrons in mercury vapor used in these calculations is given by

$$\mu_{ea} n_a = 4 \times 10^{23} \text{ (m-volt-sec)}^{-1} \text{ for mercury}$$

The electron ion component of resistivity is calculated conveniently from results obtained by Spitzer and colleagues which yield

$$\frac{1}{\sigma_{ei}} = 65.3 \frac{\ln \Lambda}{T^{3/2}} \text{ (ohm-meter)}$$

when the ions carry a single electronic charge. Here T is in $^{\circ}\text{K}$. The parameter $\ln \Lambda$ is a slowly varying function of temperature and electron density that is approximately 6 for the conditions of interest here. The calculations done here use

$$\frac{1}{\sigma_{ei}} = \frac{400}{T^{3/2}} \text{ (ohm-meter)}$$

The net conductivity σ can be estimated from

$$\frac{1}{\sigma} \simeq \frac{1}{\sigma_{ea}} + \frac{1}{\sigma_{ei}}$$

*NOTE: Since the preceding work was completed an error has been discovered in the numerical calculations for Mode 6, the discharge cooled by free-free electron radiation. The effect of the error is to exaggerate greatly the power dissipated in this mode. The curves for Mode 6 in Figures 34 and 35 suffer from this error and should be ignored, as should the curves in Figure 36 for thicknesses exceeding 0.010 inches.

When the numerical error is eliminated the conclusion results

that free-free electron radiation is not a significant power dissipation process for any conditions of interest to the operation of self-healing fuses. The power dissipation mechanisms governing arc operation at large thicknesses and high current densities are not yet understood in quantitative terms.

Appendix B

SURFACE EFFECTS OF HIGH-ENERGY PULSES

This appendix contains a derivation for the surface temperature rise of a surface as a result of applying a rectangular shaped heat-energy pulse to the surface. In the interest of simplicity, certain assumptions will be made. In general, the following derivation stems from two basic facts:

(a) A temperature gradient is established in accordance with the applied energy density.

(b) The amount of material heated and the average temperature rise of that material must be consistent with the energy that is absorbed by the material.

It is assumed that:

1. The power dissipation at the surface during the energy pulse period is constant. While a plot of energy versus time for typical CSCL operation is actually not a rectangle, the rectangle may be defined as one having a width equal to the duration time of the energy pulse and a height such that the area represents the energy given up during the pulse.

2. The gradient established at the heated surface extends inward to the point where it intersects the X axis (line AC) in Figure 37. The actual case is a gradient that decreases as penetration is increased (curve AD). (It is believed that the error caused by the above assumption is small since area ABC is about 80 percent of the area ABD.) In the derivation, the area of the triangle ABC will represent the energy absorbed by the surface. The area under the actual gradient, then, cannot exceed the triangular area. The area under the triangle is more nearly equal to the area under a curved gradient, when the curved gradient is adjusted downward some 10 percent as in the case of EF. (From the above, the calculated surface temperature rise will be higher than the actual rise, and, if desired, this 10-percent correction can be made.)

3. The heat flow is linear for a single event. Because the penetration is so small in the transient case, compared to the cross-section of the heat front, the material being heated may be considered as a solid having a cross-section equal to the area of the impinging heat front and a depth equal to the depth of penetration.

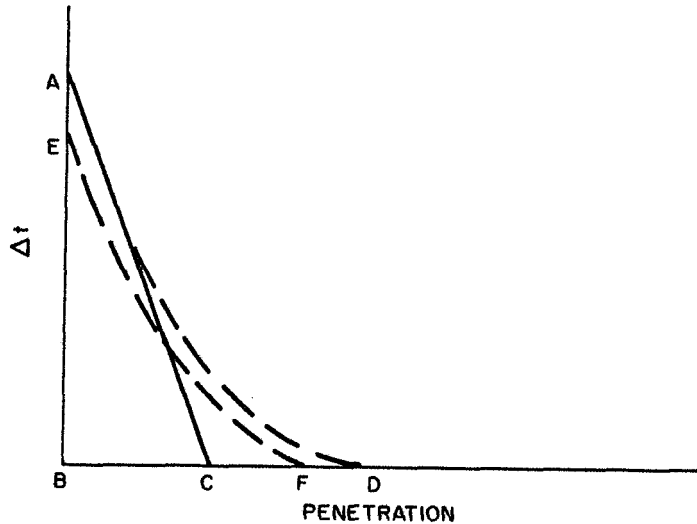


Figure 37 - Generalized Temperature Profiles
for Heated Surfaces

4. The physical constants of the material being evaluated in temperature remain constant. While this is not completely true, the constants may be chosen so as not to overstate the temperature rise.

The notations used are as follows:

ΔT = temperature rise, $^{\circ}\text{K}$ at anode surface

(avg. ΔT) = average ΔT of the anode material affected
by heat front = $Hp/2$

The general energy relationship becomes:

$$q = C_s DV (\text{avg } \Delta T) = C_s a D p \left(\frac{Hp}{2}\right) \quad (67)$$

using $\Delta T = Hp$ (68)

and $H = \frac{q}{Kat}$ (69)

Solving Equation (67) for p:

$$p = \frac{2q}{C_s a D \left(\frac{q}{Kat}\right) p} = \frac{2Kt}{p C_s D}$$

or $p^2 = \frac{2Kt}{C_s D}$ and $p = \sqrt{\frac{2Kt}{C_s D}}$ (70)

Then: $\Delta T = Hp = \frac{q p}{Kat} = \frac{q \sqrt{\frac{2Kt}{C_s D}}}{Kat}$

$$= \frac{q \sqrt{2}}{a \sqrt{Kt C_s D}} = \frac{\sqrt{2t P_w}}{a \sqrt{K C_s D}} \quad (71)$$

Thus, the surface temperature rise resulting from a pulse of energy for a given current limiter bore geometry would be a function of $(K C_s D)^{-1/2}$ for the bore material and refractory metals have approximately a 2-to-1 advantage in this factor. The bore erosion experienced will be a function of surface temperature and the refractoriness of the bore material.

Appendix C

CURRENT LIMITERS DRIVEN BY CONSTANT CURRENTS

This appendix presents a derivation of expressions relating channel geometry and current to current limiter firing time for the case where the "fault" current is constant, as depicted in Figure 17.

If the channel is assumed to be a uniform cylinder, and thermal conduction is neglected, the heating is determined by the energy balance:

$$C_s \frac{dT}{dt} = Ri^2 \quad (72)$$

The solution to this equation giving $T = T_c$ at $t = 0$, when i remains constant and R varies linearly with temperature T such that:

$$R = R_c [1 + \alpha (T - T_c)] \quad (73)$$

is

$$T - T_c = \frac{1}{\alpha} \left[\exp \left(\frac{\alpha T_c i^3}{3C_s} \right) - 1 \right] \quad (74)$$

or

$$R_c i^2 t = \frac{\ln [1 + \alpha (T - T_c)] C_s}{\alpha} \quad (75)$$

When the Dulong-Petit value (3k per atom) is used to estimate specific heat we obtain:

$$C_s = \frac{3N_o k D a \ell}{M} \quad (76)$$

We may substitute for cold resistance R_c the expression:

$$R_c = \rho_c \frac{\ell}{a} \quad (77)$$

Substituting equations (76) and (77) in equation (75), we obtain:

$$i^2 t = \frac{3N_o kD}{M\rho_c} \frac{\ln[1 + \alpha (T - T_c)]}{\alpha} a^2 \quad (78)$$

Since $\alpha (T - T_c)$ is small, this may be written

$$i^2 t \cong \frac{3N_o kD (T - T_c)}{M\rho_c} a^2 \quad (79)$$

The firing of the limiter presumably occurs at the time when T equals the boiling point of the mercury at its filling pressure.

Except for minor changes that occur when the fill pressure is varied, the quantity ($i^2 t$) at firing for a cylindrical column driven by constant current is (a^2) times a constant determined by the fill metal. For mercury and loading pressure of a few atmospheres, we obtain:

$$i^2 t \cong 5 \times 10^6 a^2 (\text{amp})^2 - \text{sec} \quad (80)$$

where area is expressed in cm^2 . Note that the firing time is very sensitive to current and the cross-section, and varies about as the 4th power of the diameter for cylindrical channels.

This relationship is plotted for 0.015-inch and 0.020-inch diameter cylinders of mercury in Figure 38. The actual performance of 0.020 inch and 0.023 inch fuses is also plotted here.

It should be noted that the constant current case plotted in Figure 38 is also valid for RMS current. For sinusoidal alternating current of at least 1/2 cycle duration, an RMS value of $1/\sqrt{2} I_{\text{max}}$ would apply. For severe fault currents, where circuit inductance limits current to an essentially linear function of time [$i \approx (V/L)t$], an RMS value of $1/\sqrt{3} I_{\text{max}}$ would apply.

As would be expected, the actual performance begins to deviate from the theoretical line at about 4 milliseconds as the rate of thermal diffusion into the alumina begins to be appreciable. The curve will asymptotically approach some current level where steady-state heat flow from the channel

equals the energy dissipated in the channel, and this would become a current rating for the fuse, comparable to a conventional fuse current rating. This rating would be appreciably affected by the thermal impedance of the mechanical support structure of the fuse, of course, and such considerations would probably be a factor in the eventual application of the fuse.

Several test firings have been made at constant currents which cause the fuse to fire after 10 to 30 seconds. In summary, the data show that 0.015-inch diameter fuses open in 10 to 30 seconds at 20 amperes, while 0.020-inch fuses open at 27 amperes over the same interval. By using the wattage dissipated, the external fuse temperature, the boiling temperature of mercury (as the internal temperature), and the channel wall area, a good approximation of steady state thermal impedance of the bore of the alumina fuse can be calculated. This impedance is a useful parameter for designing devices of various sizes. Typical values of test data and calculated values leading to thermal impedance, expressed as a coefficient of film heat transfer, are shown in Table VI.

Later, more comprehensive data indicate that the most representative film coefficient (h) is 1.2 watts/cm²/°K and the film temperature drop (ΔT_f) is usually about 300°K for alumina, sapphire or sandwich devices. Thus rated fuse current (I) is related to channel wall area by $I^2 R = 360 a_w$ where a_w is the wall area in cm² and R is the cold resistance of the mercury in the channel in ohms.

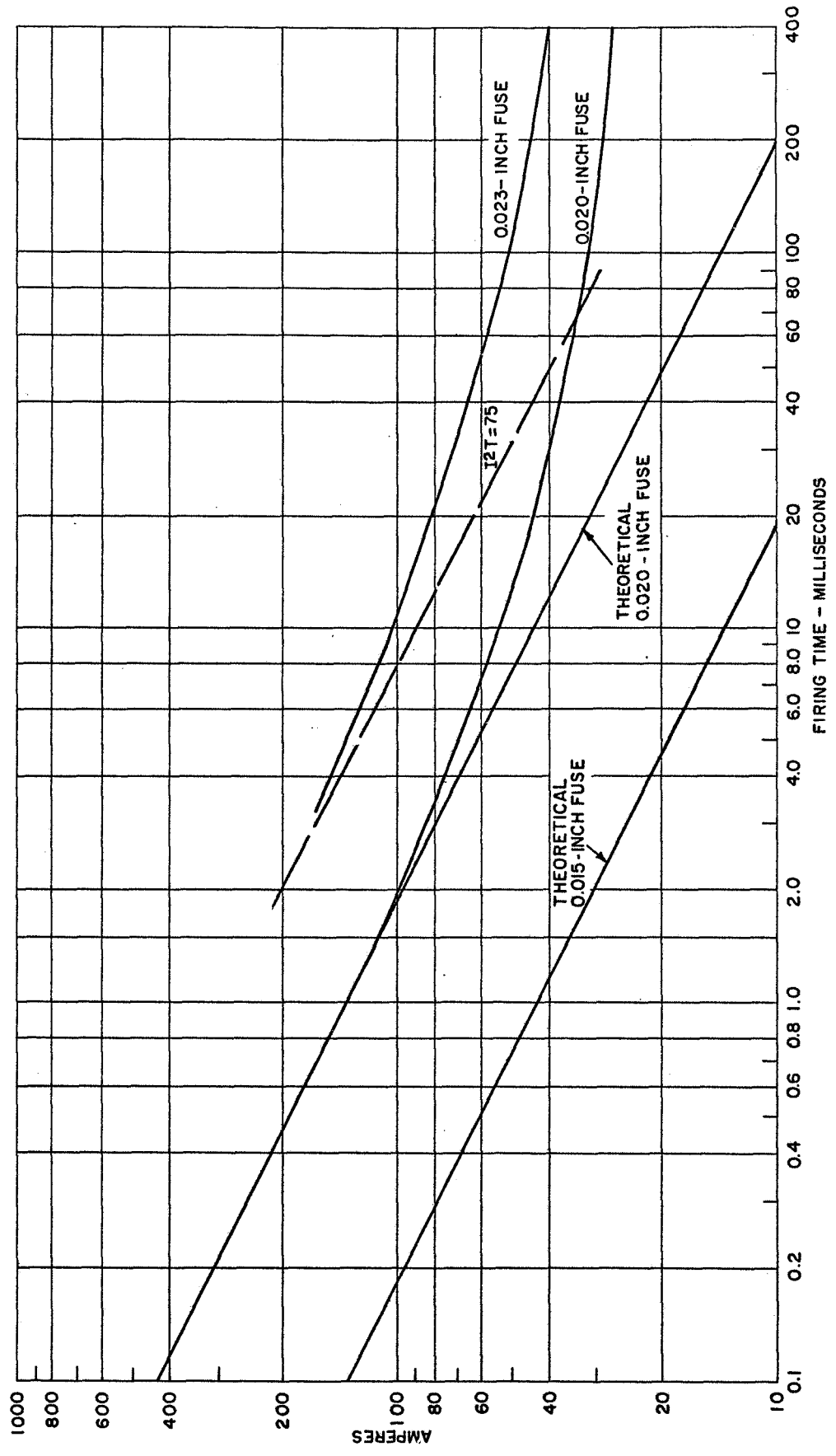


Figure 38 - Theoretical and Actual Firing Time at Constant Current

Table VI - Thermal Impedance of Alumina-Bore CSSL Devices

Capillary Dia. x Length (Inches)	External Temp. (°C)	Alumina Impedance "Z" (°C/Watt)	Heat in Capillary "W" (Watts)	Alumina $\Delta T_A = ZW$ (°C)	Mercury to Alumina ΔT_F (°C)	Capillary Wall Area "A" (Cm ²)	Film Coefficient "h" = $W / A \Delta T_F$ (Watts/Cm ² /°C)
.015 x .125	60	1.69	16	27	300	.038	1.40
.015 x .140	70	1.44	22	32	290	.043	1.76
.020 x .250	80	0.78	36	28	280	.101	1.30
.020 x .310	80	0.61	42	26	280	.126	1.19
.023 x .125	70	1.32	22	29	290	.056	1.36

Where: "Z" = thermal impedance from the capillary diameter (D1) to the outside diameter (D2) of the alumina (.250 inch).

$$Z = \frac{h_n (D2/D1)}{2\pi K L}$$

K = 0.83 Watt/Cm/°C for alumina

L = capillary length, Cm

$$\Delta T_F = 400^\circ\text{C} - (\text{External Temperature} + 40^\circ\text{C})$$

1. Average mercury temperature is assumed to be boiling minus 10°C or 400°C for these tests at 2 atmospheres pressure.
2. All other ΔT is estimated as 40°C based on ΔT_A .

Appendix D
GLOSSARY OF SYMBOLS

(MKS units are used except where specified otherwise)

Variables

A	collision cross section
a	surface or cross-sectional area
C	velocity of light
C_s	specific heat capacity of the liquid metal or solid
D	density of the liquid metal
d	diameter
E	electric field
e	electronic charge
G	conductance of unit arc length
g	statistical weight
H	temperature gradient in $^{\circ}\text{C}$
h	Planck constant (6.626×10^{-34} joule-sec)
\hbar	$h/2\pi$
I, i	current
J	current density
K	thermal conductivity
k	Boltzmann constant (1.38×10^{-23} joule/ $^{\circ}\text{K}$)
L	radiation absorption length
l	column length
M	molecular weight of the liquid metal
m	electron mass
N_o	Avogadro's number
n	particle density
P	power input per unit arc length
P_w	power to unit wall area
p	depth of penetration of heat front in centimeters
q	energy in watt-seconds
R	electrical resistance of the liquid metal column
R_c	"cold" resistance at $t = 0$
s	Stefan-Boltzmann constant (5.67×10^{-8} watt/ $\text{m}^2 - ^{\circ}\text{K}$)
T	absolute temperature
t	time
U	ionization potential
V	volume of material in cm^3

α	temperature coefficient of resistance
Γ	particle flux density
ϵ	neperian base
ϵ_r	emissivity
ϵ_o	vacuum permittivity
λ	wavelength
μ	mobility
ν	collision frequency
ρ_c	cold resistivity
σ	electrical conductivity
τ	time
ω	frequency
ω_p	electron plasma frequency

Subscripts

a	atom
c	cold state
e	electron
i	ion
max	maximum
min	minimum
o	discharge center
r	radiation
s	defined coordinate
w	wall
p	plasma

REFERENCES

1. For example Sears, F. W., Thermodynamics, the Kinetic Theory of Gases, and Statistical Mechanics, 2nd ed. Addison Wesley Publishing Co., Cambridge (1953) p. 267
2. Cobine, J. D., Gaseous Conductors, Dover Publications, Inc., New York (1958) Chapter 9
3. Spitzer, Lyman, Jr., Physics of Fully Ionized Gases, 2nd ed., Interscience Publishers, New York (1962) p. 139
4. Fulk, M. M., Reynolds, M. M., and Burley, R. M., "Radiometry", in American Institute of Physics Handbook, McGraw-Hill Book Co., New York (1957) pp. 6-65

CR-72868

FINAL REPORT DISTRIBUTION LIST

	<u>Copies</u>
NASA-Lewis Research Center 21000 Brookpark Road Cleveland, Ohio 44135	
Attn: C. C. Conger - MS 54-1	1
E. H. Davis - MS 54-5	1
R. E. Alexovich - MS 54-5	1
Dr. F. C. Schwarz - MS 77-2	6
Dr. I. T. Myers - MS 77-2	1
G. R. Sundberg - MS 77-2	15
H. A. Shumaker - MS 77-2	1
B. L. Sater - MS 77-2	1
Dr. S. C. Himmel - MS 77-1	1
C. C. Gettelman - MS 77-2	1
R. R. Miller - MS 3-3	1
Rockets & Vehicles Procurement Sec. - MS 500-313	1
C. S. Corcoran, Jr. - MS 500-202	1
P. E. Foster, Tech. Utilization Office - MS 3-19	1
Dorothy Morris, Librarian - MS 60-3	1
Alice Dill, Report Control Office - MS 5-5	1
 NASA-Marshall Space Flight Center Huntsville, Alabama 35812 Attn: Library	 1
 NASA-Langley Research Center Langley Station Hampton, Virginia 23365 Attn: Library	 1
 NASA-Ames Research Center Moffett Field, CA 94035 Attn: Library	 1
 NASA-Headquarters Washington, D. C. 20546 Attn: Library	 1

2

Copies

NASA Scientific & Technical Information Facility
P.O. Box 33
College Park, Maryland
Attn: NASA Representative

6

NASA-Goddard Space Flight Center
Greenbelt, Maryland 20771
Attn: Library

1

NASA-Manned Spacecraft Center
Houston, TX 77058
Attn: Library

1

Naval Research Laboratory
Washington, D.C. 20390
Attn: Librarian

1

Bureau of Naval Weapons
Department of the Navy
Washington, D.C. 20360
Attn: Librarian

1

Advanced Research Project Agency
The Pentagon
Washington, D.C. 20325
Attn: John Huth

1

Jet Propulsion Laboratory
4800 Oak Grove Drive
Pasadena, CA 91103
Attn: Librarian

1

Diamond Ordnance Fuze Laboratories
Connecticut Avenue & Van Ness Street, N.W.
Washington, D.C.
Attn: R. B. Goodrich (Branch 940)

1

U.S. Army Research & Development Laboratory
Energy Conversion Branch
Ft. Monmouth, N.J. 07703

1

Engineers Research & Development Laboratory Electrical Power Branch Ft. Belvoir, VA 22060	1
University City Science Institute Power Information Center - Rm. 2107 3401 Market Street Philadelphia, PA 19104	1
Naval Air Systems Command Department of the Navy Washington, D.C. 20360	1
Wright-Patterson Air Force Base Dayton, OH 45433 Attn: Aeropropulsion Laboratory Materials Laboratory	1 1
U. S. Atomic Energy Commission Germantown, MD 20767 Attn: Lt. Col. G. H. Anderson	1
U. S. Atomic Energy Commission Division of Space Nuclear Systems Washington, D. C. Attn: G. S. Leighton	1
Westinghouse Electric Corporation Aerospace Electrical Division Lima, OH 45800 Attn: Library	1
Lear-Siegler Incorporated Power Equipment Division P.O. Box 6719 Cleveland, OH 44101 Attn: C. Gebby	1
Aerospace Corporation P.O. Box 95085 Los Angeles, CA Attn: Library Tech. Documents Group	1

AiResearch Manufacturing Company Division of Garrett Corporation P.O. Box 5217 Phoenix, AZ 85010 Attn: Mrs. J. F. Mackenzie, Library	1
Battelle Memorial Institute 505 King Avenue Columbus, OH 43201 Attn: Library	1
TRW, Inc. 23555 Euclid Avenue Cleveland, OH Attn: Library	1
North American Rockwell Corporation 3370 East Anaheim Road Anaheim, CA 92803 Attn: Library	1
Ion Physics Corporation P.O. Box 98 Burlington, MA 01803 Attn: Technical Library	1
Northeastern University Boston, MA 02115 Attn: Dr. B. Rabinowici	2